DESIGN AND FABRICATION OF RESONANT NANOANTENNAS ON CHALCOGENIDE GLASSES FOR NONLINEAR PHOTONIC APPLICATIONS

A THESIS

SUBMITTED TO THE MATERIALS SCIENCE AND

NANOTECHNOLOGY PROGRAM

AND THE GRADUATE SCHOOL OF ENGINEERING AND SCIENCE

OF BILKENT UNIVERSITY

IN PARTIAL FULFILLMENT OF THE REQUIREMENTS

FOR THE DEGREE OF

MASTER OF SCIENCE

By

Hüseyin Duman

August, 2013

I certify that I have read this thesis and that in my opinion it is fully adequate, in scope and in quality, as a thesis for the degree of Master of Science.

Assoc. Prof. Dr. Mehmet Bayındır (Advisor)

I certify that I have read this thesis and that in my opinion it is fully adequate, in scope and in quality, as a thesis for the degree of Master of Science.

Assoc. Prof. Dr. Selçuk Aktürk

I certify that I have read this thesis and that in my opinion it is fully adequate, in scope and in quality, as a thesis for the degree of Master of Science.

Assist. Prof. Dr. Ali Kemal Okyay

Approved for the Graduate School of Engineering and Science:

Prof. Dr. Levent Onural
Director of the Graduate School

ABSTRACT

DESIGN AND FABRICATION OF RESONANT NANOANTENNAS ON CHALCOGENIDE GLASSES FOR NONLINEAR PHOTONIC APPLICATIONS

Hüseyin Duman
M.S. in Materials Science and Nanotechnology Program
Supervisor: Assoc. Prof. Dr. Mehmet Bayındır
August, 2013

Optical nanoantennas are the metallic nanostructures which confine electromagnetic waves into sub-wavelength volumes at resonant conditions. They are used for various applications including biological and chemical sensing, single molecule spectroscopy, manipulation and generation of light. Combining extremely large electromagnetic field enhancement in plasmonic resonant nanoantenna with high optical nonlinearity of chalcogenide glass leads to a low-threshold broadband light generation scheme in sub-wavelength chip-scale structures. New frequency generation with ultra-low pumping power in plasmonic nanostructures allows compact on-chip light sources which can find applications in single molecule spectroscopy, optical signal processing and broadband lasers. We propose plasmonic nanoantenna chalcogenide glass systems for initiating nonlinear phenomena at low threshold. Size and shape of antennas are optimized according to linear refractive index of substrate and surrounding media for this purpose by finite difference time domain (FDTD) simulations. Resonant behaviour of antennas at their near-field and nonlinear response of optically highly nonlinear chalcogenide glasses are investigated. On resonance, strong field accumulation at the interface of the gold stripe and highly nonlinear As_2Se_3 glass triggers a start of the spectral broadening of incident beam accompanied by third harmonic generation at an ultra-low threshold power level of 3 W/μm^2. Moreover, we fabricate the designed structures by electron beam lithography, wet chemical techniques and optimize each fabrication step of processes by several experiments. Fabrication steps are explained and SEM images of related steps are presented.

Keywords: Plasmonic resonant antenna, optical nonlinearity, supercontinuum generation, chalcogenide glasses, third harmonic generation.

ÖZET

DOĞRUSAL OLMAYAN FOTONİK UYGULAMALAR İÇİN KALKOJEN CAMLAR ÜZERİNDE REZONANT NANOANTEN TASARIMI VE ÜRETİMİ

Hüseyin Duman
Malzeme Bilimi ve Nanoteknoloji Programı, Yüksek Lisans
Tez Yöneticisi: Doç. Dr. Mehmet Bayındır
Ağustos, 2013

Optik nanoantenler rezonans durumlarında elektromanyetik dalgaları dalga boyundan daha küçük hacimlere yoğunlaştıran metal nanaparçacıklardır. Biyolojik ve kimyasal algılamar, tek molekül spektroskopisi, ışık üretimi ve yönlendirilmesi gibi uygulama alanları vardır. Plazmonik rezonant nanoantenlerin son derece iyi elektromanyetik alan yükseltgeme özelliği ile kalkojen camların yüksek optik doğrusal olmayan indisi bulunması özelliğini birleştirmek düşük eşik değerli geniş bantlı ışığın dalga boyunun altında çip ölçeğinde üretilmesine imkan tanıyor. Plazmonik nanoyapılarda düşük pompalama gücü ile yeni frekans üretilmesi kompakt ışık kaynakları üretilmesinin önünü açarak tek molekül spektrokopisi, optik sinyal işleme ve geniş bant lazerler gibi uygulama alanları bulabilir. Doğrusal olmayan optik fenomenlerin düşük eşik değerlerde başlatılması için nanoanten-kalkojen cam sistemleri önerdik. Bu amaçla "finite difference time domain" (FDTD) simülasyonları marifetiyle antenlerin boyut ve şekillerini alttaşın ve ortamın kırılma indisine göre optimize ettik. Antenlerin yakın çevresinde rezonans davranışları ve optik olarak yüksek nanlineeriteye sahip kalkojen camın doğrusal olmayan tepkisi incelendi. Rezonans durumda altın çubuk ve As_2Se_3 cam arasında oluşan güçlü alan birikimi 3 W/μm^2 gibi düşük eşik değerinde üçüncü harmonik oluşumunun eşlik ettiği, gelen ışık etrafında tayfsal genişlemenin başlangıcını tetikliyor. Bununla birlikte, tasarlanan yapıları elektron ışın litografisi ve kimyasal yöntemler kullanarak ürettik. Ayrıca, her üretim basamağını bir dizi deney sonucunda optimize ettik. Üretim basamakları ilgili SEM görüntüleri verilerek açıklandı.

Anahtar sözcükler: Plazmonik rezonant antenler, doğrusal olmayan optik, süper süreklilik oluşumu, kalkojen camlar, üçüncü harmonik oluşumu.

Acknowledgement

Firstly, I would like to thank my supervisor Assoc. Prof. Mehmet Bayındır for his invaluable guidance, support and encouragement. I would also like to thank Prof. Salim Çıracı and Assoc. Prof. Mehmet Bayındır for their efforts to establish UNAM.

I would like to thank all my group members: Tuğrul Ç. Cinkara, Tural Khudiyev, Mehmet Kanık, Enes Korkut, Bihter Dağlar, Hülya Budunoğlu, Erol Özgür, Ekin Özgür, Ozan Aktaş, Adem Yıldırım, Yunus Çetin, Muhammet Çelebi, M. Halit Dolaş, Pınar Beyazkılıç, Dr. İbrahim Yılmaz, Dr. Gökçen B. Demirel, Dr. Mecit Yaman and Dr. Hakan Deniz. I also would like to thank all my friends: S. Bilal Çay, Enes Bilgin, Fatih Büker, Semih Yaşar, Deniz Kocaay, Feyza Oruç, Mustafa Ürel, Sencer Ayaş, Fatih B. Atar, Ali C. Kösger and Abdullah Gülle. Also, I would like to thank Daniel L. Thames for editing.

I wish to give special thanks to my parents Remziye and Ziya Duman, my sister Nur H. Duman and my dear fiancé Elif Aydın for their eternal love, support, patience and encouragement.

Finally, I would like to thank TÜBİTAK for their financial support through 2210 and 2224 coded scholarships.

Contents

List of Figures

Chapter 1

Introduction

In all the parts of our daily life, we use optics and optical devices such as mirrors, glasses, monitors, detectors, etc. Optics is one of the very first branches of science and it is still advancing. In the last several decades, a new sub-branch of optics emerged because of improvements in nanotechnology and nanoscience. We can define plasmonics as nanoscale optics [1]. In contrast to conventional optics, metals are key materials for plasmonics. Coherent free electron oscillations in metals allow concentration and propagation of light in sub-wavelength scales at metal-dielectric interfaces as surface plasmons (SP). The unique property of plasmonics which we can confine light into sub-wavelength dimensions, allows us to fabricate on-chip optic circuits where we can manipulate, amplify or generate light.

Recently one of the critical plasmonic devices used is optical nanoantennas. They enable optimum conversion of propagating light into sub-wavelength localized optical fields by resonant oscillations of free electrons in nanoscale metallic structures. Concentrating light into very small volumes by localized surface plasmons (LSP) leads to electric field enhancement, which is more than three orders of magnitude, especially at the corners and sharp tips of the structure [2, 3]. Thus, nanoantennas allow increasing of light-matter interactions in the near field of the nanoantenna. These resonant nanostructures provide strong near field enhancement at specific wavelengths [4]; therefore, they are used for many technological

applications that include spectroscopy [5], optical trapping [6], tumor therapy [7], detection, manipulation and generation of light [8, 9, 10].

The creation of new frequency components from narrow band and high energy input pulses is required for all optical signal processing and spectroscopic optical applications [11]. Silica and other materials, such as lead-silicate, bismuth and chalcogenide glasses, with higher nonlinear coefficients are used in fibers to observe new frequency generation [12, 13, 14]. Recently, threshold energy for initiating continuum generation reduced significantly in fiber geometry [15]. However, generated frequencies require further amplification, because converted power is insufficient for direct use in applications. Also, fiber fabrication and tapering are somewhat burdensome. To achieve supercontinuum, one needs to compensate waveguide and material dispersion at specific wavelengths and fiber diameters. Additionally, for supercontinuum generation, propagation length is the key factor; pulse can be distorted due to higher order dispersions and material absorption during propagation. Therefore, nanoantennas can be employed instead of fiber waveguides to increase light matter interaction by storing incident light at resonant length. Thus, optically nonlinear materials within the antenna near field can generate new frequency components suitable for on-chip applications. Thanks to the recent advances in nanofabrication, nanoantennas could be fabricated on nonlinear thin films by using different techniques. There are some experimental and theoretical studies which use bowtie [11] and dipole [2, 16] type nanoantenna for observing nonlinear effects.

Resonant nanoantenna is a proper medium for nonlinear interactions. As the propagating laser beam incident on nanoantenna surface it is converted to evanescent wave, which decays through the high index chalcogenide glass substrate. Though, phase matching satisfied both on antenna edge and dielectric-antenna surface. Dielectric-antenna surface is a convenient medium for allowing stored electromagnetic energy to decay through the nonlinear chalcogenide glass material. In resonant nanoantenna structures, it is expected that incident light efficiently converted to harmonic generation. Here, however, nonlinear material is not resonant itself, therefore it use power enhanced by the antenna. Even in

lower values of pulse energy third harmonic generation can occur due to suitable nanoantenna medium. Self-phase modulation based broadening starts when threshold power is reached. As a result, incident light energy is distributed to both supercontinuum and harmonic generations by the features of both nanoantenna and nonlinear material systems. Upon threshold of supercontinuum generation, it is expected that all pumped energy is converted to harmonic generation in terms of nonlinear processes.

In this thesis, we investigated the low threshold nonlinear generation by using single stripe and rod shaped resonant optical nanoantennas on chalcogenide glasses. We combined the two significant and distinguished properties of optical nanoantennas and chalcogenide glasses to reduce trigger power for nonlinear phenomenon. We used the increase in light material interaction by near field intensity enhancement of resonant optical nanoantennas and the high nonlinear refractive index of chalcogenide glasses. Furthermore, we explored effects of shape of the antenna, substrate material and dimensions of the antenna on resonant length and optical nonlinear generation by finite difference time domain (FDTD) simulations. Finally, we fabricated the proposed antenna structures by three different fabrication techniques: electron beam lithography, seed-mediated chemical technique and electro deposition of anodic aluminum oxide templates.

This thesis is organized as follows: Chapter 2 deals with theoretical background of resonant plasmonic antennas, chalcogenide glasses and optical nonlinear effects. Chapter 3 includes details of simulated structures, simulation parameters and results. Chapter 4 contains the information about fabrication steps and results of all techniques which we used to produce nanoantennas. Lastly, chapter 5 concludes the thesis and proposes future work about the topic.

Chapter 2

Theoretical Background

2.1 Plasmonic Nanoantennas

Nanoantennas are the short-wavelength equivalent of the conventional antennas [17], and they can transmit and receive ultraviolet (UV), visible (VIS) and infrared (IR) light resonantly. Windows with red and yellow colors during the medieval era included gold and silver nanoparticles [18]. A nanoantenna is nothing but a metallic nanoparticle. By the localized surface plasmons (LSP) they can confine light into extremely small volumes [18, 1]. Collective oscillations of free electrons on resonant nanoantennas create hot spots at the near-field of the antenna. If we excite a metallic nanoparticle with electro-magnetic wave, conduction current will be generated on the particle. Oscillation frequency of this current is same with the frequency of incoming electromagnetic wave. On the particle free electrons moves collectively from one side of the particle to the other. Electric field created by these oscillations and localized components makes electric field at the near-field of nanoantenna greater than incident electric field. These hot spots enhance light-material interactions and pave the way for many technological applications. In recent years, nanoantennas are used for cancer treatment [7, 19], surface-enhanced Raman spectroscopy [20], biological sensing [5], near-field probes [21] and enhancing florescent of molecules [22, 23]. Other works

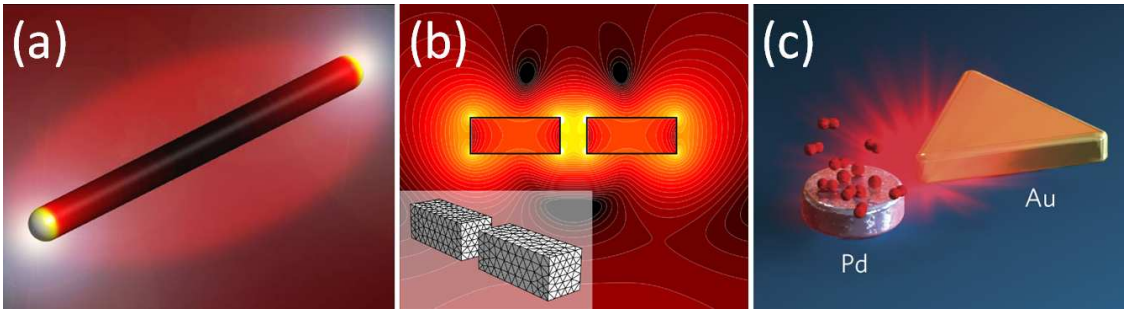

Figure 2.1: Some examples for optical antennas. (a) Single rod nanoantenna and electromagnetic field distribution around the antenna (Ref. [29]). (b) Dipole antennas confine electromagnetic field into their feed gap (Ref. [30]). (c) Bow-tie antennas confine light at their sharp edges (Ref. [28]).

about nanoantennas include imaging single quantum dot [24, 25], improving size mismatch between light [26], fluorescent molecules and two-photon luminescence with nanoantennast [2], spectroscopy of single gold nanoparticle [11], nonlinear response of bowtie nanoantennas [27], trapping of 10 nm nanoparticles [6], spectroscopy of protein monolayer [5] and nanoantenna enhanced gas sensing [28].

Antenna length and polarization of the incoming light affect the resonant wavelength of the nanoantenna. Mühlschlegel *et al.* show this in their work about the resonant optical antennas [2]. In the work, dipole stripe antennas are used for enhancing incoming electromagnetic waves. FDTD simulations are performed to determine resonant wavelength of gold nanoantenna. Researchers fabricate resonant nanoantennas at desired lengths and shine femtosecond laser pulses at 560 nm. At the output, they observe white light supercontinuum generation. This is the first work about the resonant nanoantennas and their application in nonlinear frequency generation. Figure 2.2 shows SEM images of the fabricated antennas and localization of incoming light for different antennas and polarization of light.

Linear responses of nanoantenna also affect the nonlinear response of the system [31]. Hentschel *et al.* investigate the relation between linear response and

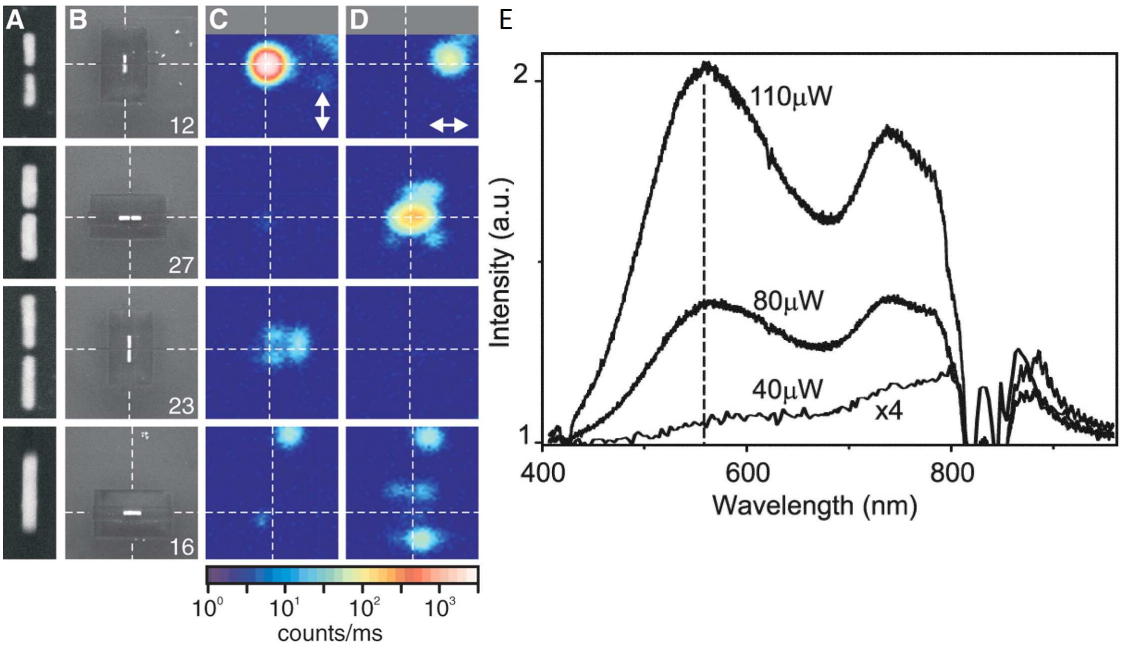

Figure 2.2: Some examples of optical resonant antennas. (a-b) SEM images of the resonant antennas. (c-d) Confocal image of white light supercontinuum generation for TE and TM polarizations. (e) Spectra of the supercontinuum generation for different input intensities (Ref. [2]).

nonlinear response of nanoantennas, and they claim that nonlinear spectral properties of nanoantennas are fully determined by the linear response of the antenna. Dipole bow-tie antennas are excited with 817 nm wavelength 8 fs pulse length laser pulses in this work. Researchers determine the resonance wavelength for different nanoantennas with same size and different gap sizes. Also, they examine the generated third harmonic wavelength for these different structures. Results show that shift in resonance lengths leads to a shift in wavelength of generated third harmonic (Fig. 2.3). Therefore, to estimate nonlinear response of antenna by checking the linear response of it they model the resonance frequency of the antenna like a harmonic oscillator with the parameters: resonance frequency, mass, intrinsic damping constant, charge and perturbation term. The developed nonlinear oscillator model is tested with different size and gap sizes of bow-tie antennas. Also the inspecting effect of the shape of the antenna response stripe dipole antennas is measured. Lastly, they check the effect of refractive index of

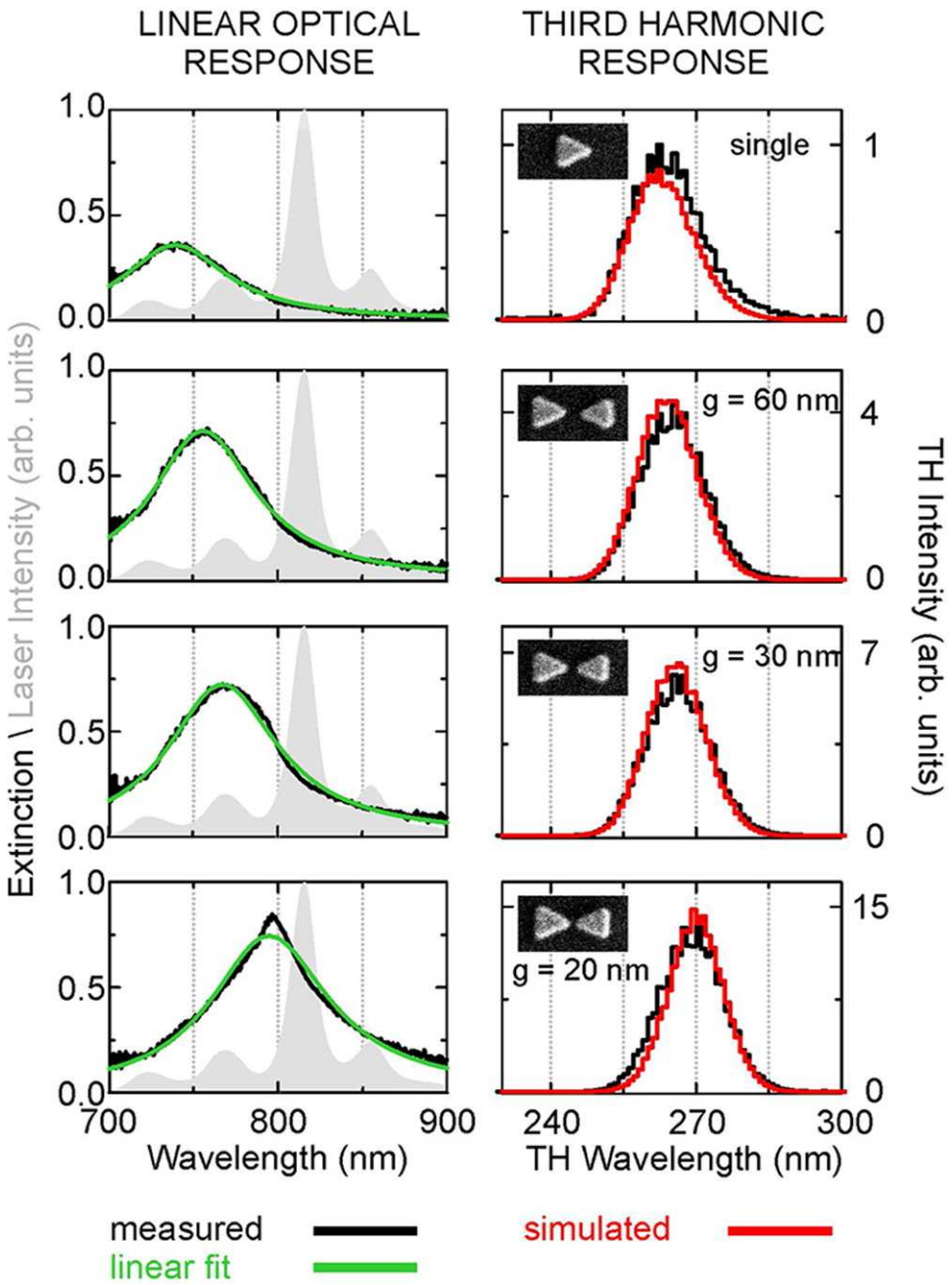

Figure 2.3: Left column is linear response of the antennas and the right column is nonlinear response of the antennas. Antennas have different gap sizes but the edge sizes of the antennas are same. Shift on the linear response of the antenna leads the shift on the nonlinear response of them (Ref. [31]).

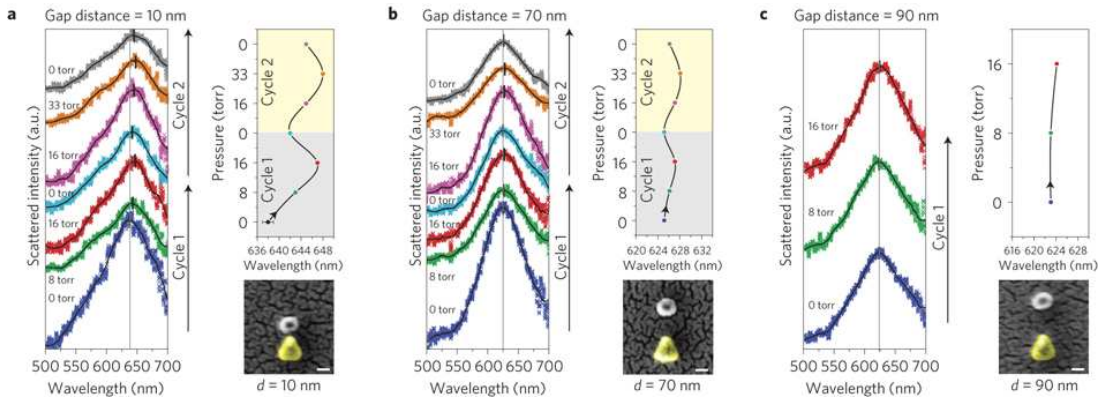

Figure 2.4: Optical scattering measurements for palladium-gold system under the hydrogen gas flow. (a) Measurement results for 10 nm gap between gold bow-tie antenna and palladium particle. (b) 70 nm gap size and (c) 90 nm gap size. Scale bar for SEM images is 50 nm. For measurements pressure of the hydrogen gas starts from 0 torr and raises to higher pressures. There are two cycle of measurement for each figure (Ref. [28]).

medium and coat the bow-tie antennas with SiO_2 glass. Results of the experiment show a good agreement with simulated signal and measured signal. They conclude that nonlinear response of nanoantennas is directly related with linear responses of the structures.

There are several variables which affect the resonance wavelength of nanoantennas [18]. One of these variables is dielectric permittivity of the materials at the near field of nanoantenna. That unique property of nanoantennas enables single particle sensing for detectors [28]. Liu and her colleagues sense hydrogen in nanoantenna enhanced system at single particle level. They placed a single palladium particle at the near field of gold nanoantenna and detect the change in optical properties of the system when hydrogen exposed on the system. For this work, a circular palladium particle is fabricated close to the tip of the gold triangular nanoantenna by two-step fabrication of electron beam lithography. Then, scattering electromagnetic field from the structure is measured for different gas pressures. These different gas pressures lead to different peak points at scattering spectra of the system. Increase in gas pressure shifts resonant frequency of the

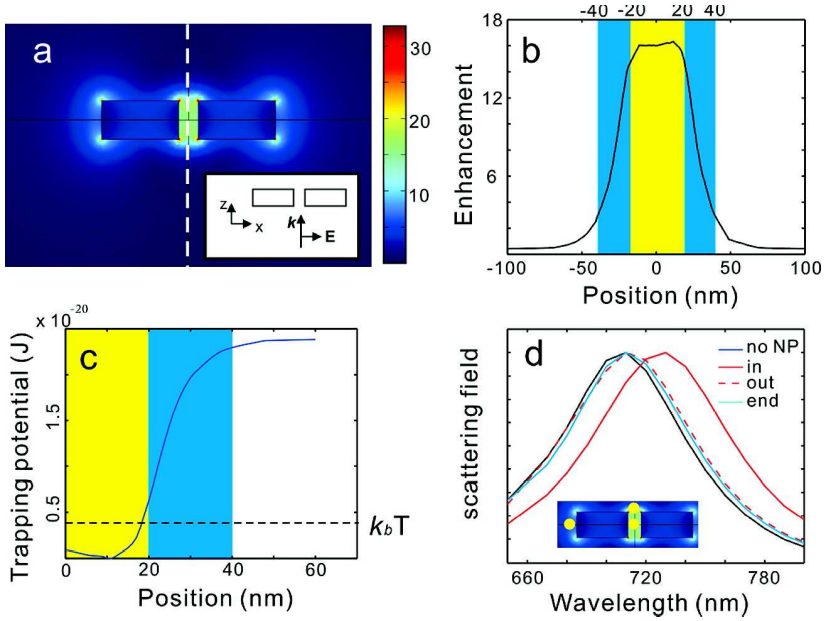

Figure 2.5: (a) Simulated electric field distribution of 80 nm arm length and 25 nm gap size dipole antenna. The inset is the schematic illustration of the antenna structure. (b) Electric field enhancement of the system on the dashed line given at (a). 0 point in the graph is the mid-point of the dipole antenna. (c) Trapping potential of the localized electric field. (d) Resonant spectrum of the antenna with particle at different locations around the antenna. The black curve corresponds the resonant spectrum of the antenna without any particle. The red one is the particle at the feed gap of the antenna (Ref. [6]).

system to red. Hydrogen absorption change the dielectric permittivity of the palladium which affects the interaction between gold nanoantenna and palladium. Therefore, according to change in resonant wavelength of the system one can detect the pressure of hydrogen gas. Figure 2.4 shows the measurement results and resonant length shift with respect to gas pressure.

High intensity enhancement ability of nanoantennas reduces necessary source power for some high intensity required applications. An example for this kind of application is trapping and sensing of nanoparticles. Zhang *et al.* overcome the necessity of high laser power to overcome Brownian motion by using dipole nanoantennas [6]. Furthermore, sensing trapped particles in real time is another

challenge. Thanks to localized surface plasmon resonance (LSPR) shifts they overcome this problem. Since nanoantennas enhances incoming electromagnetic waves by localizing them at their near-field about three orders of magnitudes, it reduces necessary input power for trapping a particle. Moreover, LSPR of dipole antennas shifts significantly by the change of dielectric constant at the gap of antenna, so it is easy to check whether there is a particle at the feed gap or not by observing scattering response of the system. Figure 2.5 shows the simulations results for designed structure. Researchers fabricate different dipole antennas with gap size vary from 5 nm to 30 nm by e-beam lithography, and they measure the scattering response of the antennas in the deionized water without any Au particles inside it to have a background of the clean system. Then, Au particles are added inside the water, and the same measurements are performed. For the first case, they measure resonance wavelength as 690 nm and for the second case 50 nm red shift occur at LSPR. Results indicate that a particle exists which is trapped at the gap of dipole antenna.

Another example for reduced necessary input power for application is nanoantenna enhanced nonlinear spectroscopy of single gold nanoparticle [11]. Schumacher *et al.* increase signal amplitude by ten folds on gold particle by locating it at the near-field of antenna. To determine the nonlinear transient absorption signal of nanoparticle caused by mechanical breathing oscillations, they employ nanoantenna. They use 70 nm diameter plasmonic gold nanodisc as nanoantenna, and they investigate smaller diameter, 40 nm, gold nanoparticle. This particle has weak optical scattering signals and transient absorption is almost non detectable. Observations of researchers show that transient absorption signal is enhanced in the presence of nanoantenna close to the particle. Also, they use polarization dependency of the structure as an on-off switch. It is possible to switch the antenna enhancement by changing the polarization direction. Moreover, by focusing laser pulse on nanoantenna-object couple, the electron gas and lattice are heated up. This starts mechanical breathing oscillations of the particle in a picosecond time scale. Therefore, particles begin to mechanically oscillate with the help of antenna. However, observing oscillation peaks of particle without antenna is not possible. Figure 2.6 includes oscillation peaks of system both with and without

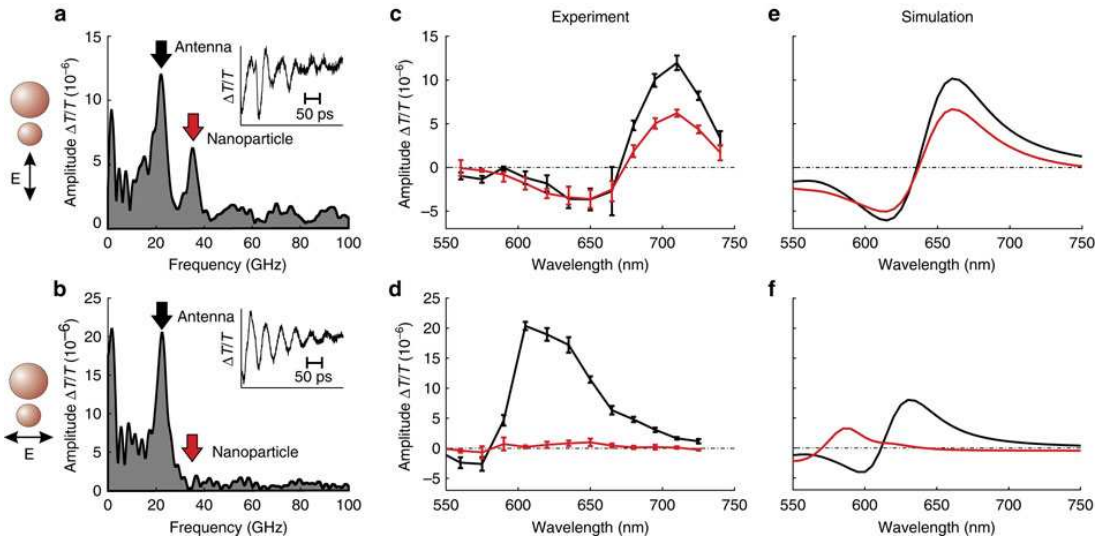

Figure 2.6: Experimental and simulation results of the coupling of the light to nanoparticles. Upper row is polarization along the particles and the lower row is polarization with perpendicular to first one. Red lines are the response of the nanoparticle and the black lines are the response of the antenna. There is nanoparticle mode in (a) but since the coupling is weak in (b) there is no nanoparticle mode. However, there is nanoantenna mode both for (a,b). (c,d) Oscillation amplitude spectrum for different polarizations. (e,f) Simulation results of oscillation amplitude spectra for different polarizations (Ref. [11]).

antenna cases.

Nanoantennas have some applications in array configuration also. Ko *et al.* employ gold bowtie nanoantenna arrays for nonlinear frequency generation [27]. Since nanoantennas enhance incoming electromagnetic waves by more than three orders of magnitude, they are useful for starting nonlinear phenomena. They use the property of confinement of light at feed gap of bowtie antenna to second harmonic generation and two-photon photoluminescence. Fabricated structures are 50 nm thickness, 140 nm side length and 20 nm gap size gold bowtie antennas which are resonant at 780 nm wavelength (Fig. 2.7). Nanoantennas are on the 25 nm ITO coated glass in array configuration with 4 different spacings. Researchers simulate these different arrays by finite difference time domain technique and determine the resonant length of each system. Results show that different spacing

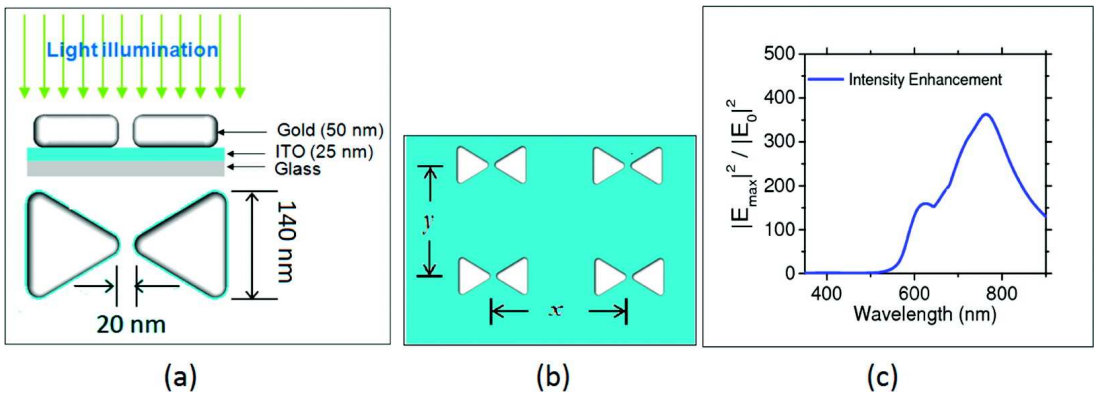

Figure 2.7: (a) Schematic illustration of the dipole bow-tie antenna system. They are placed on 25 nm ITO coated glass substrate. (b) Field distribution of the array configuration of bow-tie antenna systems. x and y defines the center to center distances. (c) Intensity enhancement spectra of the antenna. It is resonant around 750 nm wavelength (Ref. [27]).

in array causes different resonant wavelength for the system. To measure the nonlinear response of the structure the system is pumped with 780 nm wavelength 100 fs pulse length and 80 MHz repetition rate laser pulse. The pump wavelength filtered out to measure the second harmonic generation of the system. As a result, they prove that bowtie nanoantennas can be employed as periodic arrays to increase intensity enhancement and by changing array lattice one can manipulate the resonant wavelength of the structures. Furthermore, they observe second harmonic generation and two-photon photoluminescence by exciting the system.

Nanoantennas have application areas in biology such as spectroscopy of proteins or other molecules. Adato *et al.* demonstrates ultra-sensitive vibrational spectroscopy of protein monolayers with nanoantenna arrays [5]. Intrinsic absorption cross-sections of infrared (IR) active modes of proteins are not enough to sense. However, by enhancing this property with nanoantenna arrays, it is possible to sense monolayer proteins. Near-field localization of nanoantenna arrays enables more than four orders of magnitude intensity enhancement so they are helpful for that application. Like surface enhanced Raman spectroscopy (SERS), surface enhanced infrared absorption spectroscopy (SEIRA) is a technique also

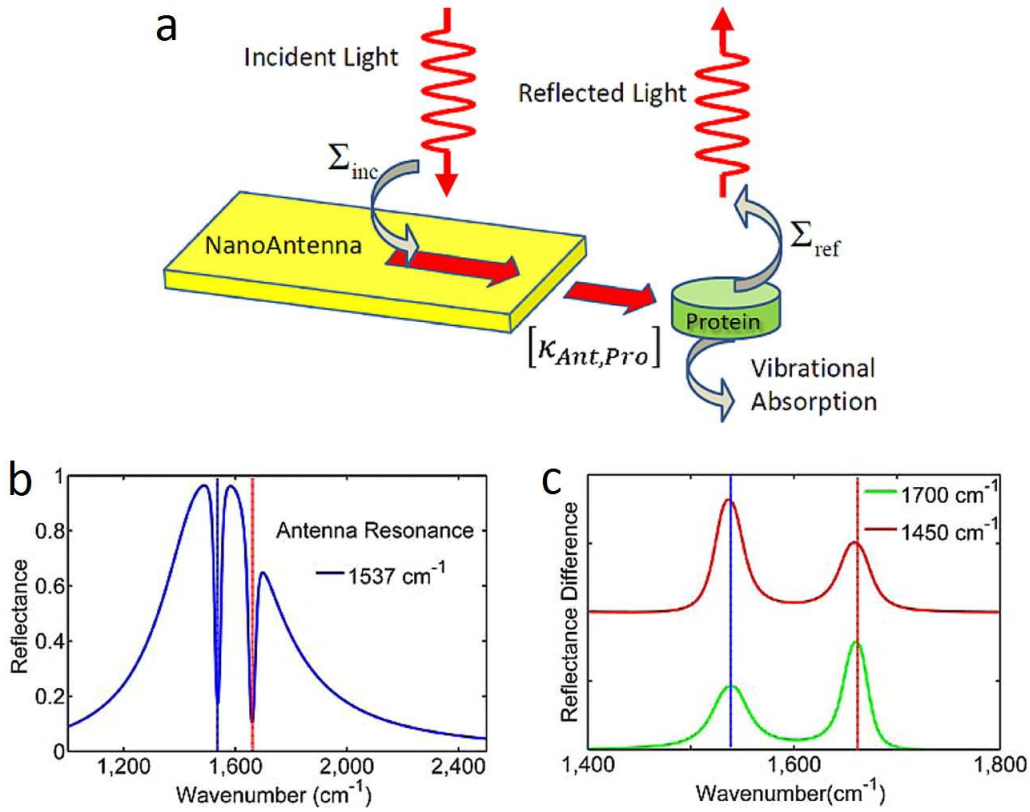

Figure 2.8: Schematic illustration of the system. (a) Incident light causes coupling between the antenna and the protein. (b) System shifts from its self resonance point if there is a protein load at the near field of the antenna. (c) Resonance of the antenna is tuned to 1450 cm^{-1} and 1700 cm^{-1}, but their strength changes with the adding protein to near field of the antenna (Ref. [5]).

for spectroscopy of materials. For SEIRA chemically prepared or roughened surfaces common to use, but enhancement factor of these surfaces are limited to 10-100 range. On the other hand, enhancement factor of nanoantenna arrays much greater than this. In their work Adato *et al.* use stripe nanoantenna arrays. Firstly they determine the resonant length of single antenna by FDTD simulations and fabricate these arrays by using lithography techniques (Fig. 2.8). Thickness of the antenna is 70 nm and the length is 1100 nm, antenna material is selected as gold. After fabricating the antennas, researchers coat silk fibroin proteins on them by spin coating. Coating proteins on antennas causes red shift

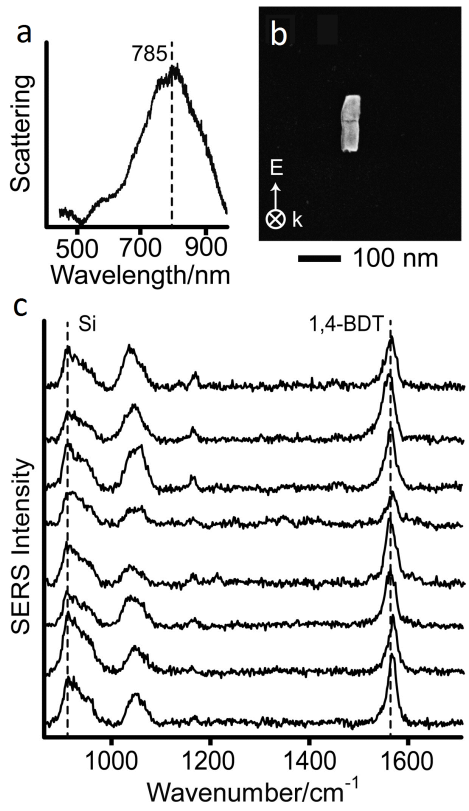

Figure 2.9: SERS measurement of a single particle (a) Resonant spectra s a dipole antenna used in the study. (b) SEM image of a dipole antenna fabricated by on wire lithography technique. Inset is the propagation direction and the polarization of the incident light. (c) SERS spectra of different dipole antennas. Resonant wavenumbers are different for each dipole (Ref. [20]).

at the resonance wavelength of the antenna. However, enhancement value of system is enough for SEIRA measurements. According to this work we can say that nanoantenna arrays enhances light at their near-field and this can be used for enhancing SEIRA signals to sense protein monolayers.

New fabrication techniques for producing nano scale metallic structures open up new possibilities for plasmonic nanoantenna applications. Osberg *et al.* develop a new technique to fabricate dipole gold nanoantennas and use this antennas for SERS application [20]. By using on-wire lithography (OWL) technique they

fabricate 35 nm diameter 5 nm gap size gold dipole nano rod antennas. This fabrication technique has some advantages: existence of physical support fixes gap size, finely control of length and gap size of structure and high yields of particles. Researchers select 785 nm for excitation wavelength and determine the resonant length of antenna pair by performing FDTD simulations. Then SERS measurements are performed for different nanoantenna systems. Figure 2.9 includes scattering spectrum of fabricated antennas and SERS spectra measurements. Results show that employing dipole gold nanoantenna increases measured SERS signals to have more reliable data. This work differs from others because of the fabrication process of the nanoanatennas. In most of the studies nanoantennas are fabricated by electron beam lithography on a substrate. However, Osberg *et al.* fabricate these structures by using OWL and antennas fabricated in a liquid.

Dipole nanoantennas confine electromagnetic waves in the feed gap and O´Carrol *et al.* use this confinement feature of nanoantennas to enhance the radiative emission rate of P3HT [32]. They fabricate dipole nanoantennas. The feed gap of the antennas are filled with P3HT. Antennas are fabricated by electro deposition of anodic aluminum oxide membrane template. After deposition of first arm of the antenna, they deposit P3HT and thermally evaporate next arm of the antenna. Before the fabrication FDTD simulations are done to determine resonant length and have an insight about the enhancement of decay rate. Figure 2.10 represents schematic illustration of nanoantenna system and FDTD simulation results about electromagnetic field profile around the antenna and at the feed gap. Moreover, simulation results about the enhancement on radiative decay rate are presented, and it is more than 50 for first resonant mode. Researchers use 375 nm picosecond laser for measurements. At the measurement results radiative emission rate is enhanced by the factor of 29. These results are consistent with FDTD simulation results.

Since nanoantennas localize incoming electromagnetic waves they increases light and matter interaction. This property of nanoantennas can enhance the efficiency of thin-film solar cells by trapping light [33]. Simovski *et al.* propose planer nanoantennas on photovoltaic solar cell (Fig. 2.11). Researchers design antenna arms perpendicular to each other to localize all polarizations of light,

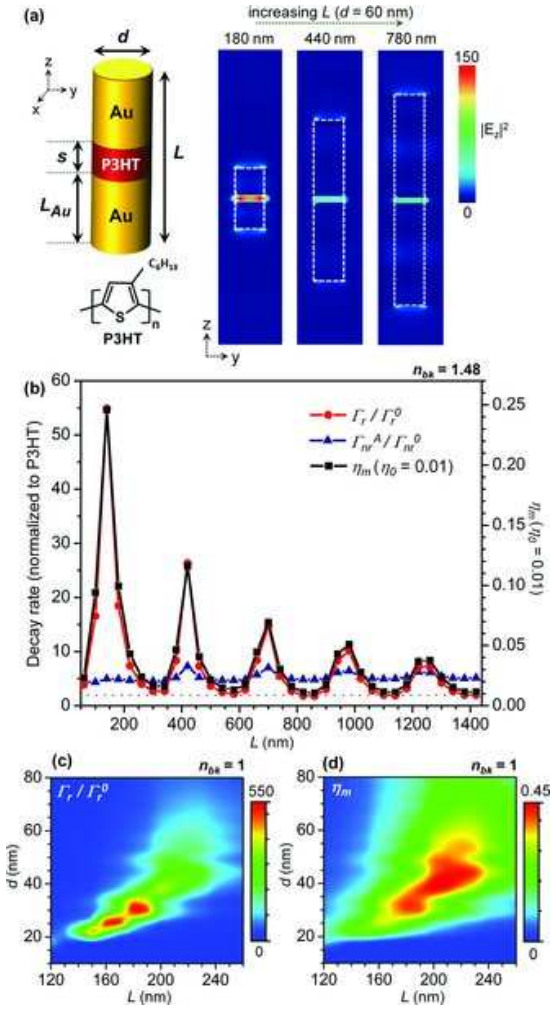

Figure 2.10: Design and theoretical results of the dipole antenna system.(a) Schematic illustration of the dipole antenna with P3HT in the feed gap of it. Chemical molecule structure of the P3HT. Electric field distribution of the incident electromagnetic field for different antenna lengths. (b) Simulation results of radiative and non-radiative decay rate change according to antenna length. Also modified quantum efficiency of a dipole emitter is given according to length of the antenna. (c) Theoretical results of radiative decay rate change according to length and the diameter of the antenna. (d) FDTD results of quantum efficiency enhancements as a function of length and diameter of the antenna (Ref. [32]).

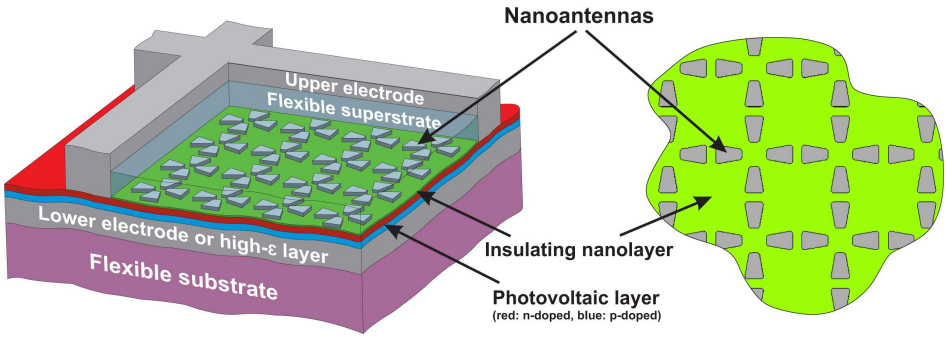

Figure 2.11: Schematic of layers of thin-film solar cell with light trapping nanoantenna structure on it (Ref. [33]).

so their solar cell works independent from polarization of incoming light. They optimize the sizes of antennas and layer thickness of the solar cell by some sets of simulations for different wavelengths. They claim that they can reach high efficiency even they use only 110 nm photovoltaic layer by adding light trapping nanoantenna structure on it. The important part of the research is, designed structure works in a broad range of visible and infrared parts of the spectrum. According to the results in the paper, nanoantenna design on a solar cell works better than anti-reflective coatings.

2.2 Chalcogenide Glasses

Chalcogenide glasses are the materials which contain at least one chalcogen element from group 6a of the periodic table, S, Se and Te, and other elements such as As, Ge, Sb, etc (Fig. 2.12). These glasses are optically sensitive the absorption of electromagnetic waves, transparent in infrared and highly nonlinear [16, 34]. Therefore, they have lots of application areas including nonlinear optics, phase change materials, imaging and sensing.

One of the most important properties of chalcogenide glasses is sensitivity to electromagnetic waves in another way photosensitivity. Exposing light, heat,

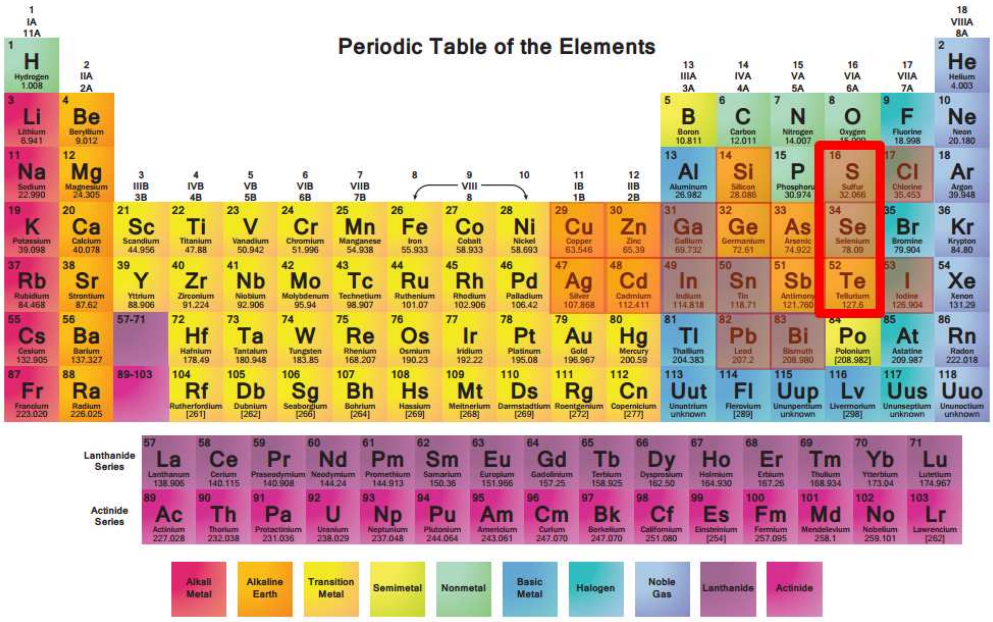

Figure 2.12: Periodic table of the elements with chalcogen elements are highlighted with red rectangle.

x-ray or electron beams to chalcogenide glasses change their chemical bond structure. This property of the materials makes them attractive for phase change memories [35], photodarkening [36], photodiffusion [37] and photocrytallization [38]. Another important property of chalcogenide glasses is transparency at infrared region. They are transparent especially at 2-25 μm band for different glasses and compositions [34]. This makes them attractive for infrared transmitting optical fibers and waveguides. Most of the losses in these fibers are caused by impurities and bubbles in the fiber. There are several techniques for fabricating these fibers such as core drilling, rotational casting and thermal drawing [16]. Fabrication technique affects the quality of the fiber and losses due to scattering. For different applications planner waveguides have better performance than optical fibers. In those applications chalcogenide glasses are in thin film form. Chalcogenide thin films can be produced by thermal evaporation, sputtering and pulsed laser deposition. After fabrication of thin film, annealing step is necessary to relax the chemical bounds. Otherwise, chalcogenide thin film lift-off from the substrate [34]. Also there are several methods for patterning thin film chalcogenide

glasses such as, photodarkening, lithography, lift-off and wet etching. All these techniques have both advantageous and disadvantageous. Fiber or waveguide geometry of chalcogenide glasses are used for different sensing applications other than just transmitting infrared light. Spectroscopy of liquid or vapor can be performed by monitoring transmission of a chalcogenide fiber in these mediums. There are some chemical sensors which include chalcogenide glasses in waveguide geometry which use evanescent wave or Raman spectroscopy. Advantages of these sensors are small size, reproducibility and easy integration with sources. Chalcogenide glasses have high refractive index n_0 about 2-3. High linear refractive index leads high nonlinear refractive index n_2. Chalcogenide glasses have three orders of magnitude greater third order nonlinear coefficient $\chi^{(3)}$ than silica glass [16]. This makes these materials attractive for nonlinear optics applications such as ultra-high bandwidth signal processing and self phase modulation. Therefore, they have key roles in ultra-high bandwidth optical communication systems in the future. Chalcogenide glasses are used in the device for four-wave-mixing gain, demultiplexing and regeneration. Moreover, they are used as efficient supercontinuum generators.

Supercontinuum generation is useful for spectroscopy, laser frequency metrology and optical imaging applications. Moreover, it has interest as a fundamental research. Yeom *et al.* employ chalcogenide fiber, As_2Se_3, as low threshold supercontinuum source [14]. They taper fiber sub-micrometer dimensions by flame brushing technique and engineer it as has zero dispersion at 1550 nm. Measurements are performed under excitation of 1550 nm laser beam and figure compares simulation and measurement results. Wide spectrum broadening and low input power shows that chalcogenide fibers are attractive devices for low threshold supercontinuum generation.

It is possible to use two different chacodenide glasses in a fiber by core-shell configuration. Shabahang *et al.* proposes a fiber configuration with high refractive index chalcogenide core, $As_2Se_{1.5}S_{1.5}$ (n=2.743), and low index chalcogenide shell, As_2S_3 (n=2.472), for nonlinear supercontinuum generation [39]. Since the refractive index of core material is higher than shell material confined electromagnetic field inside to the fiber will propagate along the fiber by total internal

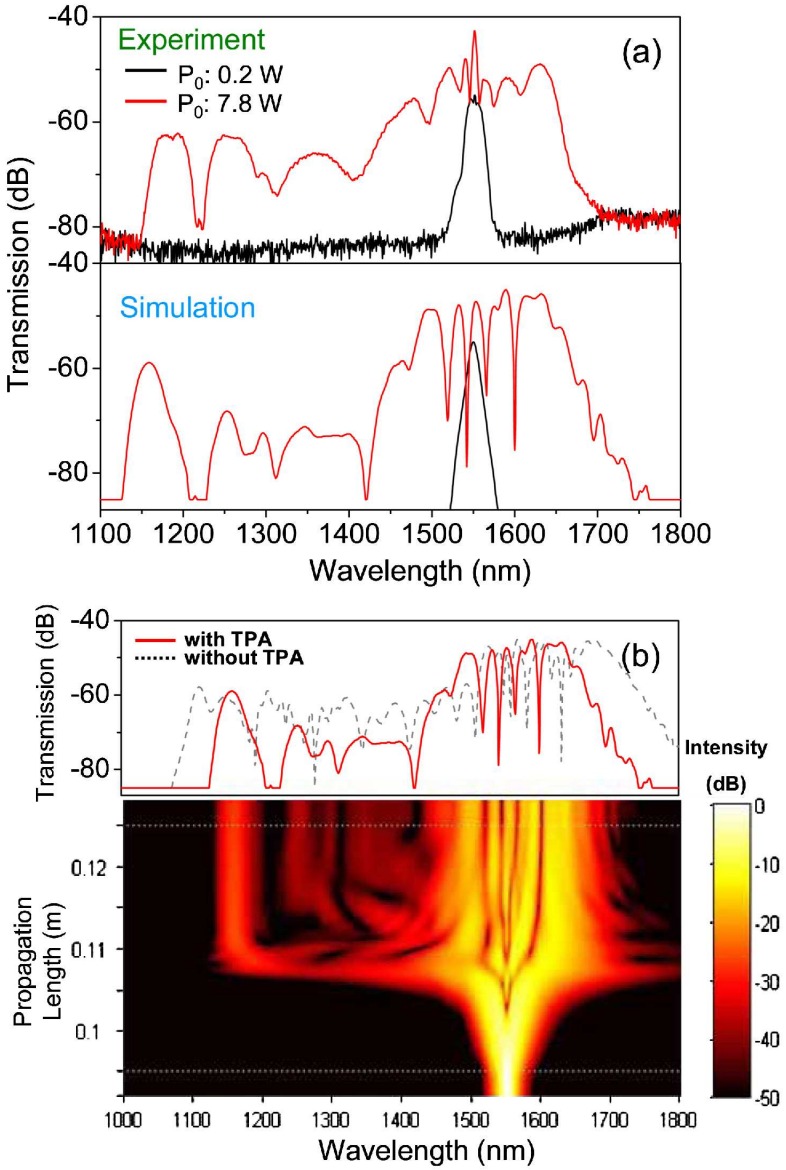

Figure 2.13: (a) Comparison of experimental results with numerical simulation results for different power levels (black curve: P_0= 0.2 W ; red curve: 7.8 W). (b) Spectra of pulse while propagating along the As_2Se_3 fibers at P_0= 7.8 W. The dotted curve in the graph shows the boundary of the fiber waist. (Ref. [14])

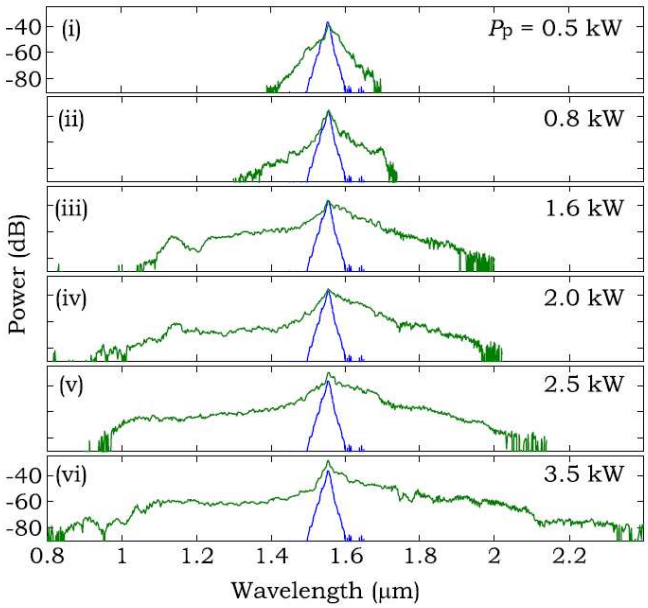

Figure 2.14: Input laser spectrum and spectral broadening at the end of the chalcogenide fiber for different pump power (Ref. [39]).

reflection. Researchers fabricate the fiber by using iterative size reduction technique and diameters of the core and cladding are 10 and 35 μm respectively. By shining 1.55 μm high power laser beam inside the fiber they generate supercontinuum from 850 nm to 2.35 μm. Figure 2.14 shows spectral broadening for different power inputs. Research shows that higher power inputs allow higher spectral broadening.

2.3 Nonlinear Optics

Applied electromagnetic field on dielectric medium excites the bound charges and oscillates the electrons around the nucleus. For low intensities these electrons oscillates linearly. However, when the strength of the electromagnetic wave is greater than 1% of binding potential of the electrons they start anharmonic oscillations. These non-linear oscillations cause new frequency generation in material.

Polarization of a material is described as the Formula 2.1 in linear regime [34, 40].

$$P = \varepsilon_0 \chi^{(1)} \cdot E \tag{2.1}$$

In the equation ε_0 is the vacuum permittivity and $\chi^{(1)}$ is the linear dielectric response tensor. This formula is a great approximation for low intensity cases. However, relation between polarization and electric field is formulated in Equation 2.2 for both low and high intensity cases.

$$P = \varepsilon_0(\chi^{(1)} \cdot E + \chi^{(2)} \vdots EE + \chi^{(3)} \vdots EEE + \ldots) \tag{2.2}$$

$\chi^{(1)}$ is mostly related with linear refractive index n_0 and it is the most dominant coefficient in the equation. $\chi^{(2)}$ drives the nonlinear phenomenon called second harmonic generation, sum and difference frequency generation and optical parametric oscillation. $\chi^{(2)}$ is only non-zero for materials which has inversion symmetry; however all the materials with inversion symmetry do not have non-zero $\chi^{(2)}$ value. $\chi^{(3)}$ is responsible for nonlinear optical effects called optical Kerr effect, self phase modulation, cross phase modulation, third harmonic generation, four wave mixing, two photon absorption, stimulated Raman scattering, stimulated Brillouin scattering.

We model the motion of electrons around the nuclei when low intensity light exposed on it, as harmonic oscillator. Electrons around the nuclei oscillate just like a mass attached to a fixed point by a spring [34, 40]. Force on electron because of electric field is given by Equation 2.3.

$$f = eE \tag{2.3}$$

Where e is charge of electron and E is electric field. Restoring force on electron is given by Equation 2.4.

$$f_{res} = -m\omega_0^2 x \tag{2.4}$$

Where m is the mass of electron, ω_0 is frequency of oscillation and it is equal to excitation frequency. Lastly, x is displacement. Since the force is mass times acceleration also if we consider the damping ratio, ς, we can obtain Equation 2.5.

$$\frac{d^2x}{dt^2} + 2\varsigma\frac{dx}{dt} + \omega_0^2 x = -\frac{e}{m}E \tag{2.5}$$

Solution of the differential equation is

$$x = -\frac{e}{m}E\left(\frac{e^{i\omega t}}{\omega_0^2 - 2i\varsigma\omega - \omega^2} + \frac{e^{-i\omega t}}{\omega_0^2 + 2i\varsigma\omega - \omega^2}\right) \tag{2.6}$$

Solution shows that displacement is linearly proportional with electric field E and excitation frequency is same with the frequency of electron motion. Therefore, frequency of radiated wave from the motion of electron is same with excitation frequency but with a phase delay.

We can model the nonlinear motion of electrons by introducing high order terms to restoring force such as ax^2 and bx^3. In that case we have restoring force as

$$f_{res} = -m(\omega_0^2 x + ax^2) \tag{2.7}$$

where a is the parameter which indicates the strength of the nonlinearity.

Then we should consider this term in Equation 2.5 and obtain new equation. The solution of this equation is in the form of

$$x = x_1 + x_2 \tag{2.8}$$

where x_1 is the same solution with Equation 2.6 and x_2 has the solution in the form of

$$x_2 = x_2(2\omega) + x_2(0) + x_2^*(2\omega) + x_2^*(0) \tag{2.9}$$

In that case $2w$ term comes and causes second harmonic generation.

Like ax^2 term bx^3 drives third-order nonlinear generations. For the materials which have third order nonlinear coefficient nonlinear polarization is [40]

$$P_{NL} = 4\chi^{(3)}E^3 \tag{2.10}$$

Therefore nonlinear polarization contains two different components, one of them at frequency ω and the other one at 3ω.

$$P(\omega) = 3\chi^{(3)}|E(\omega)|^2E(\omega) \tag{2.11}$$

$$P(3\omega) = \chi^{(3)}E^3(\omega) \tag{2.12}$$

3ω components shows that there is third harmonic generation for the materials which have non-zero $\chi^{(3)}$ value.

Self-phase modulation is another nonlinear effect of third order nonlineaer coefficient. Propagating intense pulse in a nonlinear medium gain a new phase because of the nonlinear refractive index of the medium [34]. The nonlinear phase shift is given as

$$\phi(t) = -\frac{\omega_0}{c}n_2I(t)L, \tag{2.13}$$

where I is intensity, ω_0 is center frequency and L is length of propagation of the light. Therefore, intensity and length of the propagation directly related with the gained phase. Increase in these variables leads increase in acquired phase. Instantaneous frequency shift is given as

$$\delta\omega(t) = d\phi/dt \tag{2.14}$$

Continuum generation is an application of self-phase modulation. There is no frequency shift at the center wavelength of the incident wave but leading frequencies are red-shifted and trailing frequencies are blue shifted. These shift in different edges of pulse cause spectral broadening and continuum generation.

Finally, $\chi^{(3)}$ and n_2 are related coefficients with each other. The relation between these coefficients is given in Equation 2.13 [40] and by using this equation we determine the $\chi^{(3)}$ as input for FDTD Kerr material.

$$n_2 = \frac{3n_0}{n^2\epsilon_0}\chi^{(3)} \tag{2.15}$$

Chapter 3

Numerical Calculations

Simulations of proposed structures gives an insight into the results of the design and avoid wasting time and money with fabricating poorly designed systems. New advances in processor technology provide more computational power for simulation programs. Today's simulation results are more reliable, and they are almost same with real life measurements [5, 11, 18, 27]. In this study, we first simulate the proposed structures and follow by fabricating designs according to results of these simulations. In this chapter, we will present simulation structures and results for new frequency generation by enhancing optical intensity on chalcogenide glass (As_2Se_3, As_2S_3) substrate with localized surface plasmons (LSP) around the near field of gold resonant nanoantenna.

We simulate the structures by using commercially available Lumerical Finite Difference Time Domain (FDTD) software. FDTD method was first introduced by K. S. Yee in 1966 [41]. In FDTD method, space is divided into small meshes, called Yee cell (Fig. 3.1), by the software. Each unit cell has its constants according to the defined material. Software solves the time-depended Maxwell equations (Equ. 3.1 and 3.2) by replacing derivatives with finite differences for each mesh individually [42].

$$-\nabla \cdot \vec{D} = \rho, -\nabla \cdot \vec{B} = 0 \tag{3.1}$$

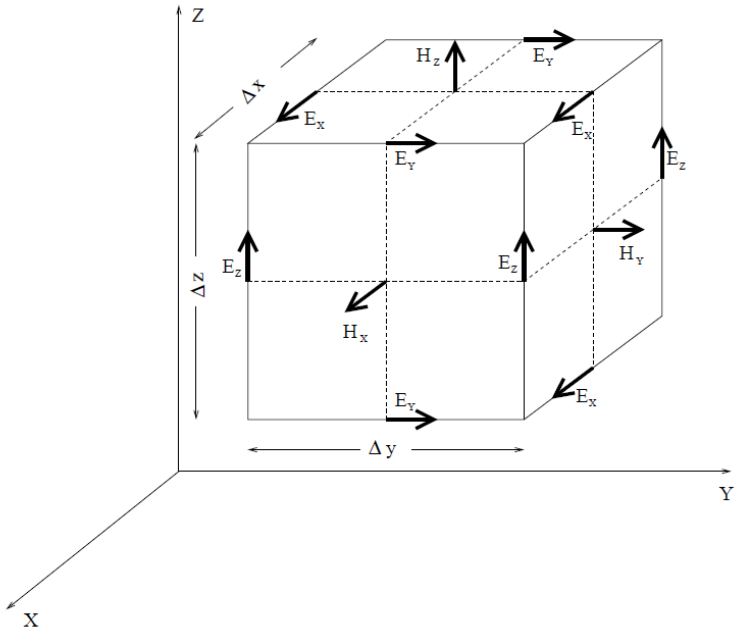

Figure 3.1: Schematic illustration of a Yee unit cell (Ref. [42]).

$$-\nabla \times \vec{\varepsilon} = \partial_t \vec{B}, \nabla \times \vec{H} = \vec{J} + \partial_t \vec{D} \tag{3.2}$$

To replace the derivatives in the Maxwell's curl equation FDTD technique algorithm uses central difference formula which is given in Equation 3.3.

$$\frac{df(x)}{dx} \tilde{=} \frac{f(x + \frac{\Delta x}{2}) - f(x - \frac{\Delta x}{2})}{\Delta x} \tag{3.3}$$

For each time step software first defines the magnetic field components and then calculates electric field components for unit Yee cell by solving derived equations (3.4, 3.5) from Maxwells curl equation by using central difference formula.

$$H_{i,j,k}^{n+0.5} = \vec{H}_{i,j,k}^{n-0.5} \frac{\mu_{i,j,k} - \sigma_{i,j,k}\Delta t/2}{\mu_{i,j,k} + \sigma_{i,j,k}\Delta t/2} + \frac{\Delta t}{\mu_{i,j,k} + \sigma_{i,j,k}\Delta t/2} \tilde{\delta}_r \vec{E}_{i,j,k}^{n} \tag{3.4}$$

$$E_{i,j,k}^{n+1} = \vec{E}_{i,j,k}^{n} \frac{\varepsilon_{i,j,k} - \sigma_{i,j,k}^{*} \Delta t/2}{\varepsilon_{i,j,k} + \sigma_{i,j,k}^{*} \Delta t/2} - \frac{\Delta t}{\varepsilon_{i,j,k} + \sigma_{i,j,k}^{*} \Delta t/2} \tilde{\delta}_r \vec{H}_{i,j,k}^{n+0.5} \tag{3.5}$$

After each calculation software checks the difference in the magnetic and electromagnetic field components of last and previous iterations. If the difference between two consecutive calculations is equal or less than pre-defined termination condition of simulation, it assumes steady-state condition is reached and stops the program. Also in the Lumerical user can define the end time of the simulation. If the simulation is not reached steady-state until defined time, software stops the calculations at the pre-defined time. Since the technique is time domain it allows wide spectrum simulations in a single run. It is an advantage for our study since we do not know the exact resonant point of the structure and we can find the resonant point in one simulation by exciting the structure with a broadband source. Most important disadvantage of the technique is all the simulation space should be gridded. Therefore, simulation of a small structures in a big system takes too much simulation time.

We use gold as antenna material and calculate the response of the structure under excitation of plane wave. Gaussian beam acts as plane wave on gold nanoantenna surface due to small size of the beam compared with real beam size. Therefore, in simulations we used plane wave approximation. We excite the antenna structure, light with monochromatic 1500 nm and 1550 nm wavelength for linear simulations, but for the nonlinear simulations we use 150 fs pulse length at the same wavelengths. As required in all simulations, transverse electric (TE) polarization is selected to activate plasma oscillations. Nonlinear index of refraction, n_2, for As_2Se_3 ranges between 1.1x10^{-17} m^2/W and 2.3x10^{-17} m^2/W [43, 44, 45]. For our simulations, we use optical properties of As_2Se_3 as n_0=2.78, n_2=1.6x10^{-17} m^2/W and As_2S_3 as n_0=2.45, n_2=5.5x10^{-18} m^2/W. In Lumerical software one can create Kerr nonlinear material by defining its χ^3 and permittivity (ε) values. To determine these values we use Equation 2.13 which shows the relation between n_2 and χ^3. For all the simulations we select the boundary conditions as perfectly matched layer (PML) to get rid of reflections from boundaries. However, since the structure is symmetric for both x and y

directions, we define one of x axis boundaries as anti-symmetric and one of y axis boundaries as symmetric according to polarization of light source. Therefore, we reduce necessary time for each simulation significantly by reducing effective simulation volume one forth of real volume. In the simulations we insert extra mesh around the gold nanoantenna structure to have more precise results. The extra mesh has 1 nm grid size for all three directions. We essentially simulate two different antenna types in the simulations. One of them is stripe antenna which has a square or rectangular cross section, and the other one is rod shaped antenna which has a circular cross section. We then examine different properties of these antenna structures such as the effect of height for stripe antennas and the effect of diameter for rod shaped antennas. Additionally, we investigate all types of antennas for the resonant length of the antenna-substrate structures for simulated wavelength.

3.1 Stripe Nanoantennas

In this section, we investigate the resonant length of stripe antennas and nonlinear novel freqeuncy generation at the near field of these nanoantennas. Fundamental configuration for stripe nanoantennas consists of two main parts: gold resonant nanoantenna rests on highly nonlinear chalcogenide glass (Fig. 3.2). Also, we simulate the structure with an additional layer between the antenna and the substrate as adhesion and wetting layers. For all calculations the antenna width and height is fixed and 50 nm. We monitor electric field at the interface between antenna and chalcogenide substrate by inserting 2D field monitor. We select the maximum enhancement value as a figure of merit for antenna to determine its resonant length. Therefore, for each simulation we probed the intensity amplification value from a point which is around to corner of the antenna by normalizing calculated electric field intensity with respect to intensity of source.

For harnessing the enhancement feature of preferred stripe nanoantenna due to its simple and easy producible geometry, we need to first determine its resonant lengths for wavelength of 1500 nm by performing simulations for several

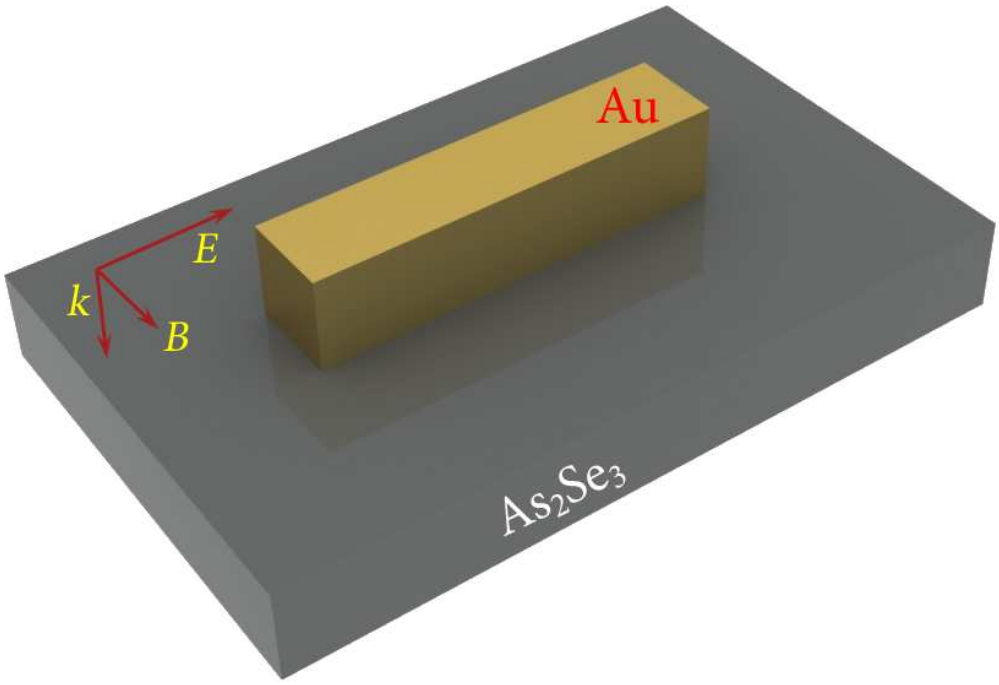

Figure 3.2: Schematic illustration of the simulated structure. Gold nanoantenna placed on highly nonlinear (n_2=1.6x10^{-17} m^2/W) As_2Se_3 glass substrate.

data points (Fig. 3.3). We perform simulations between 80 nm and 1050 nm with 10 nm step size, but at the peak points we prefer smaller step size to have more precise results. First and second resonances of the structure are at 190 nm and 680 nm antenna lengths respectively, and these values correspond to $\lambda_{eff}/2$ and $3\lambda_{eff}/2$. The field distributions for these two resonance points are given in Figure 3.4, and it is a bare fact that intensity is highly confined around the corners of the antenna. Localization of incoming electromagnetic waves around the sharp corners of the antenna is consistent with previous works about the field [3, 2, 18]. Maximum enhancement value in the first resonance mode is greater than the second resonance mode. For the first resonant mode, also known as the fundamental mode, light only concentrated around the short edges of the antenna. On the other hand, for the second resonance mode there are some spots around the long edge of the antenna. This causes wider distribution for incoming light and so peak intensity enhancement for this mode is less than the first one. At the

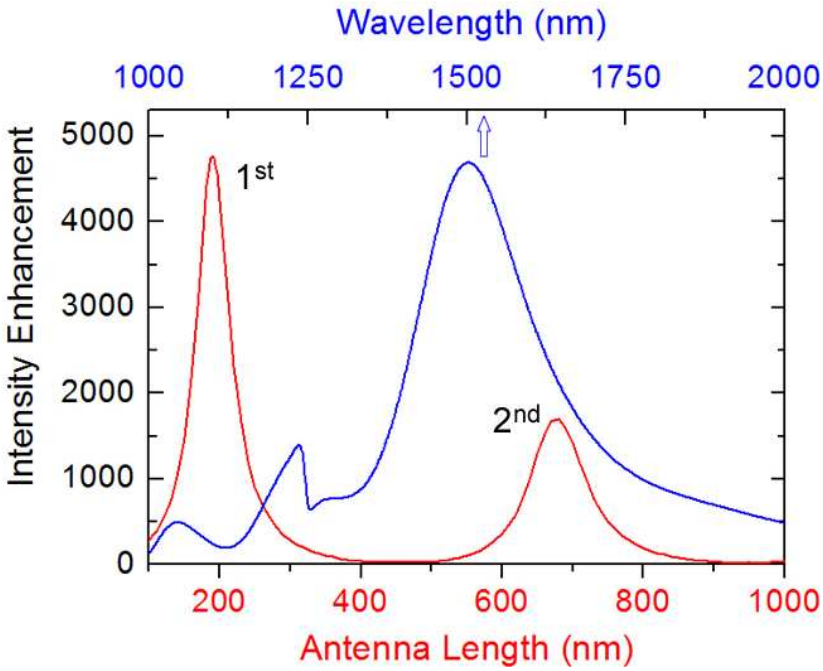

Figure 3.3: Plot of maximum enhancement due to metallic structure as a function of antenna length. The peaks are at 190 nm and 680 nm correspond to $\lambda_{eff}/2$ and $3\lambda_{eff}/2$, where wavelength of incident light is 1500 nm. Maximum enhancement is greater than three orders of magnitude.

first resonance peak, achieved maximum enhancement is about 5000. Through the study for non-linear simulations of stripe antenna on As_2Se_3 substrate, we performed simulations at this antenna length to maintain maximum enhancement for 1500 nm wavelength.

To explore enhancement capability of 190 nm resonant nanoantenna for wavelengths other than 1500 nm, we also carried out simulations by ignoring nonlinearities. We plot Figure 3.3 response of nanoantenna in the spectrum range of 1000-2000 nm, and we recognized that enhancement exist not only at single resonant wavelength but it also gradually decreases around the both sides of it. This is important because the created frequencies can be amplified by an enhancement factor of antenna at these wavelengths. Therefore it makes direct use of generated frequencies in the applications possible. This feature also makes nanoantenna-nonlinear media system convenient to use as on chip supercontinuum source. The

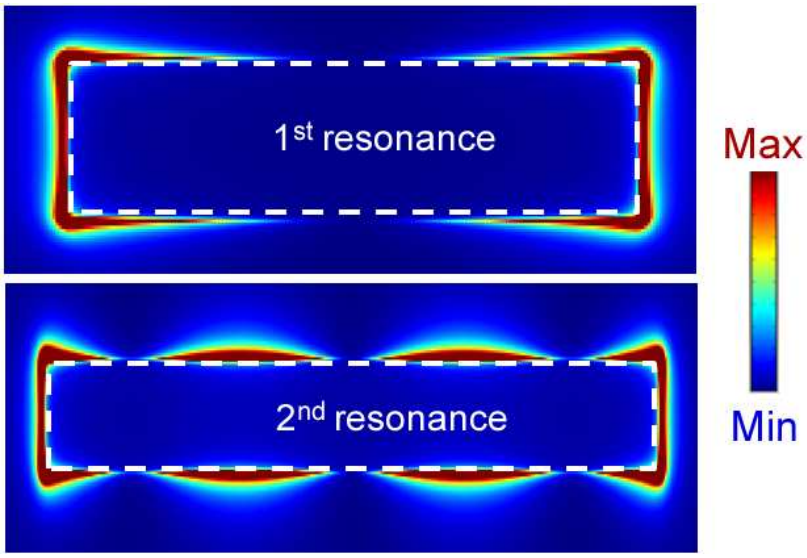

Figure 3.4: Electric field distribution of first and second resonant modes at two different resonant antenna lengths. Electric field localized around the sharp corners of the nanoantenna.

peak located near 1250 nm is due to quadrupole resonance. This resonance occurs when the size of the antenna is large for dipole peak. However, this peak is always smaller than the dipole resonance peak, so we do not observe anything about this peak in the maximum enhancement value plot. Kelly *et al.* observes quadrupole peak at spherical particles [18], and in our study we observe it for rectangular nanoantennas.

Since we fabricate the nanoantennas in array configuration by using e- beam lithography we look the resonant antenna length of the antennas in array configuration. We put 500 nm gap in x axis and 1000 nm gap in y axis between two consecutive antennas. This configuration is the same with which we fabricate by using e-beam lithography technique. The only difference between simulation and fabrication is, in fabrication we put the array in a square which has 50 μm edge length, but in the simulation we assume that array goes to infinite. Since 50 μm is too greater than an antenna length this assumption will not cause any error in our computation, but it makes the computation time and requirements less. In the results of simulation we saw that resonant antenna length of array

configuration is not different than single antenna. Since the gaps between the antennas are big enough there is not any interaction between antennas and they behave like an individual antenna.

In order to analyze nonlinear response of dielectric structure we looked to its spectral behaviour at the antenna-substrate interface while exciting resonant structure with the fixed peak intensity of 4.8 $W/\mu m^2$. We get data from a long edge of the antenna with equal distance between the data points and gather them to obtain a 2D map of nonlinear phenomena occurring in resonant nanostructures (Fig. 3.5). It is easily observable from the Figure 3.5 that there is both continuum and third harmonic generation around the corners of the antenna. This graph is also consistent with Figure 3.4 about the maximum enhancement point. Full width half maximum (FWHM) of continuum generation is around 500 nm for mentioned peak intensity. This broadening is almost same with fiber counterparts [14] in this excitation intensity. Third harmonic generation is at $\lambda/3$, where λ is incident light wavelength. For comparison purposes we inject the light with same features (pulse length, power) on a bare As_2Se_3 glass. However, we cannot observe any spectral broadening. This verifies the fact that employed nanoantenna reduces threshold intensity for generation of light with novel spectral components.

In Figure 3.6, we investigate effects of the peak intensity of incident light on the nonlinear response of the chalcogenide glass. Here, spectra is calculated at a point close to corner of the antenna, where maximum enhancement happens, for different incident light intensity. From the plot, we can see that there is not any continuum generation until intensity reaches 3.3 $W/\mu m^2$. This can be considered as the threshold point of continuum generation. After this point, increment in power broadens FWHM of both continuum and harmonic generation. This shows that more input intensity allows more broadening in output spectrum.

To compare widely used SiO_2 susbtrate and As_2Se_3 substrate we find the resonant length of nanoantenna on SiO_2 substrate by several simulations (Fig. 3.7). We sweep antenna length from 100 nm to 800 nm with 10 nm step size. According to simulation results, resonant length of nanoantenna on SiO_2 substrate is

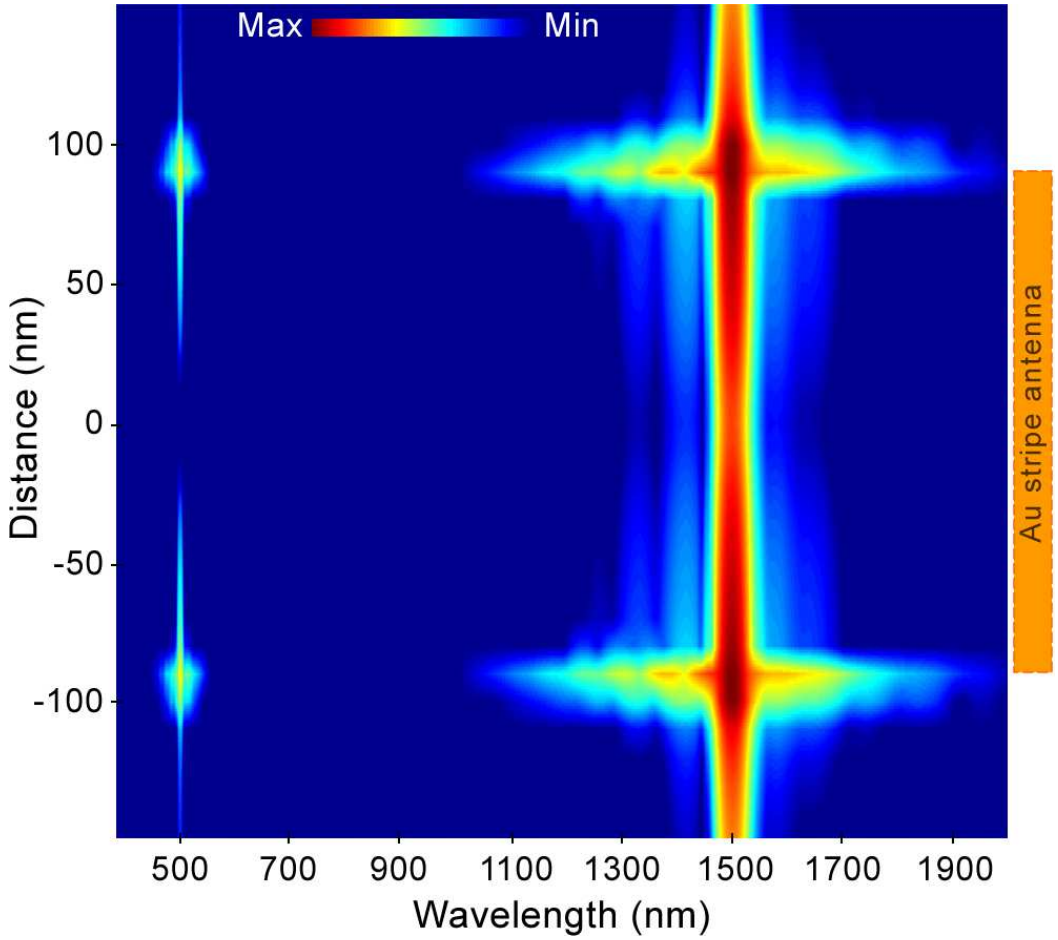

Figure 3.5: Two dimensional map of intensity as a function of wavelength and distance to the center of the antenna. Incident light intensity and pulse length (FWHM) used in FDTD simulation are 4.8 W/μm^2 and 150 fs respectively. Spectral broadening and third harmonic generation occur at the corners of the antenna. Achieved continuum generation is more than 500 nm around the excitation wavelength of 1500 nm. Third harmonic generation observed at the 3ω incident which corresponds to 500 nm wavelength. As the intensity increases going from center to the edges of the gold antenna, generated light both at the third harmonic of incident light and around pump wavelength also broaden.

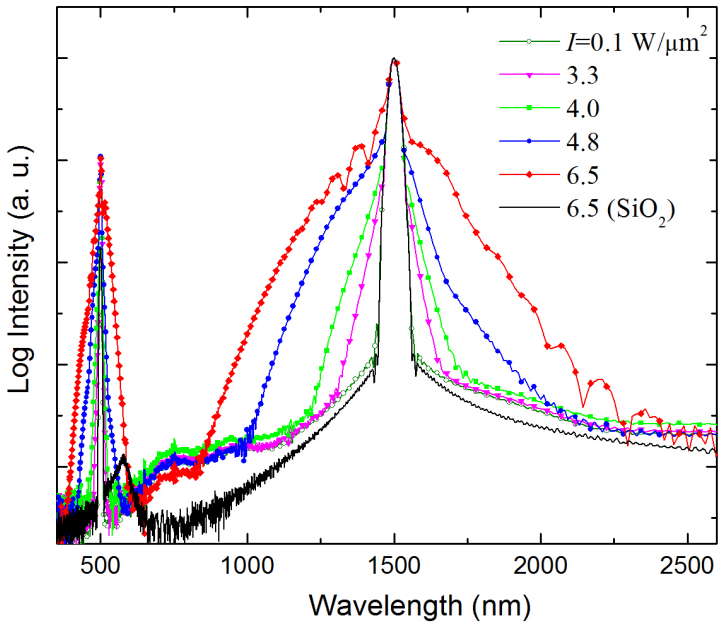

Figure 3.6: Normalized logarithmic intensity plotted as a function of wavelength to observe effects of pump intensity. Spectral broadening and harmonic generation of incident light investigated for different excitation powers. Threshold intensity value for triggering spectral broadening is about 3.0 W/μm^2. As the incident light intensity increases spectral broadening also increases, both around the incident wavelength and third harmonic generation. Comparing with chalcogenide, silica glass as a nonlinear medium remains insufficient for broadening even if intensity value is 1000 times higher than that of threshold value of arsenic selenide.

at 350 nm. This value also corresponds to $\lambda_{eff}/2$. If we compare the resonant length of nanoantennas on SiO_2 and As_2Se_3 substrates, we show that resonant length on As_2Se_3 substrate is smaller. Since refractive index of As_2Se_3 is greater than refractive index of SiO_2 at incident wavelength, λ_{eff} for As_2Se_3 is smaller. As a result we can say that resonant length of antenna is inversely proportional with refractive index of substrate material. This result is consistent with the previous work on effect of dielectric substrate on resonance of triangular metal particles [18]. Moreover, maximum intensity enhancement on SiO_2 substrate is about 7000 and this is greater than maximum enhancement value on As_2Se_3 substrate. We can say that nanoantennas can localize incoming electromagnetic wave

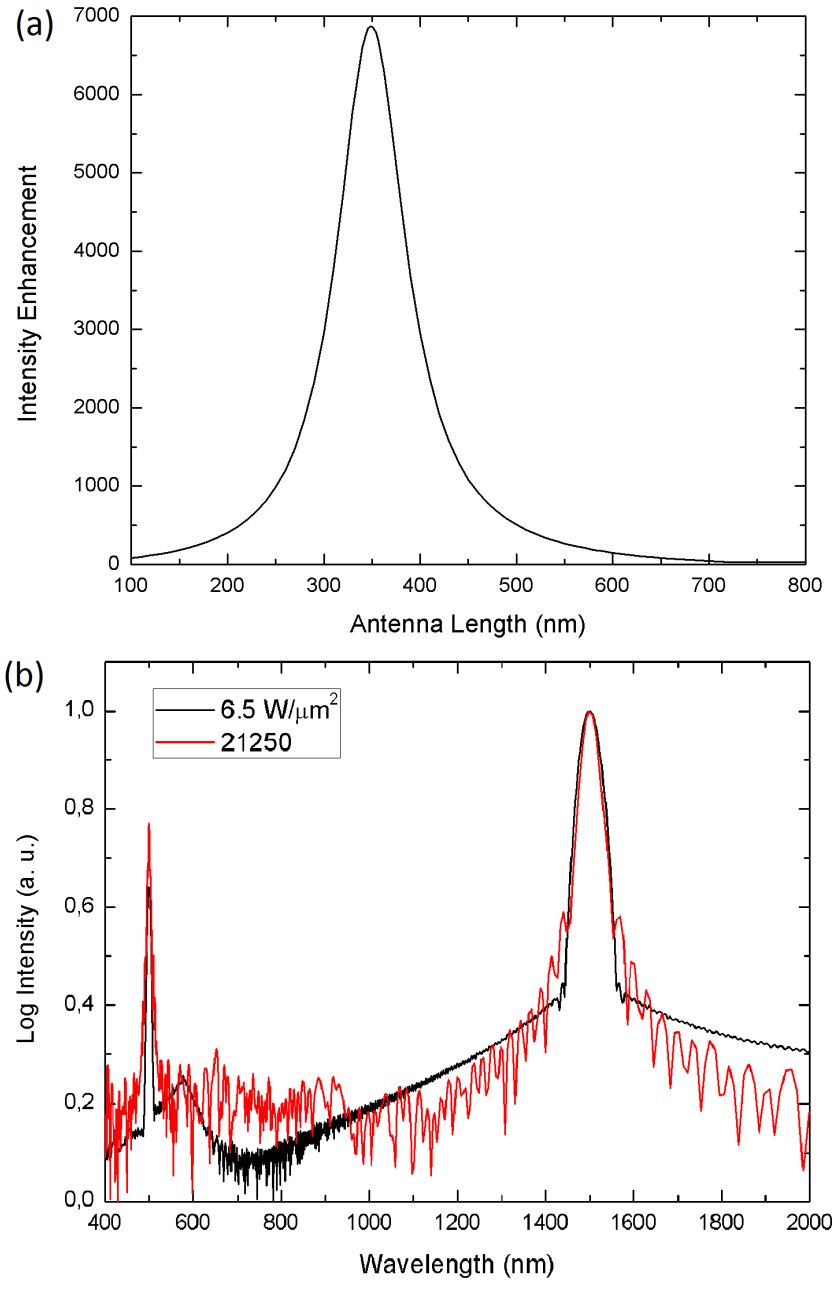

Figure 3.7: (a) Plot of maximum enhancement due to metallic structure as a function of antenna length. (b) Normalized logarithmic intensity as a function of wavelength for SiO_2 substrate for two different input intensities.

more efficiently on low refractive index substrates.

We also simulate nonlinear response of SiO_2 substrate by employing resonant nanoantenna on the substrate. We shine a light with 6.5 W/μm^2 intensity and 150 fs pulse length. For this intensity spectral broadening around the incoming light's wavelength does not exist. We increase the intensity of light to find the threshold value to trigger spectral broadening. Continuum generation starts at about 3300 times higher power than As_2Se_3 case (Fig. 3.7). Nonlinear refractive index of SiO_2 is about 3600 times lower than n_2 of As_2Se_3. Since the enhancement by the plasmonic antenna on SiO_2 is greater, threshold intensity difference for triggering nonlinear generations is less than the difference between nonlinear refractive indices of materials. Although, enhancement value of nanoantenna on SiO_2 substrate is greater, threshold power for continuum generation is greater than the previous one. This shows that only the high localization property of plasmonic antennas is not enough for low threshold continuum generation, but high nonlinear refractive index substrate is necessary for this work. Higher nonlinear and linear index of arsenic selenide material lowers the threshold of nonlinear processes and increases electromagnetic storing capability respectively.

We also explore enhancement at deeper points in As_2Se_3 substrate. We obtain data with approximately 5 nm steps from surface to 100 nm depth. In deeper points of substrate, enhancement decreases dramatically (Fig. 3.8). At the interface between antenna and substrate, enhancement is about 5000. However, at 100 nm depth, power could not be confined by resonant behavior of the nanoantenna. This shows the high confinement capability of nanoantennas at their near-field. Therefore, plasmonic antennas efficiently localize propagating electromagnetic waves to sub-wavelength spots.

We also investigate nonlinear generation for different intensification values. For maximum enhancement, spectral broadening is easily observable and FWHM of the continuum generation is narrowing while enhancement is decreasing. Moreover, intensity of third harmonic and spectral broadening around the $\lambda/3$ also reduces following a decrease in enhancement. For 10 times enhancement there is not any significant spectral broadening around the incident wavelength and

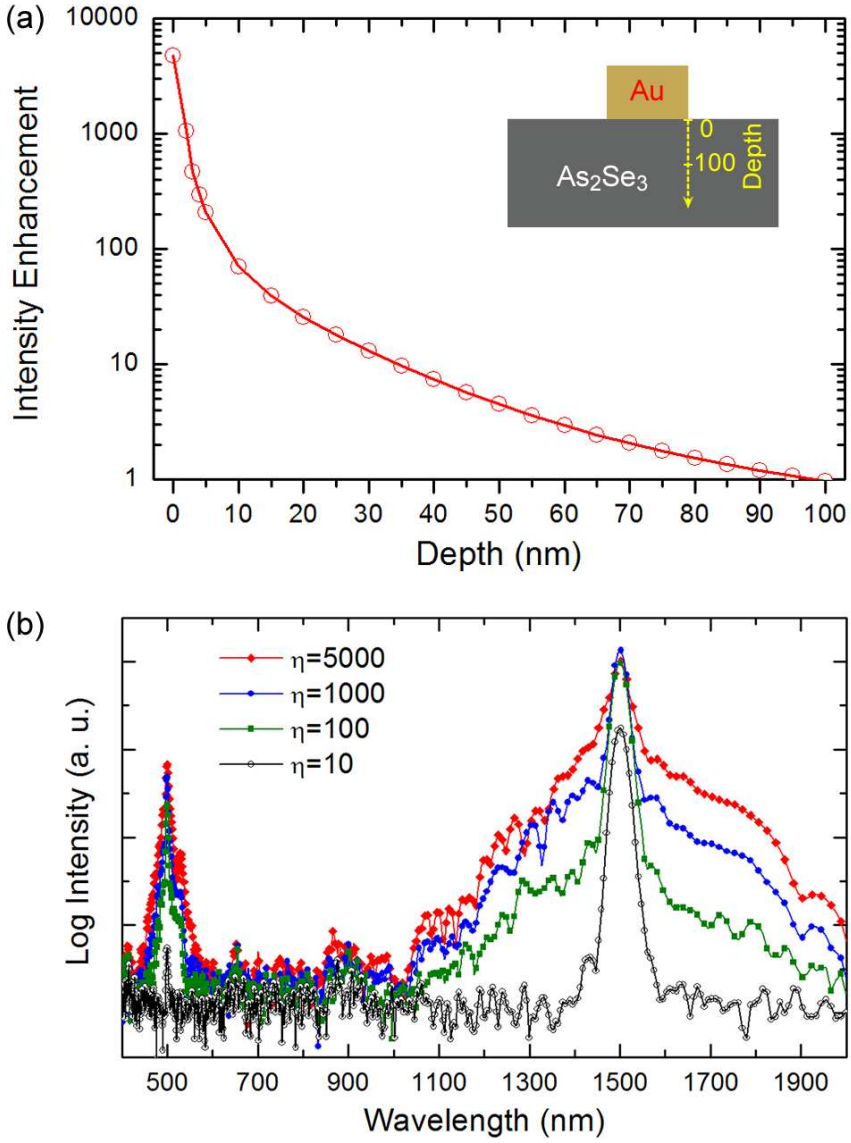

Figure 3.8: (a) Maximum enhancement as a function of depth. (Inset is cross section of the structure.) In the deeper point of nonlinear medium electric field enhancement reduces dramatically and there is only one order of magnitude enhancement at 30 nm depth. Beyond 100 nm depth there is no more enhancement. (b) Plot of spectrum of generated light at the edges of the nanoantenna, for different enhancement values which corresponds to different depth points. As the enhancement reduces spectral broadening also decreases. Both continuum and third harmonic generations are not yet observable for one order of magnitude enhancement.

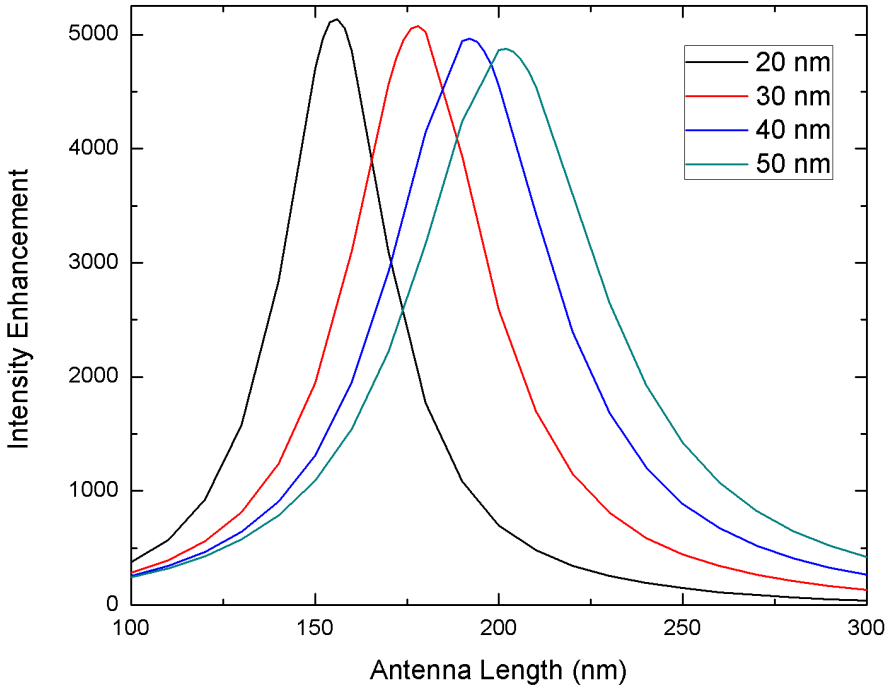

Figure 3.9: Plot of maximum enhancement as a function of antenna length for As_2Se_3 substrate at 1550 nm for different antenna height.

third harmonic generation is too weak. This implies that without efficient sub-wavelength localization property of nanoantennas only highly nonlinear substrate is not sufficient to initiate low threshold continuum and third harmonic generation.

We compare resonant length and maximum enhancement values for different heights of nanoantenna on As_2Se_3 substrate (Fig. 3.9). We compare heights 20 to 50 nm with 10 nm step size. We do not simulate height under 20 nm because fabrication of these heights is not feasible by thermal evaporation technique, which we use for fabrication of nanoantennas due to material properties of gold. We simulate all the antennas between 100 nm and 300 nm length with 10 nm step size to find fundamental resonant mode of the antennas. Finding fundamental

mode is enough for our purpose because we know from our previous simulations (Fig. 3.3) that fundamental mode generates maximum enhancement values. We select 1550 nm monochromatic source, and we monitor the electromagnetic field at antenna substrate surface. Maximum enhancement values are at 156, 178, 192 and 202 for 20, 30, 40 and 50 nm height nanoantennas respectively. Maximum enhancement value is also greater than 5000 for 20 nm height. We observe that increases in height causes increases in resonant antenna length. This is consistent with the work of Kelly *et al.*, where they claim that resonant length red shifts with the increase in volume of metal nanoparticle [18]. Furthermore, thinner antennas localize incoming electromagnetic wave slightly more efficiently than thicker ones. Since localization of light enhances by the decrease of height of nanoantenna, effective refractive index on light increases; therefore λ_{eff} decreases according to Equation 3.6 and resonant length of the nanoantenna decreases proportionally.

$$\lambda = \frac{\lambda_0}{n} \tag{3.6}$$

Moreover we compare the response of nanoantennas at same height for different input wavelength by checking Figure 3.3 and Figure 3.9. We observe that resonant length of the nanoantenna increases by the increase of wavelength of shined light. Therefore, λ_{eff} is proportionally smaller at 1500 nm and resonant length of antenna is smaller. Also, we realize that confinement efficiency of resonant antenna at 1550 nm is slightly better than the other one. According to these results we can say that wavelength of light source and localization efficiency of nanoantenna also affects the resonant length of the antenna.

During the fabrication we sometimes encounter the problem of removal of gold antennas from As_2Se_3 substrate at the end of the lift-off of electron beam resist step. To have better fabrication performance, our proposal is to deposit adhesion and wetting layers between gold and As_2Se_3 thin film. We simulate 1 nm Cr and 1 nm Ti to be deposited as an adhesion layer and 1 nm Ge to be deposited as a wetting layer between them. For the simulations we insert 1 nm layer between gold and As_2Se_3 and find resonant length of the antenna at this configuration for each material at 1550 nm wavelength. We monitor the electromagnetic field profile at interface between adhesion or wetting layer and As_2Se_3 substrate since

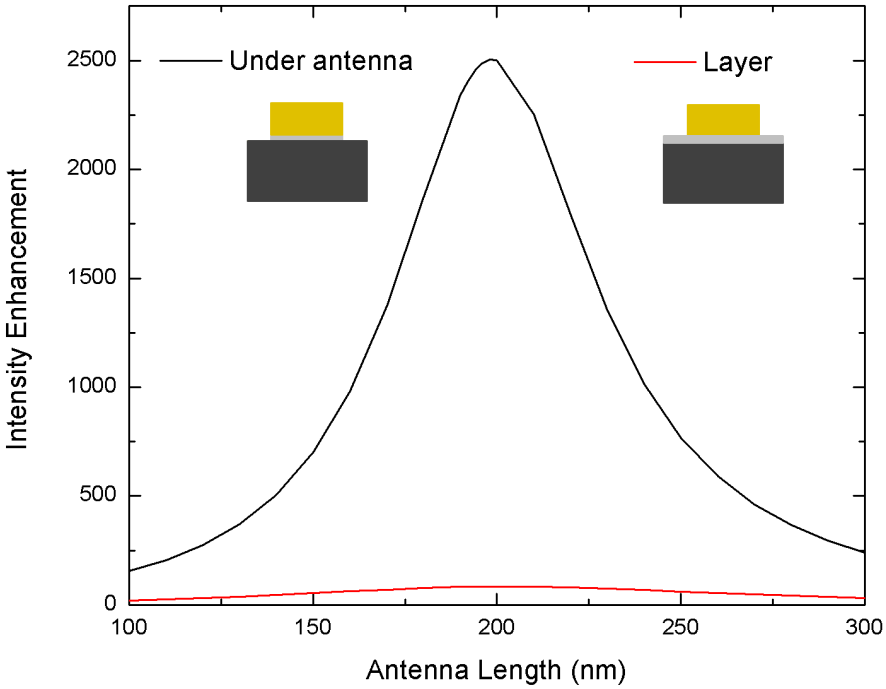

Figure 3.10: Plot of maximum enhancement as a function of antenna length for As_2Se_3 substrate at 1550 nm in case of 1 nm Cr deposited as an adhesion layer between gold and substrate.

we want to maximize localized electromagnetic field on highly nonlinear glass. For all samples we sweep the antenna length between 100 nm and 300 nm with 10 nm step size.

Figure 3.10 shows the resonant length of the antenna structure in the case of 1 nm Cr deposited as adhesion layer just under the gold antenna. We also simulate if we coat all the As_2Se_3 surface with 1 nm Cr layer. In that case we observe that this layer kills almost all the plasmonic enhancement effects (Fig. 3.10). Since Cr is metal and plasmonic effects are observable between metal dielectric interface, the Cr layer does not allow interaction between Au and As_2Se_3 if it is coated along the whole surface. However, if we coat Cr just under the Au antenna it

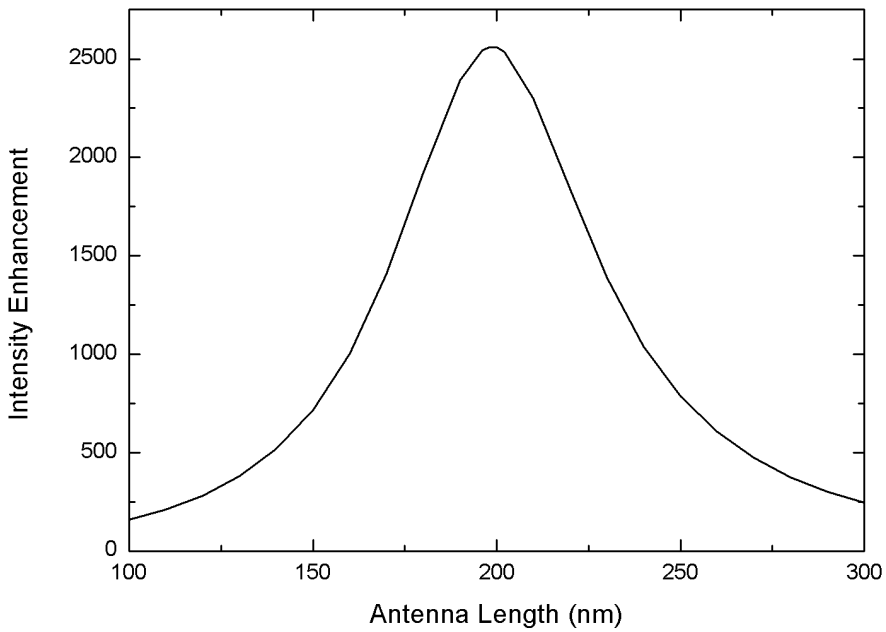

Figure 3.11: Plot of maximum enhancement as a function of antenna length for As_2Se_3 substrate at 1550 nm in case of 1 nm Ti deposited as adhesion layer.

also causes a decrease in enhancement, but still it is greater than three order of magnitude enhancement. Maximum enhancement is close to 2500 and resonant length is at 198 nm in that case. It is enough to observe low threshold nonlinear generation (Fig. 3.8).

We also simulate a 1 nm Ti coated structure as an adhesion layer to define resonant antenna length and intensity enhancement values and plot Figure 3.11. We observe that Ti also decreases the plasmonic intensity enhancement property of gold antennas, and the resonant length of the structure is the same as in the Cr coated case, 198 nm. Furthermore, at that antenna length intensity enhancement is almost the same as the Cr coated case, and it is around 2500. According to simulation results using adhesion layer significantly decreases plasmonic effects,

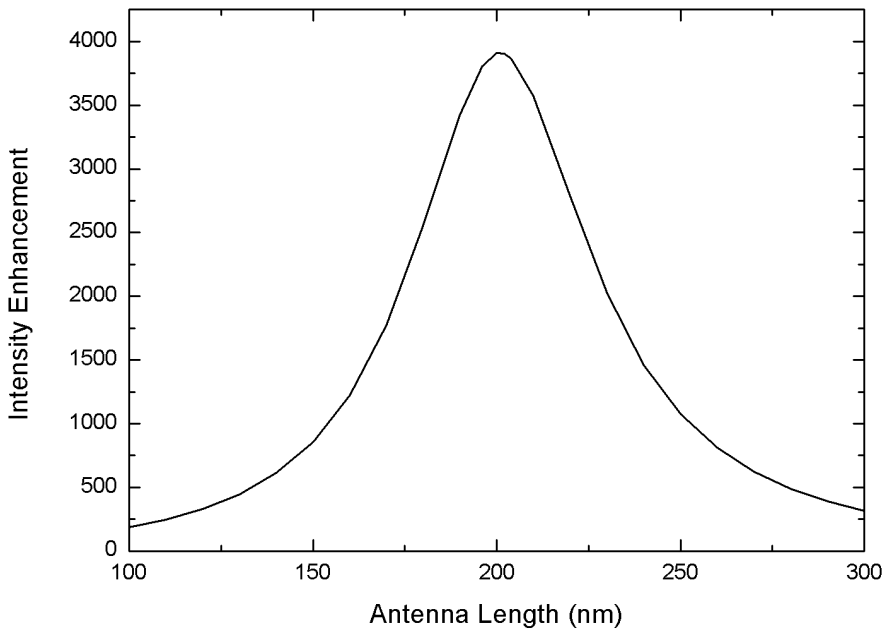

Figure 3.12: Plot of maximum enhancement as a function of antenna length for As_2Se_3 substrate at 1550 nm in case of 1 nm Ge deposited as adhesion layer.

but it does not affect too much on resonant length of antenna. Moreover, deposition of Cr or Ti as an adhesion layer does not make a significant difference in our structure; therefore one of these materials can be deposited according to availability or price.

We simulate the resonant length of gold nanoantenna and maximum intensity enhancement values on As_2Se_3 substrate if we insert Ge as a wetting layer between the antenna and the substrate (Fig. 3.12). A wetting layer is an initial layer which allows better grown and sticking of new layer on the substrate surface. We prefer Ge because it is a known and good wetting layer for gold. Simulation results for Ge deposited antenna structure have better intensity enhancement values than Cr and Ti coated cases, while on the other hand it is less than the case without any additional layer. The peak of the plot is close to 4000 and the resonant length

of the antenna is 200. One possible reason for having a better enhancement value for Ge is that Ge is a semiconductor. Cr and Ti are metal and they significantly reduce the plasmonic effects, but since Ge is semiconductor it has better results. According to maximum enhancement values one should select the Ge as an additional layer between gold antenna and As_2Se_3 substrate to overcome gold's sticking problem because of its better performance when compared to Cr and Ti.

We use another calcogenide glass As_2S_3 as a highly nonlinear substrate instead of As_2Se_3. They have different linear and nonlinear refractive indices. We sweep the antenna length from 100 nm to 300 nm with 10 nm step size to find resonant length of the gold nanoantenna on As_2S_3 glass at 1550 nm incident light wavelength (Fig. 3.13). The peak point of the plot is at 230 nm antenna length and the maximum intensity enhancement is more than 4500. Since refractive index n_0 of As_2S_3 is smaller than As_2Se_3, resonant length of gold antenna on As_2S_3 substrate is longer than on the As_2Se_3 substrate but shorter than SiO_2 substrate (Fig. 3.7). This also shows the effect of linear refractive index of material, n_0, on resonant length of antenna. Maximum intensity enhancements are almost same.

We simulate nonlinear response of gold nanoantenna on As_2S_3 substrate for 1550 nm excitation wavelength 150 fs pulse length and 6.5 W/μm^2 intensity and plot the spectrum between 200 nm and 2000 nm by probing the point where maximum enhancement occurs (Fig. 3.13). Spectral broadening is narrower when compared to As_2Se_3 because As_2S_3 has a lower nonlinear refractive index n_2. We observe 200 nm FWHM spectral broadening for excitation with 6.5 W/μm^2 intensity. This is consistent with our previous results about the effects of nonlinear refractive index n_2 on continuum generation. We also observe 3$^{\text{rd}}$ and higher harmonics generation. Harmonic generations are observable at smaller intensity values for both As_2S_3 and As_2Se_3. Intensity of harmonics decreases gradually while going to higher harmonics. The 3$^{\text{rd}}$ harmonic is generated at around 516 nm wavelength which corresponds to $\lambda/3$, and other harmonics are generated at $\lambda/5$ and $\lambda/7$.

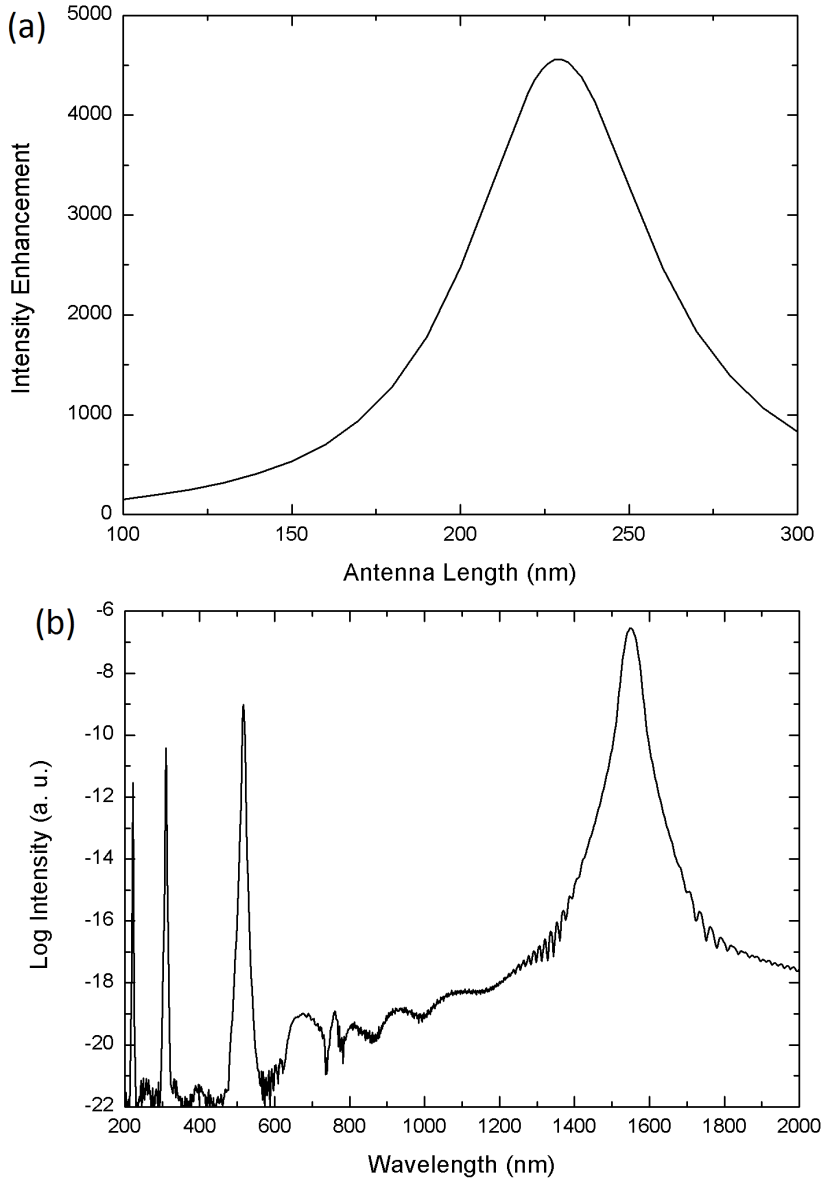

Figure 3.13: (a) Plot of maximum enhancement as a function of antenna length for As_2S_3 substrate at 1550 nm. (b) Plot of spectrum of generated light at the edges of the nanoantenna on As_2S_3 substrate for 1550 nm excitation wavelength.

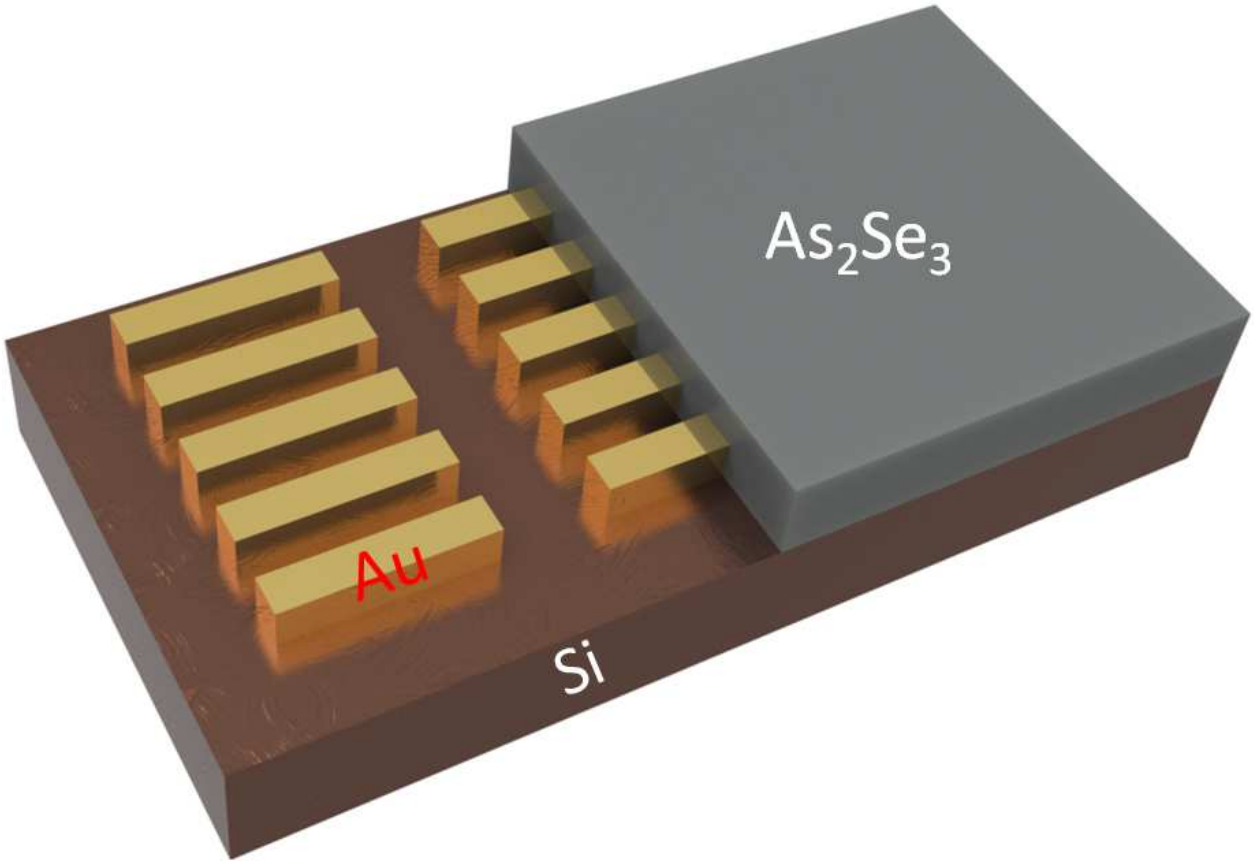

Figure 3.14: Schematic illustration of the simulated structure. Gold nanoantenna sandwiched between highly nonlinear (n_2=1.6x10^{-17} m^2/W) As_2Se_3 and SiO_2 glass substrate.

We design another nanoantenna-nonlinear glass configuration because of challenges in the fabrication process of gold nanoantennas on As_2Se_3 substrate. In this new configuration gold nanoantennas are sandwiched between Si and As_2Se_3 thin film (Fig. 3.16). Fabrication of this configuration will be explained in detailed in the fabrication chapter. To simulate, we place 50 nm gold antenna on Si substrate and locate 100 nm As_2Se_3 film on top and around the antenna. We excite the structure with 1550 nm monochromatic source from top of the structure to determine the resonant length of the antenna in this configuration. Resonant length of the antenna is 96 nm and maximum intensity enhancement is more than

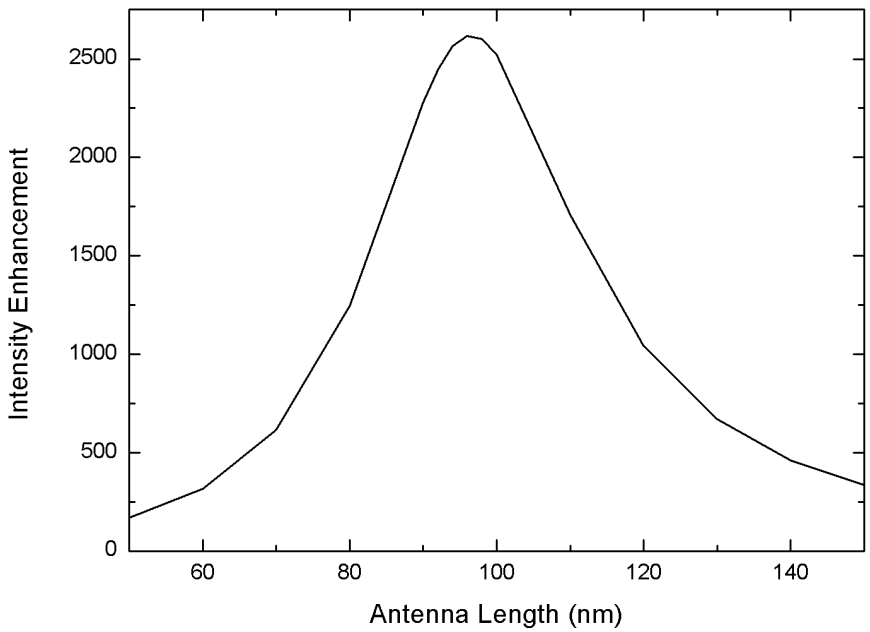

Figure 3.15: Plot of maximum enhancement as a function of antenna length for Au antennas sandwiched between As_2Se_3 and Si at 1550 nm excitation wavelength.

2500 (Fig. 3.15). Resonant length of the antenna is shorter than the first configuration since the effective refractive index is much greater in that case. In the first case the up side of the antenna is air; however in the second configuration all sides of the antenna are surrounded with high refractive index materials As_2Se_3 and Si. These results are parallel with results about the sphere metal particles in a dielectric medium in literature [18]. Maximum intensity enhancement on As_2Se_3 glass is about half of the first configuration. In that case there is also confinement on Si substrate which causes reduction on light localization on As_2Se_3 film.

After defining resonant length of the structure at 1550 nm excitation wavelength, we simulate the nonlinear response of the structure by shining 150 fs 6.5 W/μm^2 intensity light at the same frequency. We probe the electric field spectrum between 200 nm and 2000 nm at the near field of the structure. We

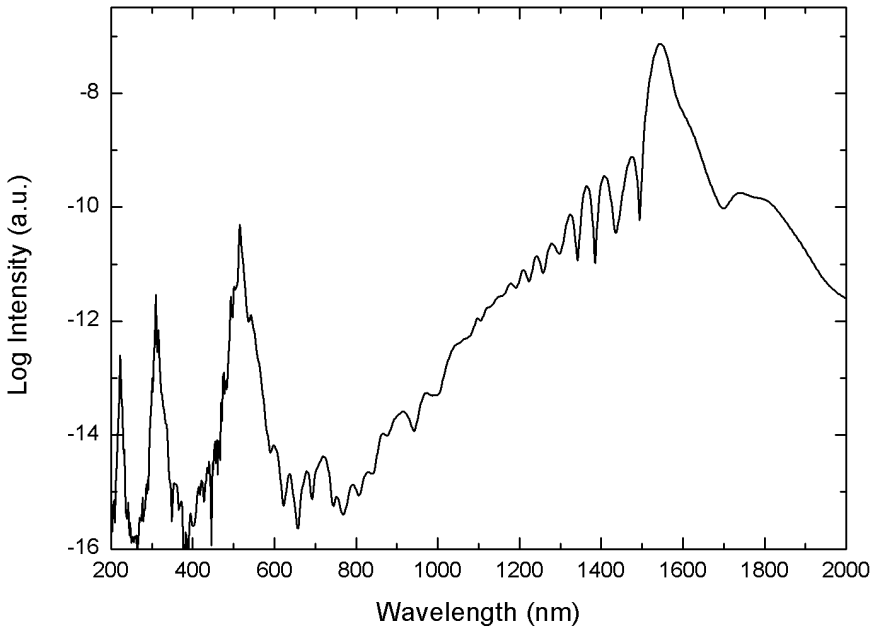

Figure 3.16: Plot of spectrum of generated light at the edges of the sandwiched nanoantenna between As_2Se_3 and Si.

observed both continuum generation and high harmonic generations including 3^{rd}, 5^{th} and 7^{th} harmonics (Fig. 3.16). Even maximum intensity enhancement in this configuration is less than the first configuration, and aspectral broadening in the nonlinear case is larger. Since almost all sides of antenna are surrounded with As_2Se_3 glass, more light-material interactions occur and nonlinear effects and generations are more prominent. Intensity of high harmonic components decreases gradually and it is similar to the first configuration.

For the second nanoantenna design we also simulate the structure by using As_2S_3 glass as nonlinear material. We sweep the antenna length from 50 nm to 200 nm and find the resonant length of the antenna. Maximum intensity enhancement occurs at 108 nm, and the peak value is more than 2500 (Fig. 3.17). The resonant length of the antenna is longer than in same configuration with

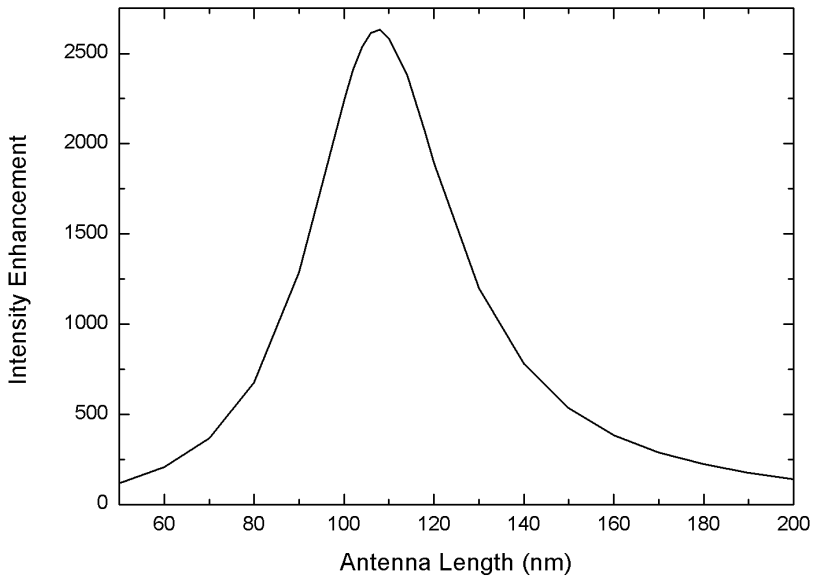

Figure 3.17: Plot of maximum enhancement as a function of antenna length for Au antennas sandwiched between As_2S_3 and Si at 1550nm excitation wavelength.

As_2Se_3 material and shorter than the first design with As_2S_3 material as expected when considering refractive indices of materials.

As a result, resonant length of antenna depends on wavelength of incident light, linear refractive index of substrate and surrounding dielectric and hight of the antenna. Resonant length of the antenna is proportional with the wavelength of the incident electromagnetic wave and height of the antenna. On the other hand, it is inversely proportional to the linear refractive index of both substrate and surrounding media. Moreover, results show that the strength of nonlinear generations is proportional to nonlinear refractive index of the substrate and the interaction of light and material. Using highly nonlinear materials and providing more interaction volume for light material interaction causes dominant nonlinear effects.

3.2 Rod Shaped Nanoantennas

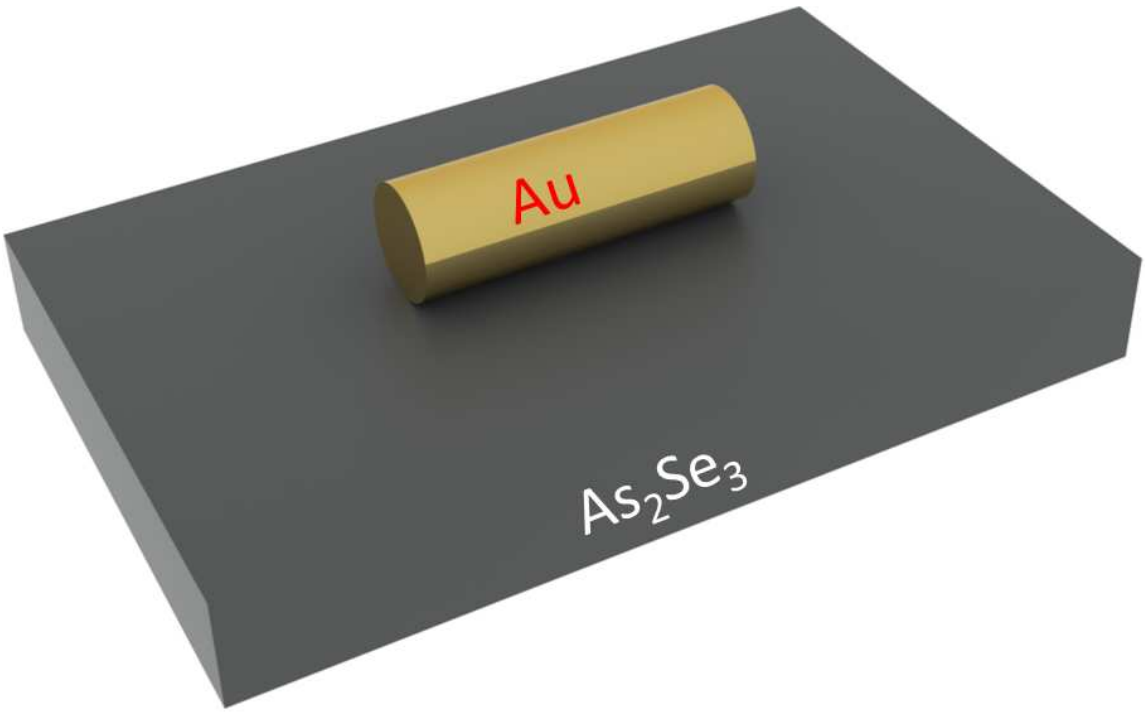

Figure 3.18: Schematic illustration of the simulated structure. Gold nanoantenna placed on highly nonlinear (n_2=1.6x10^{-17} m^2/W) As_2Se_3 glass substrate.

Other than square cross sectional nanoantennas, we also investigate near field optical wave localization properties of plasmonic antennas which have circular cross sections. We also examine the nonlinear response of structures which consist of single rod shaped nanoantenna and chalcogenide glass. Moreover, we simulate dipole antennas and study their resonant behaviour and nonlinear responses. For dipole antennas, we investigate the effect of gap distance and radius of antenna on resonant behaviour of the structure. For single antennas, we locate the antenna on As_2Se_3 glass substrate and monitor electric field distribution at the surface of chalcogenide glass, like in stripe nanoantennas, to determine the effects of the shape of the antenna on resonance length and strength (Fig. 3.18).

We sweep 50 nm to 200 nm with 10 nm step size to find the resonant length of the rod shaped gold nanoantenna on As_2Se_3 substrate. The diameter of the

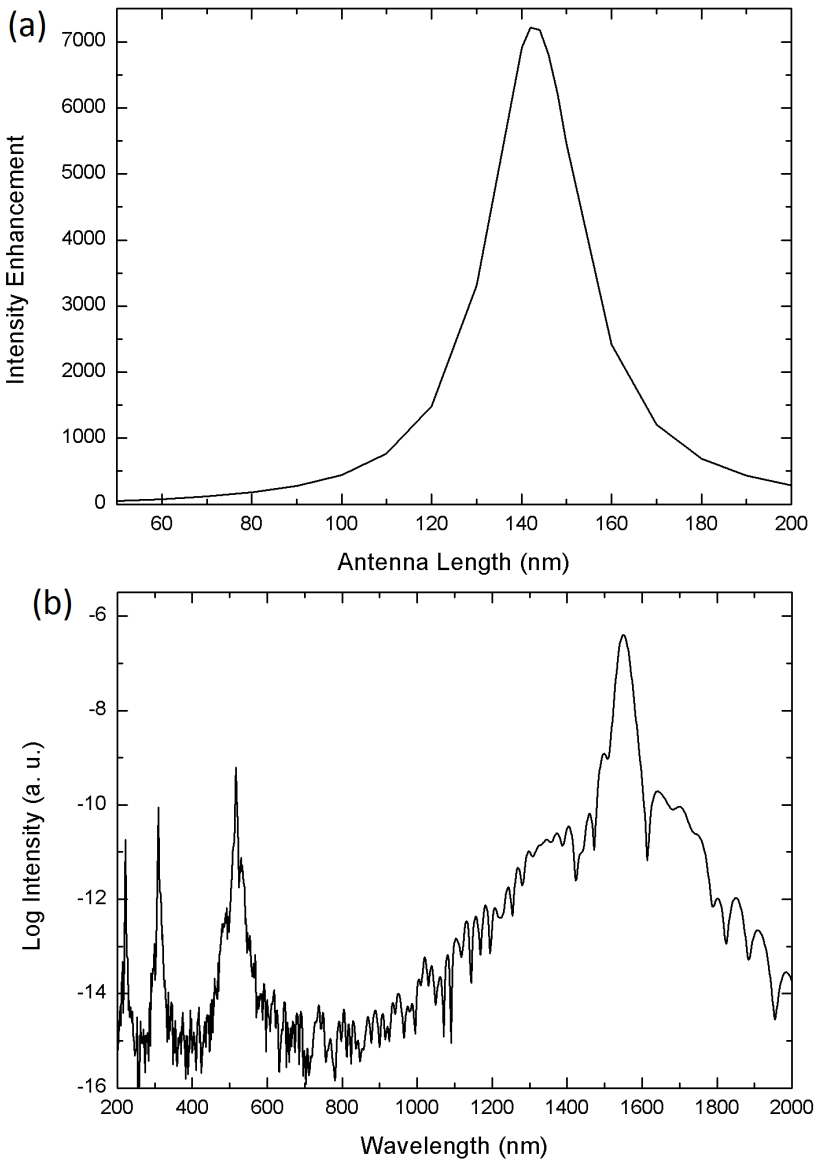

Figure 3.19: (a) Plot of maximum enhancement as a function of antenna length for 23 nm diameter Au rod antennas on As_2Se_3 substrate at 1550 nm excitation wavelength. (b) Plot of spectrum of generated light at the edges of the 23 nm diameter and 142 nm length nanoantenna on As_2Se_3 substrate for 1550 nm excitation wavelength.

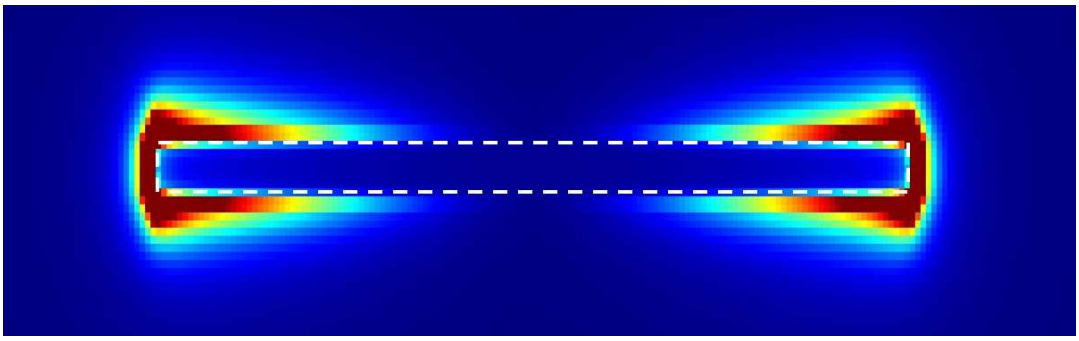

Figure 3.20: Electric field distribution of first resonant mode for rod shaped antenna.

rod is 23 nm because the diameter of the antennas which we fabricated by seed-mediated chemical technique is around 20 nm and 25 nm. The resonant length of the antenna is at 142 nm, and the maximum enhancement value is more than 7000 (Fig. 3.19). Also between 120 nm and 170 nm lengths rods provide 1000 times or more enhancement. Since the size distribution of antennas fabricated at this diameter by the seed-mediated chemical technique is wide the results are promising. Rod shaped antennas at 23 nm diameter provide better enhancement values than the stripe ones. Also the resonant length of rod shaped antennas is shorter than the stripe ones. Since the rod shaped antennas localize incoming light more efficiently, effective refractive index on light increases and resonant length of the antenna decreases. Electric field distribution at the surface of As_2Se_3 substrate is available in Figure 3.20. Electric field mostly localizes at two ends of the rod antenna at the fundamental mode similar to stripe nanoantennas for localizing light at short edge. In the stripe nanoantenna case, electric field mostly localizes around the corners of the antenna, but for the rod shaped antenna most enhancement occurs at the point where gold touches the substrate.

At the resonant length of antenna we excite the structure by 1550 nm 150 fs 6.5 $W/\mu m^2$ intensity plane wave source to simulate nonlinear response and nonlinear genereations. We probe the electric field at near field of the antenna in the range of 200 nm to 2000 nm by using field monitor. We observe both continuum generation and high harmonic generations (Fig. 3.19). FWHM of continuum

spectrum is more than 500 nm at mentioned input intensity, which is slightly greater than the stripe nanoantenna case. We expect this result because we use the same material as highly nonlinear material, and the intensity enhancement is slightly larger than the stripe case for rod shaped antennas. According to these results, more enhancement drives more spectral broadening for continuum generation. The difference for high harmonic components from the structure with stripe antenna is small.

To investigate the effect of diameter on resonant length and maximum intensity enhancement, we simulate a 70 nm diameter rod shaped antenna structure on As_2Se_3 substrate. Diameter of the antennas, which fabricated by using anodized aluminum oxide templates, are about 70 nm. Therefore, we choose this value for our simulation structure. We simulate the antenna length from 50 nm to 400 nm with 10 nm step size. Maximum intensity enhancement is about 4000, and it occurs at 258 nm antenna length (Fig. 3.21). 1000 or more intensity enhancement value observed for antenna length between approximately 200 nm and 325 nm. According to these results an increase in diameter of antenna causes significant decreases in maximum intensity enhancement values. The peak value for antenna with 70 nm diameter is almost half of the maximum point of 23 nm case. On the other hand the 70 nm diameter case provides broader antenna length band for 1000 or more enhancement than other one. Large diameter antennas have better performance for wide size distribution situations. Also, we compute the resonant wavelength of 80 nm length and 13 nm diameter gold nanoantennas on As_2Se_3 substrate by simulation. We select this size because we fabricate the gold nanoantennas with that size by using a different recipe for seed mediated chemical technique. In this simulation we fix the size of the antenna and sweep the wavelength of the incoming light from 800 nm to 1700 nm by 2 nm step size. According to the results maximum intensity enhancement is about 600 and it occurs around the 1530 nm wavelength (Fig. 3.22). Since the diameter of the antenna is small and meshing of the simulation is 1 nm, in that simulation circular geometry of the antenna is not perfectly generated by the software. Therefore, maximum enhancement value is lower than the other antennas, but it is still enough for nonlinear generation. We observe that resonant length of nanoantenna increases

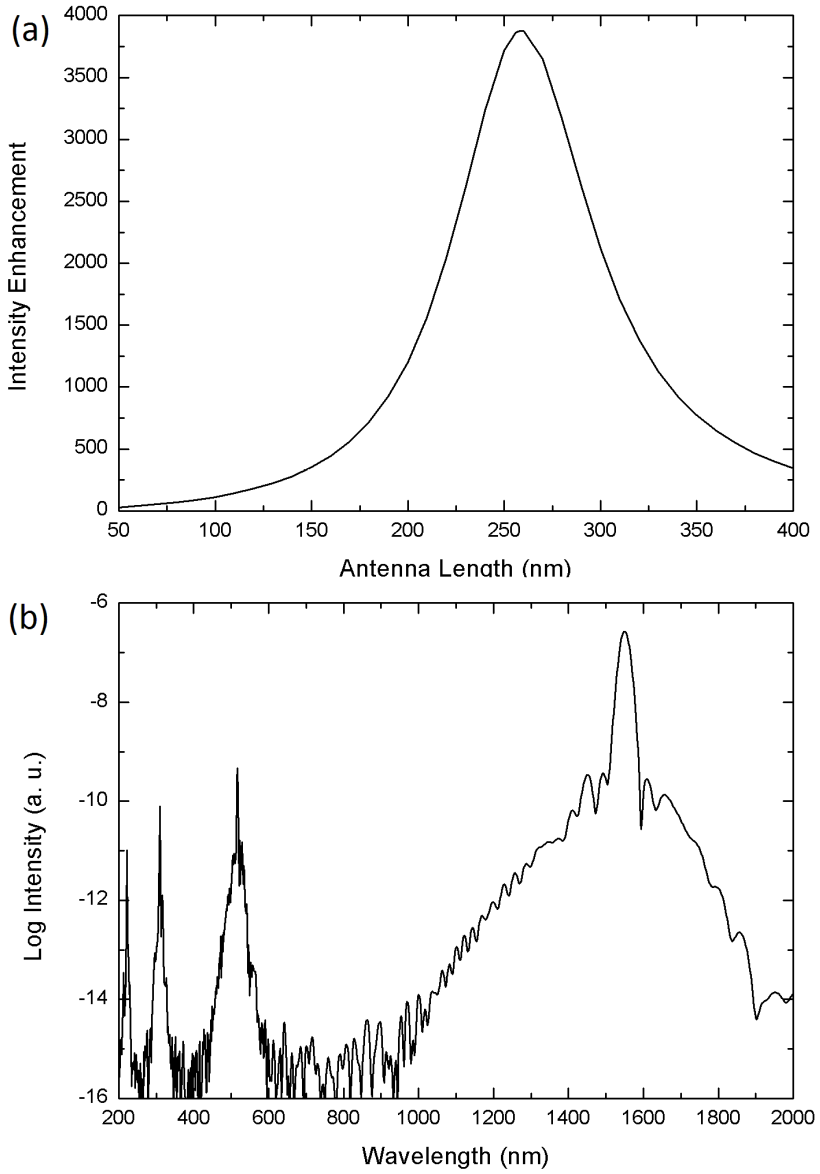

Figure 3.21: (a) Plot of maximum enhancement as a function of antenna length for 70 nm diameter Au rod antennas on As_2Se_3 substrate at 1550 nm excitation wavelength. (b) Plot of spectrum of generated light at the edges of the 70 nm diameter and 258 nm length nanoantenna on As_2Se_3 substrate for 1550 nm excitation wavelength.

with the increase of the diameter. A decrease in confinement of electromagnetic waves in high refractive index media causes larger λ_{eff}; therefore resonant length of antenna increases.

We simulate the nonlinear response of the structure by exciting it with 1550 nm 150 fs 6.5 W/μm^2 intensity plane wave source at 258 nm antenna length. Spectrum from 200 nm to 2000 nm is probed at the near field of the antenna. Output spectrum is similar to 23 nm diameter nanoantennas. There are also continuum and high harmonic generations at the output (Fig. 3.21).

Furthermore we simulate the rod shaped antennas on As_2S_3 glass. We sweep antenna lengths from 50 nm to 200 nm with 10 nm step size to determine the resonant length of antenna on the glass substrate. The diameter of the antenna is 23 nm. The resonant length of the antenna on As_2S_3 substrate is 160 nm, and the maximum value is close to 7000 (Fig. 3.22). Resonant length of the antenna is longer than As_2Se_3 case for As_2S_3 substrate as in stripe antennas because of the linear refractive index of the substrate. Results obtained from this simulation are similar to stripe nanoantenna on As_2S_3 substrate.

As a result for single rod shaped antennas effect of linear refractive index of substrate on resonant length and maximum intensity enhancement value is same with stripe case. Also, increase in diameter of the rod leads increase in resonant length and decrease in peak value of enhancement like effect of height in stripe nanoantennas. However, for rod shaped antennas decrease in maximum enhancement value is greater. Moreover, we observe that shape of the antenna effects the resonant antenna length and resonance strength. Rod shaped antennas confines incoming light more efficiently than stripe nanoantennas.

Dipole antennas enhances light at the gap between two antenna arms more efficiently [2]. To take mentioned advantage of dipole antennas we design a new configuration for gold antennas and chalcogenide materials. We insert highly nonlinear As_2Se_3 glass between two identical rod shaped nanoantennas and place them on SiO_2 glass substrate (Fig. 3.23). We observe the electric field distribution on As_2Se_3 glass and around the near field of the antenna. For the simulations antenna length corresponds to one arm length of the dipole antenna, and the

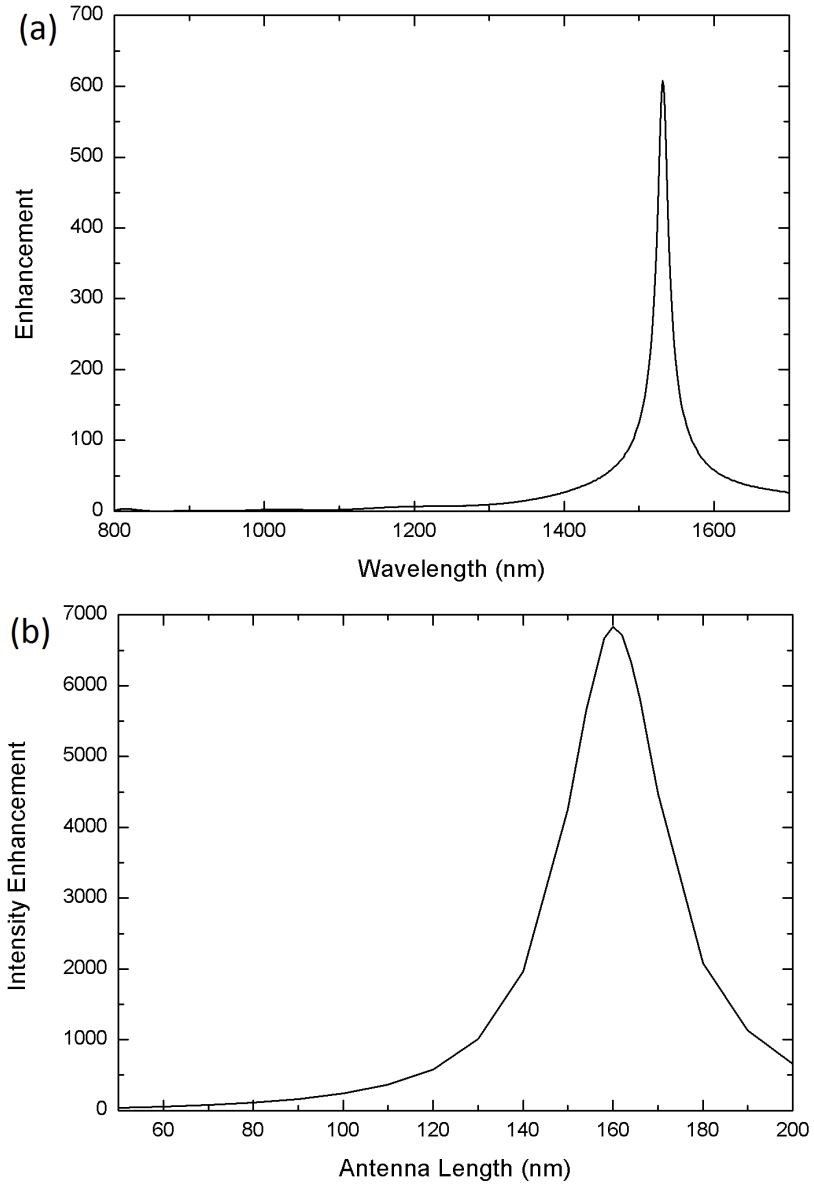

Figure 3.22: (a) Plot of maximum enhancement as a function of wavelength for 80 nm length and 13 nm diameter Au rod shaped antennas on As_2Se_3 substrate. (b) Plot of maximum enhancement as a function of antenna length for As_2S_3 substrate at 1550 nm for rod shaped antenna.

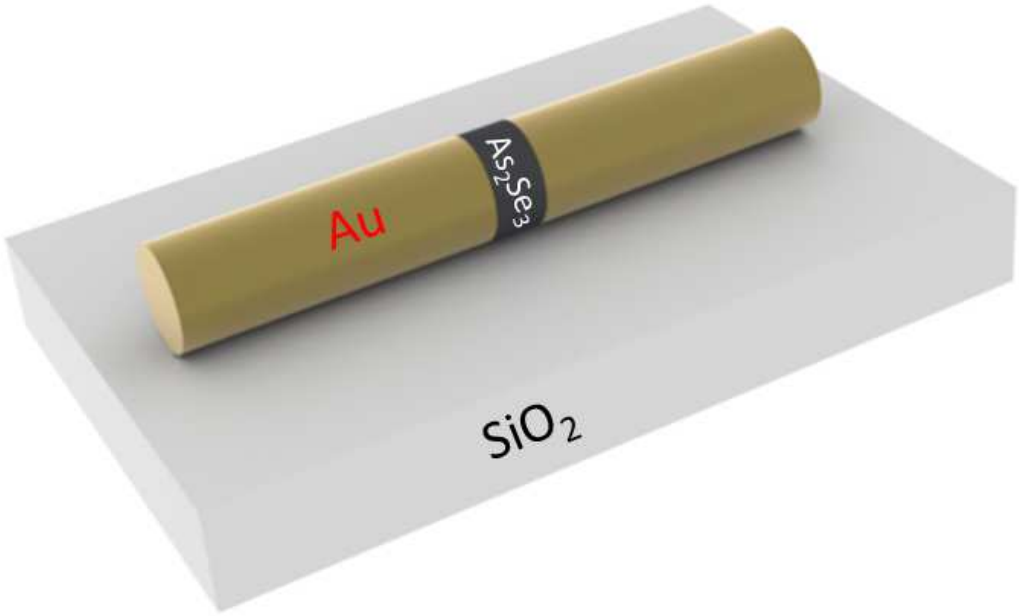

Figure 3.23: Schematic illustration of the simulated dipole antenna structure.

gap distance corresponds to the distance between two arms of the antenna. For all cases, we assume that whole gap is filled by As_2Se_3 material. We perform several simulations for different gap sizes and radius of dipole antenna to investigate effects of these parameters on resonant length and maximum intensity enhancement. Electric field distribution of dipole antenna structure at the surface between antenna and substrate is given in Figure 3.24. Both arms contribute to electric field concentration at the gap. However, since localization on SiO_2 glass is more favourable for light, the greatest enhancement is achieved at the surface of SiO_2 rather than As_2Se_3. On the other hand, enhancement values on As_2Se_3 is enough for third order nonlinear generations.

We simulate the dipole configuration which we mentioned for different diameters to determine resonant length and maximum intensity enhancement. We sweep the arm length from 100 nm to 300 nm for diameters 20 nm to 100 nm, for both variables step size is 10 nm (Fig. 3.25). We select 20 nm fixed gap distance. While the diameter is increasing, intensity enhancement on As_2Se_3 decreases dramatically. Maximum intensity enhancement on As_2Se_3 material is observed for

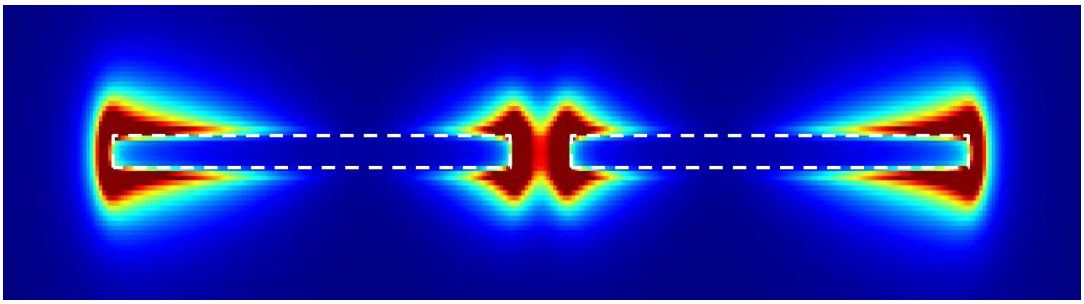

Figure 3.24: Electric field distribution of first resonant mode for dipole antenna.

20 nm diameter and 162 nm arm length and peak value is about 7000. For 60 nm and greater diameter values, maximum intensity enhancement is less than three orders of magnitude. Moreover, increase in diameter drives increase in resonant length of the antenna. A shift in resonant length decreases while the diameter of the antenna is increasing like intensity enhancement.

Since maximum localization is not on the As_2Se_3 for this antenna configuration we investigate the effects of diameter on intensity enhancement at the surface of SiO_2 substrate (Fig. 3.25). Maximum intensity enhancement occurs at 162 nm arm length for 20 nm diameter, as same with intensity enhancement on As_2Se_3. Also on SiO_2 substrate intensity enhancement decreases with an increase in diameter; however it never drops below to 2000, even for 100 nm diameter.

We examine the effect of gap size on resonant length for dipole nanoantenna configuration. We sweep gap size 10 nm to 50 nm and arm length 100 nm to 250 nm, both by 10 nm step size (Fig. 3.26). Diameter of the nanoantenna is fixed and 20 nm. Maximum intensity enhancement is observed for 20 nm gap size at 162 nm antenna length. An increase in gap size causes reduction in maximum intensity enhancement value, but it does not fall down to 5500. Unexpectedly, 10 nm gap size has a less enhancement value than 20 nm case. Resonant lengths of antennas increase by the increase of gap size since interaction between two antenna arms decreases.

We also investigate the effect of gap size on intensity enhancement on SiO_2

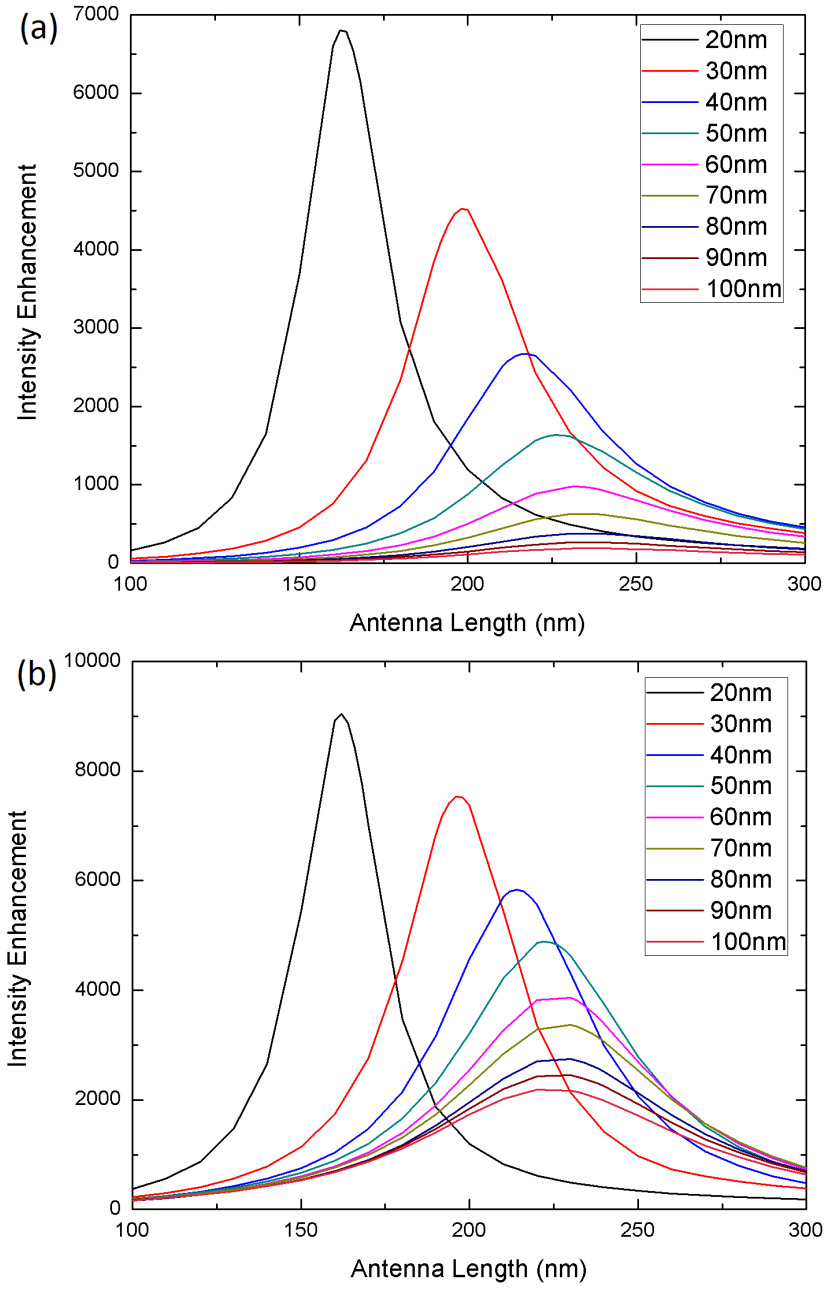

Figure 3.25: (a)Plot of maximum enhancement on As_2Se_3 as a function of antenna length for dipole antennas for different diameter. (b) Plot of maximum enhancement on the system as a function of antenna length for dipole antennas for different diameters.

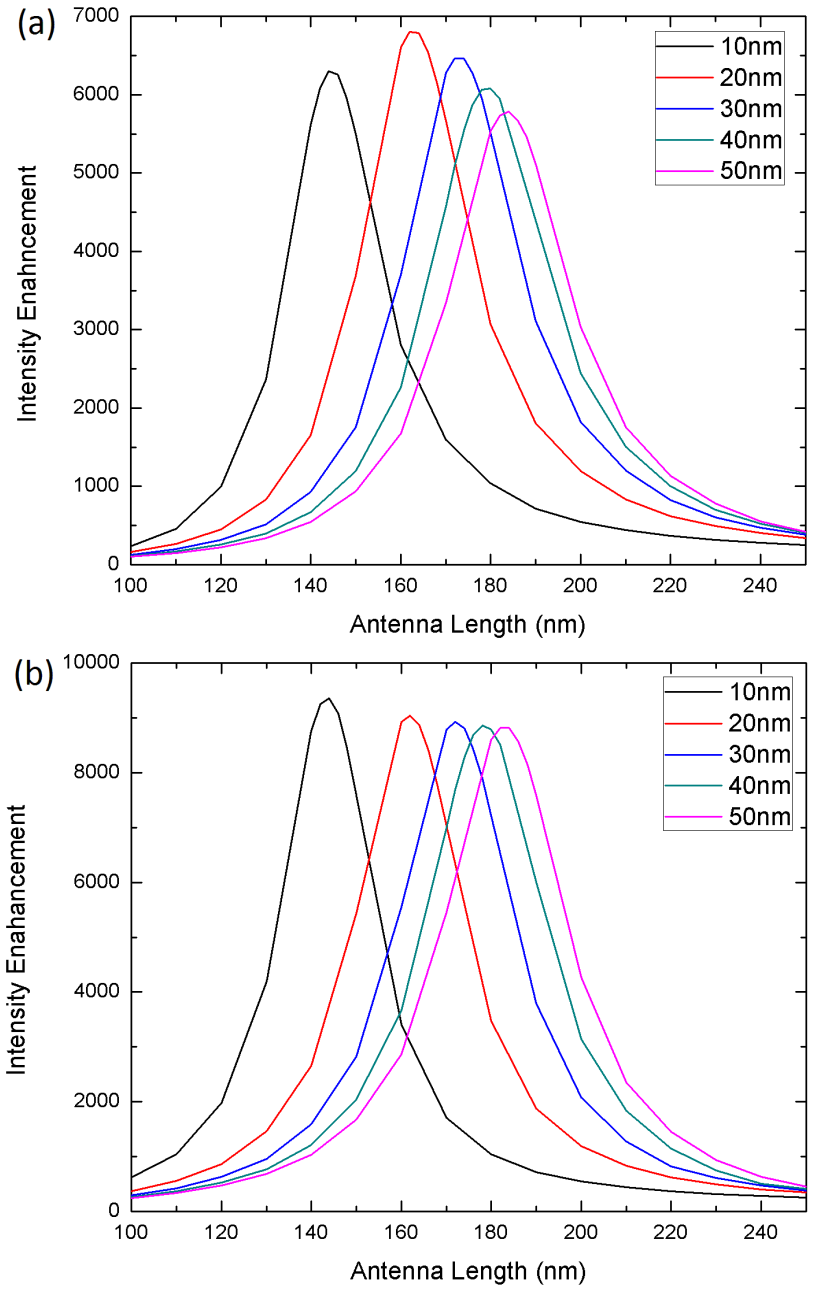

Figure 3.26: (a) Plot of maximum enhancement on As_2Se_3 as a function of antenna length for dipole antennas for different gap sizes. (b) Plot of maximum enhancement on the system as a function of antenna length for dipole antennas for different diameters.

substrate. Even maximum intensity enhancement on As_2Se_3 is maximum for 20 nm gap size, peak of enhancement on SiO_2 is at 10 nm gap size and it is more than 9000. Like As_2Se_3 case peak value decreases and resonant length increases by the increase of gap size. However; reduction on peak value is not too much, even at maximum gap size peak value for enhancement is close to 9000.

As a result, dipole antennas enhances incoming electromagnetic waves at the feed gap region as noted in the literature [6, 8, 20, 31, 32]. Furthermore, gap size and diameter of antenna arms effect resonant length and resonance strength of the system. An increase in gap size decreases the maximum enhancement value and increases the resonant length of the antenna for rod shaped antennas like bow-tie antennas [31]. An increase in diameter also decreases the resonance strength and increases the resonant arm length of antenna like in single rod nanaoantennas.

Chapter 4

Fabrication

In this chapter we will present the fabrication methods for proposed nanoantenna structures step by step wise and scanning electron microscope (SEM) images of fabricated structures. We had fabricated proposed antenna-substrate structures by using electron beam lithography (e-beam lithography) and seed-mediated chemical techniques. Also we had tried to fabricate these structures by using anodized aluminum oxide (AAO) templates; however we could not optimize the process to produce antennas on the desired substrate.

Nowadays there are several techniques for fabricating metal nanostructures, such as e-beam lithography [6, 28, 31], x-ray lithography [46], focused ion beam milling (FIB) [8], near field lithography [47], on-wire lithography [20] and nano imprint lithography [48]. One of the fabrication techniques which we used is the e-beam lithography technique. This technique allows us to fabricate ordered nanoantenna structures, and the size distribution of the fabricated nanoantennas are narrow. On the other hand it is not useful for large area applications since it takes time to fabricate. For e-beam lithography one should optimize parameters such as voltage, current, resist thickness, dose and shape sizes. We optimized these parameters according to our requirements, after several experiments. For the second technique which we were able to fabricate antennas, seed-mediated chemical technique, size distribution of the fabricated structures are so wide but the technique enables large area fabrication, since we can fabricate plenty of

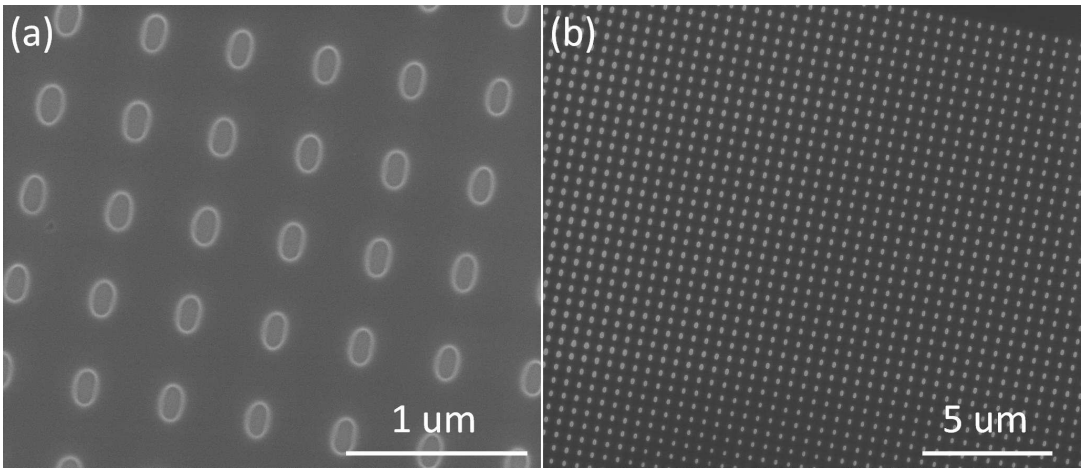

Figure 4.1: SEM images of defined holes on PMMA after the e-beam exposure. (a) Length of the holes are 190 nm. (b) Size of the hole arrays are 25x25 μm

antennas just in one process. For this technique we optimized ratio of chemicals experimentally. Fabrication by AAO membranes is the last technique which we tried to fabricate designed nanoantenna-substrate structures. This technique provides us both narrow size distribution and enables large area fabrication. Although we optimized almost all the parameters such as voltage, time and pH value of solution for fabrication of antennas at desired size, we could not locate the fabricated antennas on As_2Se_3 substrate.

4.1 Electron Beam Lithography

By using the e- beam lithography technique we basically fabricated two different antenna-substrate configurations. For the first configuration antennas located on As_2Se_3 substrate (Fig. 3.2) and for the second configuration they are sandwiched between Si wafer and As_2Se_3 film (Fig. 3.14). We simulated the structures for both configurations and results show that in both design continuum and third harmonic generation is possible. We proposed the second design due to difficulties in fabrication process of first configuration. We succeed in fabrication of both of

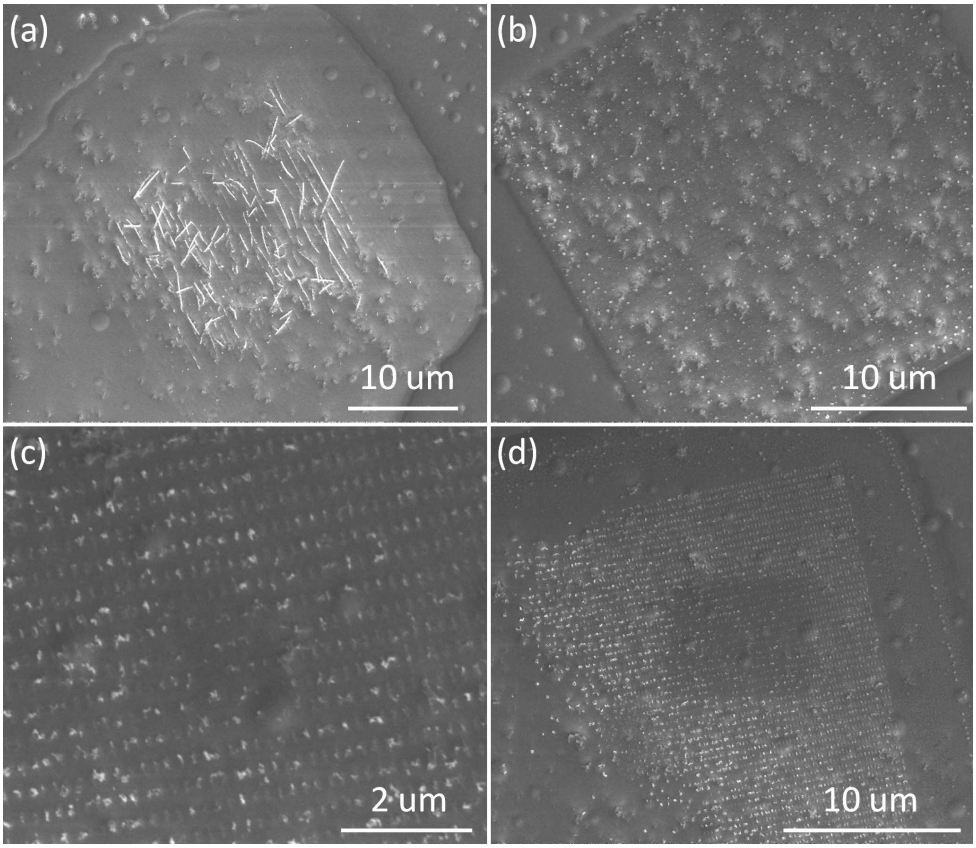

Figure 4.2: SEM images of the removed gold antennas on the As_2Se_3 substrate. (a) The aggregated gold particles on the substrate. (b) Some of the antennas are on the substrate at the center part but most of them are removed. (c-d) Some gold particles on the substrate but they are not in the desired and well defined shapes.

the antenna-nonlinear material structures.

For the first configuration, to fabricate gold nanoantennas we get a silicon (Si) wafer and clean it by using isopropanol and acetone. During the cleaning process we put the wafer in both liquids one-by-one and sonicated each approximately 5 minutes for each turn. Lastly we rinse and dry the wafer. Since the structures are so small, the cleaning step is important to fabricate high quality structures. After the cleaning procedure we thermally coat 1 μm As_2Se_3 on Si wafer. However, after lift-off step As_2Se_3 and everything on the sample go away and we get just bare

silicon at the end of the whole fabrication steps. There are two possible reasons for this problem: either As_2Se_3 dissolved in one of the chemicals which we use during the fabrication or As_2Se_3 layer goes away by sticking the Poly(methyl methacrylate) (PMMA) layer at the lift-off step. To determine the reason, we dip the As_2Se_3 coated sample into all chemicals which we use in fabrication and check whether As_2Se_3 dissolved or not. We observe that it does not dissolve in any chemicals. Therefore, we realize that the As_2Se_3 sticks to PMMA better than Si and removes at the lift-off step. Then we plasma etch the surface of Si to make it rough and keep As_2Se_3 on it, but this method does not work well. Therefore, we try to coating adhesion layer between As_2Se_3 and Si wafer and coat 1 nm Cr or 5 nm Ge on different samples by thermal evaporator as adhesion layer. For this fabrication adhesion layer is one of the key points since As_2Se_3 layer goes away by sticking PMMA layer at the lift-off step when we coat As_2Se_3 on just bare Si wafer. This is the most important challenge for this fabrication process.

After adhesion layer we coat 1 μm As_2Se_3 on the sample again thermal evaporation technique. The main problem of this deposition technique for chalcogenide glasses is necessity for rapid annealing after the deposition to avoid removal of the film in the next steps of the fabrication [16, 34]. Therefore, we annealed the thin film As_2Se_3 coated sample in a vacuum oven at 180 °C for 2 hours by increasing the temperature 3 °C/min rate from room temperature to desired value. After the annealing step we spin coat PMMA, NANO 950 PMMA A2, on top of the sample as resist for e-beam lithography by spin coating. For 50 nm height antennas we coated 100 nm PMMA by rotating sample 1 minute at 1000 rpm speed. We pre-bake the PMMA coated sample 90 s at 180 °C on a hot plate. For smaller height antennas it is useful to coated smaller thickness of PMMA, because small thickness of PMMA layer allows the fabrication of antennas with sharper edges. After PMMA coating we expose the sample to get desired shapes on it by using FEI Nova NanoSEM 600 + Raith ElphyPlus e-beam lithography system. For the exposure we use 30 kV and 26 pA as beam properties and 50x50 μm^2 for exposure area. To get the desired sizes of the shape we use dose factor array, we start with dose as 200 and increase it 10% in every next antenna matrix until dose value as 600. In an antenna matrix there are 5000 antennas with

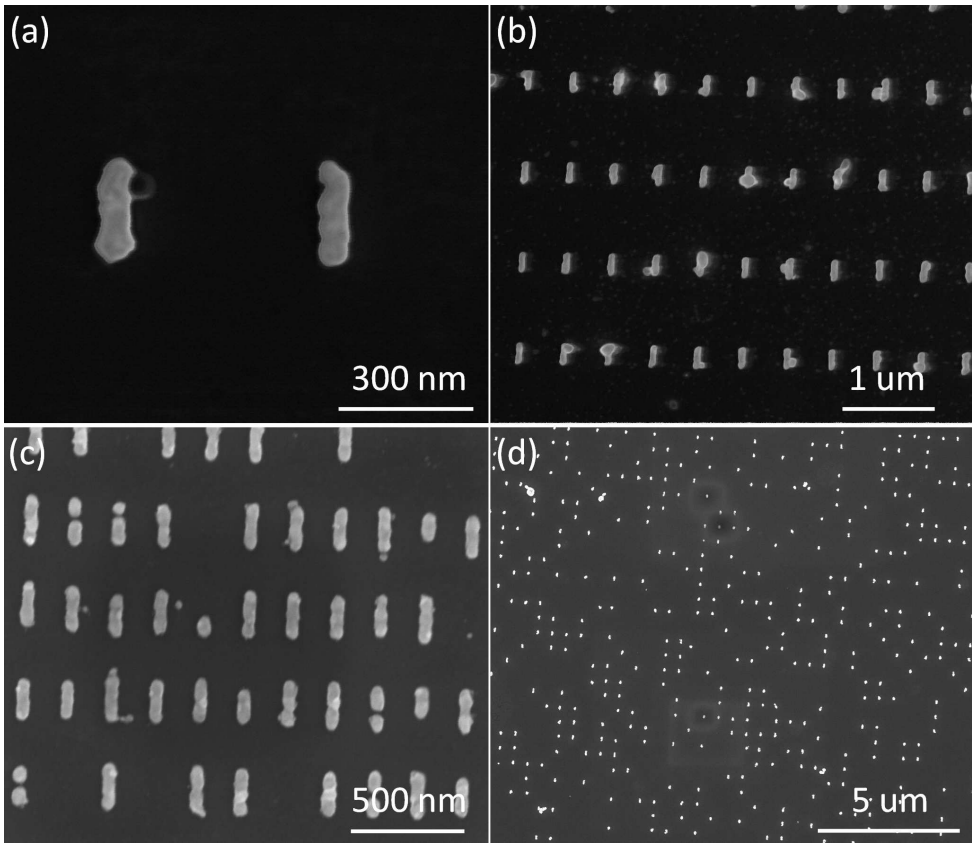

Figure 4.3: SEM images of the gold nanoantennas on As_2Se_3 without adhesion layer between gold and the As_2Se_3 substrate. (a-b) It is possible to fabricate antennas on As_2Se_3 substrate but the edges of the antennas are not sharply defined. (c-d) There are some missing antennas in the array configuration and some of the nanoantennas are defected.

500 nm gap in x axis and 1 μm gap in y axis. After e-beam exposure we dip the sample in developer and stopper solutions for 50 s and 20 s respectively and dry it with a low-nitrogen flow. At this point of process we have the holes on PMMA (Fig. 4.1) where we will put the nanoantennas inside. Even we draw the structure in rectangle shape with sharp corners in the mask design tool of e-beam lithography equipment, shape at the output have curved corners in Figure 4.1. Also the sizes of long and short edges at the output different than determined sizes at mask design. Therefore, we design the mask according to the results at the output, and to fabricate 50x190 nm rectangle we draw the mask as 20x210

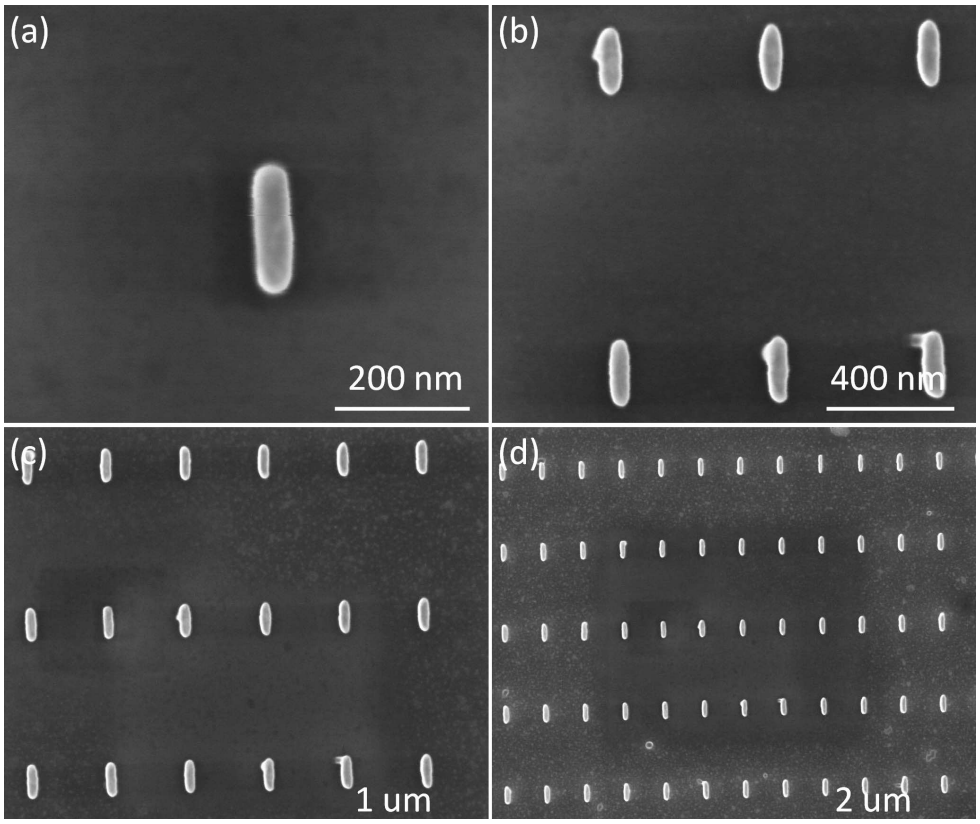

Figure 4.4: SEM images of the gold nanoantenna on As_2Se_3 substrate with an adhesion layer between gold and As_2Se_3. (a) Close view of a fabricated gold nanoantenna on As_2Se_3 substrate at resonant length. (b-d) Array configuration of the gold nanoantennas.

nm sizes. Also, dose factor effects the sizes of holes and antennas. After several experiments we optimized these variables to fabricate holes at desired sizes, but we cannot overcome the curvature problem at the corners. One possible solution for this problem is using thinner PMMA coating as resist layer.

In the next step we post-bake the sample for 90 s at 100 °C again on a hot plate. Then we deposit 50 nm gold as antenna material. At first trails we encounter problems of removal of antennas on As_2Se_3 substrate (Fig. 4.2). To solve this problem we try to optimize deposition rate of gold to have better layer and we insert adhesion layer between As_2Se_3 and gold. Then we deposit 1 nm Cr, Ti and Ge as adhesion layer for nanoantennas on different samples according

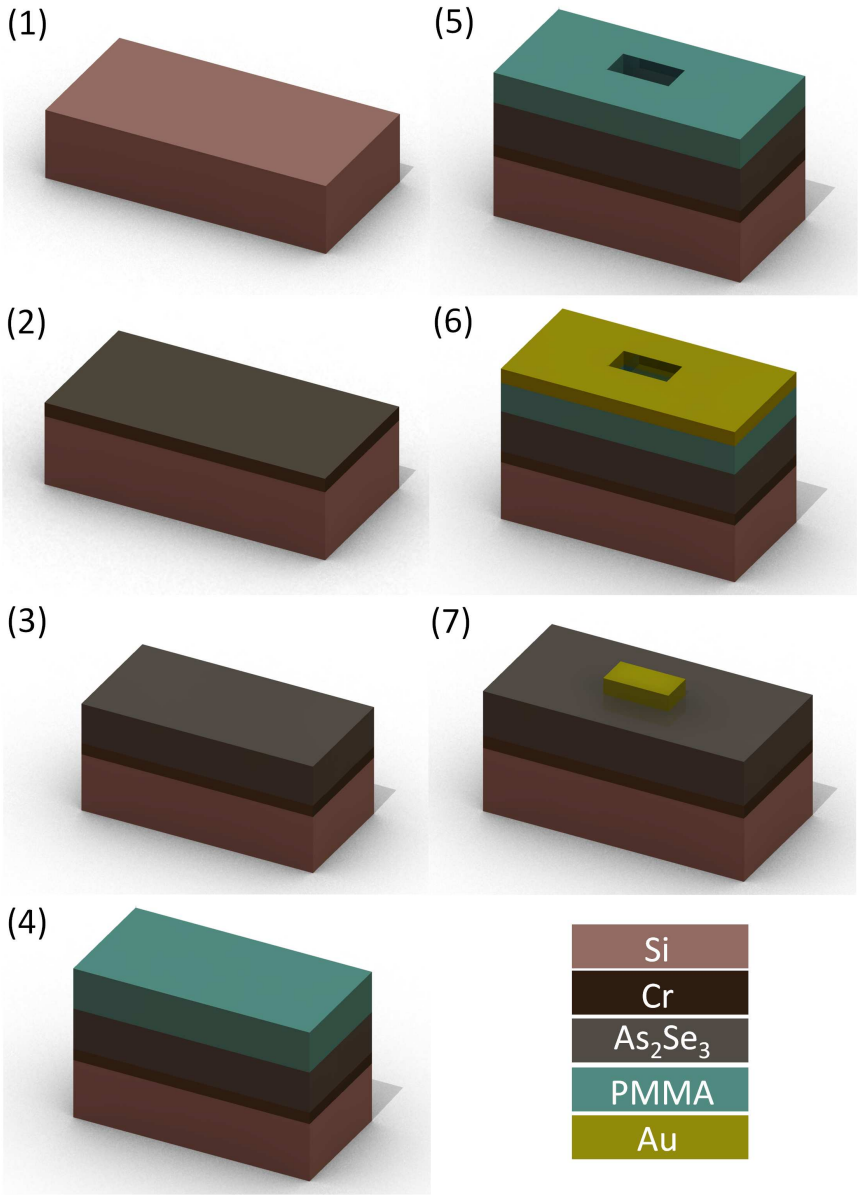

Figure 4.5: The fabrication steps of gold nanoantenna on As_2Se_3 by e-beam lithography. (1) Properly cleaned Si wafer. (2) An adhesion layer coated Si substrate. (3) As_2Se_3 evaporated sample. (4) Spin coated PMMA on the sample. (5) Defined holes on PMMA after e-beam exposure. (6) Evaporated gold on prepared sample. (7) Gold nanoantenna on the As_2Se_3 substrate after the lift-off of PMMA and excess gold.

to their resonant lengths in chapter 3 and coat 50 nm gold as antenna material at 0.5 Å/s rate on both sample with and without adhesion layer . We select this rate to have a high quality of coating and avoid removal of antennas. For all the samples we fabricate gold antennas on As_2Se_3 substrate successfully. An adhesion layer has a key role in that step again. In our trials without an adhesion layer we saw that quality and shape of antennas are not good as in the existence of adhesion layers. Figure 4.3 shows the gold antennas on As_2Se_3 glass without any adhesion layer. Edges of antennas are not so sharp and some of the antennas are defected. On the other hand, antennas at Figure 4.4 are placed on 1 nm adhesion layer have smooth surface, and we have better quality. However, adhesion layer reduces plasmonic effects significantly as we mentioned in simulations part of the work. For deposition of both adhesion layer and gold we use thermal evaporation technique. Lift-off is the last step of the fabrication process for this design. We put the sample in acetone at 40 °C and wait for 1 hour for lift-off. As a result we get the gold nanoantennas on As_2Se_3 substrate at designed sizes after simulations. Figure 4.5 shows the schematic of fabrication steps of first design.

For the fabrication of the second design we have similar steps with the previous one. Again we start with substrate cleaning step with the same procedure. Then we coated PMMA on Si wafer and expose it by using same properties in previous process but the length of the antenna. According to our simulation results in that case the resonant length of the antenna is not the same with first design (Fig 3.15), so we expose the PMMA in its resonant length. After exposure we coat the antenna layer again by thermal evaporation. In that case we do not use adhesion layer since it is not necessary for Si wafer. Then we apply the same lift-off procedure which we mentioned above and get gold nanoantennas on Si wafer (Fig. 4.6). In the last step of this process we thermally coat 100 nm As_2Se_3 on the sample. Figure 4.7 shows the schematic of fabrication steps of second system.

When we compare these two different designs according to fabrication process we see that the fabrication of the second design is easier than the initial one, since there is no necessity for adhesion layer under the As_2Se_3 thin film and gold antennas. Also, gold nanoantennas on bare Si have sharper shape than antennas on As_2Se_3 thin film without adhesion layer. Having sharper corners allows the

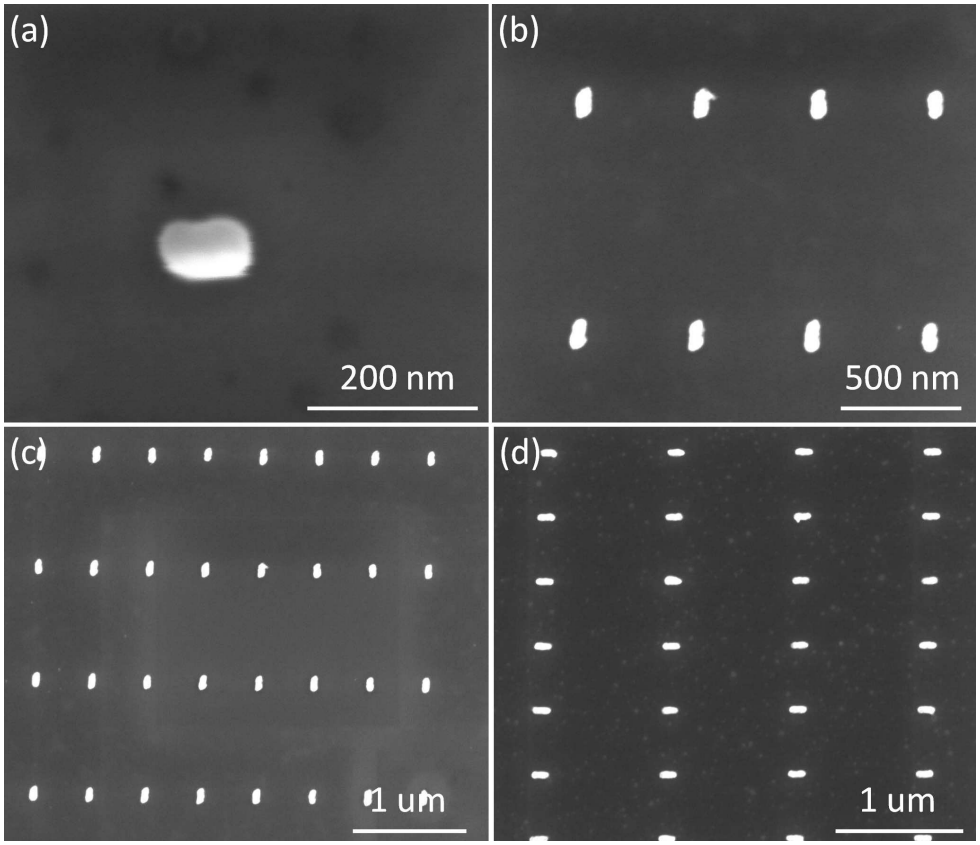

Figure 4.6: SEM images of the gold nanoantenna on the Si substrate fabricated by the e-beam lithography. (a) Close view of a fabricated gold antenna on Si substrate before the evaporation of As_2Se_3. (b-d) Array configuration of the gold nanoantennas.

second design to have more enhancements at the near field of nanoantenna. On the other hand for the first design, it is natural to have more enhancement values than the second design according to simulation results since it just localizes the incoming light on As_2Se_3 glass.

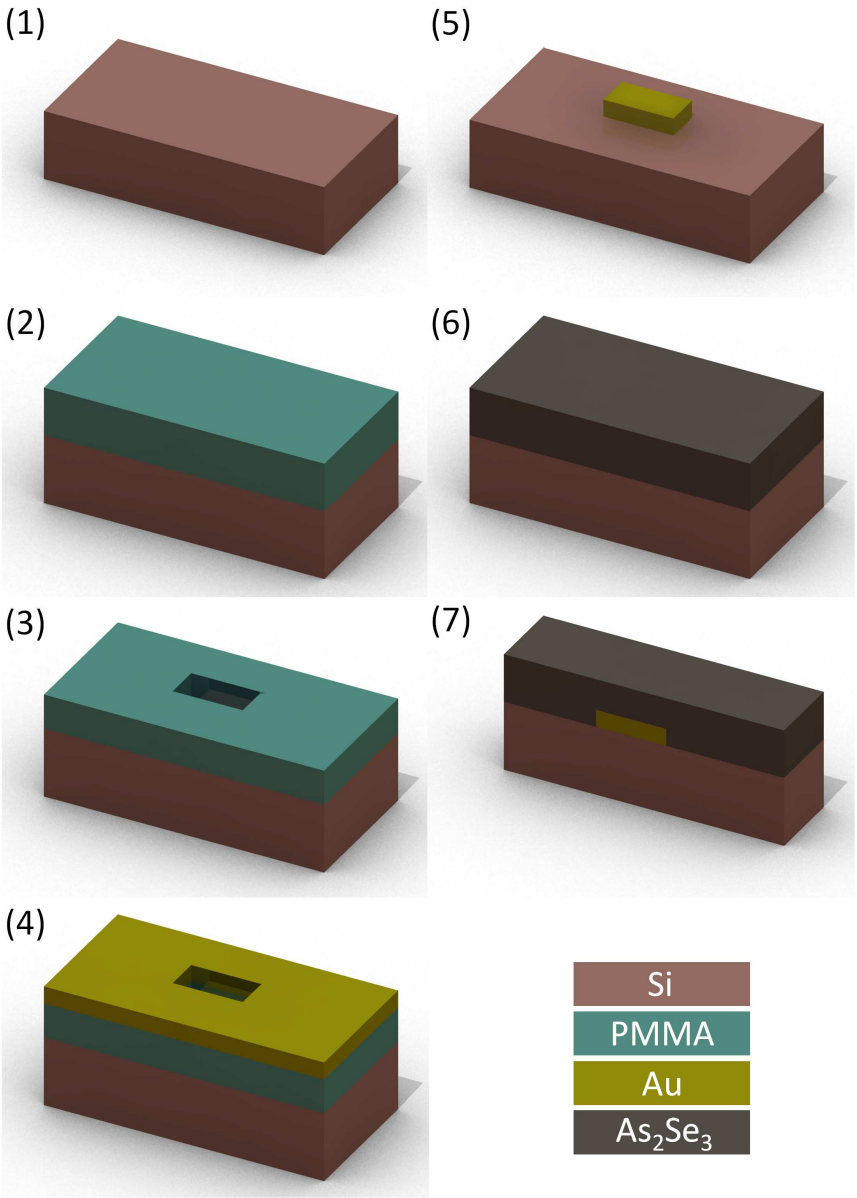

Figure 4.7: Fabrication steps of gold nanoantenna sandwiched between As_2Se_3 and SiO_2 by e-beam lithography. (1) Properly cleaned Si wafer. (2) Coated PMMA on Si substrate. (3) Defined holes on PMMA after e-beam exposure. (4) Evaporated gold on prepared sample. (5) Gold nanoantenna on the Si wafer after the lift-off of PMMA and excess gold. (6) Coated As_2Se_3 on gold antenna and Si wafer. (7) Cross sectional view of the prepared structure.

4.2 Seed Mediated Chemical Technique

Nowadays, metal nanoparticles in various shapes such as spheres [49], triangular prisms [50] and rods [51, 52] are fabricated by using wet chemical techniques. We fabricate rod shaped gold nanoantennas by seed mediated growth. Under the base of this technique firstly we prepare spherical gold seeds by adding strong nucleating agent sodium borohydride ($NaBH_4$) into chloroauric acid ($HAuCl_4$)-trisodium citrate solution. $HAuCl_4$-trisodium citrate solution contains 20 mL deionized water, 1.25×10^{-4} M $HAuCl_4$ and 2.50×10^{-4} M trisodium citrate. We mix them at room temperature. Then we add freshly prepared, ice-cold 0.3 mL 0.01 M $NaBH_4$ solution into first solution while stirring vigorously. After 30 s we slow down the stirring and it continues for 15 min slowly at 45 °C. 3.5 nm seeds are produced in the solution. After preparation of seeds, we prepare the growth solution by firstly adding 1.25×10^{-4} M $HAuCl_4$ and 0.008 M CTAB into 10 mL deionized water. Into this solution we add 0.025 mL 0.1 ascorbic acid and mix them. After preparing growth solution we add 25 μL seed solution to it and wait overnight. Growth steps of nanoantennas are given in Figure 4.8.

To optimize length of the rods, we tried different amount of CTAB and seed solution for synthesis. If we increase the CTAB and seed solution concentration length of the rods are increases. CTAB bounds the [110] face of the seeds so it force to growth of gold at [111] face. Figure 4.10 shows synthesized gold rods at different lengths. Long rods have better size distribution then short ones. Also, yield in long roads are higher. After synthesizing gold nanoantennas in solution we disperse them on substrate by spin coating them at 1000 rpm for 2 min. Figure 4.11 shows the dispersed antennas on substrate. We spin coat them to distribute rods with a distance enough for not coupling each other. In drop-cast deposition rods stay too close to each other and it effects their resonant length. This fabrication technique allows large area fabrication, but size distribution of antennas are wide and yield of synthesis is not high. By experimentally optimizing concentration of chemicals one can overcome these problems.

Also we synthesized gold nanorods by using different recipe [53]. In that case we use hydroquinone instead of ascorbic acid. In that recipe again we prepare

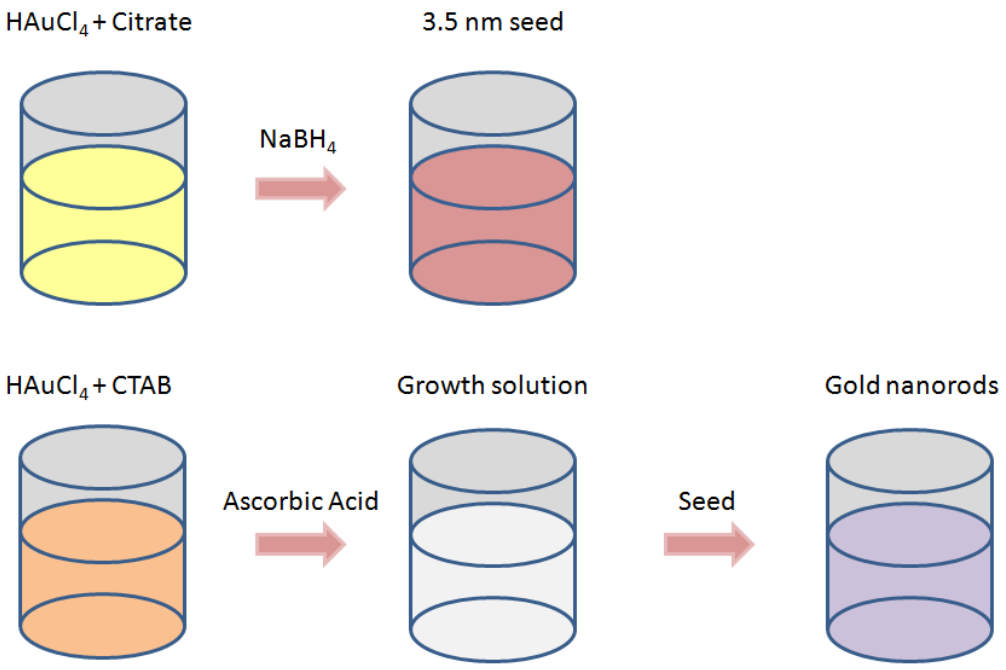

Figure 4.8: Synthesis steps of gold nanoantennas by the seed-mediated chemical technique. 3.5 nm seeds are prepared by the mixture of $HAuCl_4$, citrate and $NaBH_4$. Gold nanorods are fabricated by adding seed into the mixture of $HAuCl_4$, CTAB and ascorbic acid.

seed. To synthesize seed firstly we add CTAB in the $HAuCl_4$ and we mix it with $NaBH_4$ and sodium hydroxide (NaOH). After seed preparation we prepare growth solution by adding silver nitrate ($AgNO_3$) and hydroquinone ($C_6H_4(OH)_2$) into $HAuCl_4$ and CTAB. Lastly we mix seed and the growth solution and age it overnight. By changing hydroquinone, seed, silver and gold concentrations one can synthesize nanorods with different size. This recipe gives better yield than the first one and the size distribution is also narrower. By this technique we synthesized nanorods with 80 nm length and 13 nm diameter (Fig. 4.11). This rods gives absorption at around 1.1 μm in water with the measurements with Varian Cary 5000 UV-Vis-NIR Spectrophotometer (Fig. 4.9). Also we compute the resonant wavelength of fabricated nanoantennas in water by simulating the structure. To simulate this system we assume the refractive index of water 1.32 and insert the antenna inside water. According to Figure 4.9 we can say that

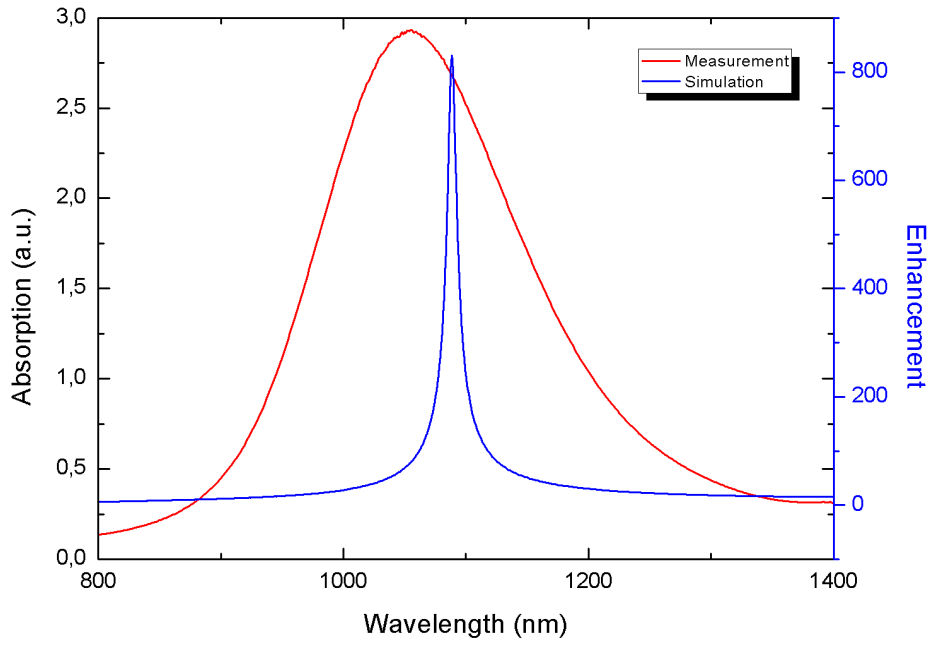

Figure 4.9: Absorption and enhancement spectrum of fabricated nanoantennas in water.

measured absorption spectrum and simulation results are consistent. Peak is wider in measurement and sharper in simulation because there is not any size distribution in the simulation. We try to get this measurement after dispersing antennas on substrate but density of the antennas is not enough to get meaningful signal from the device.

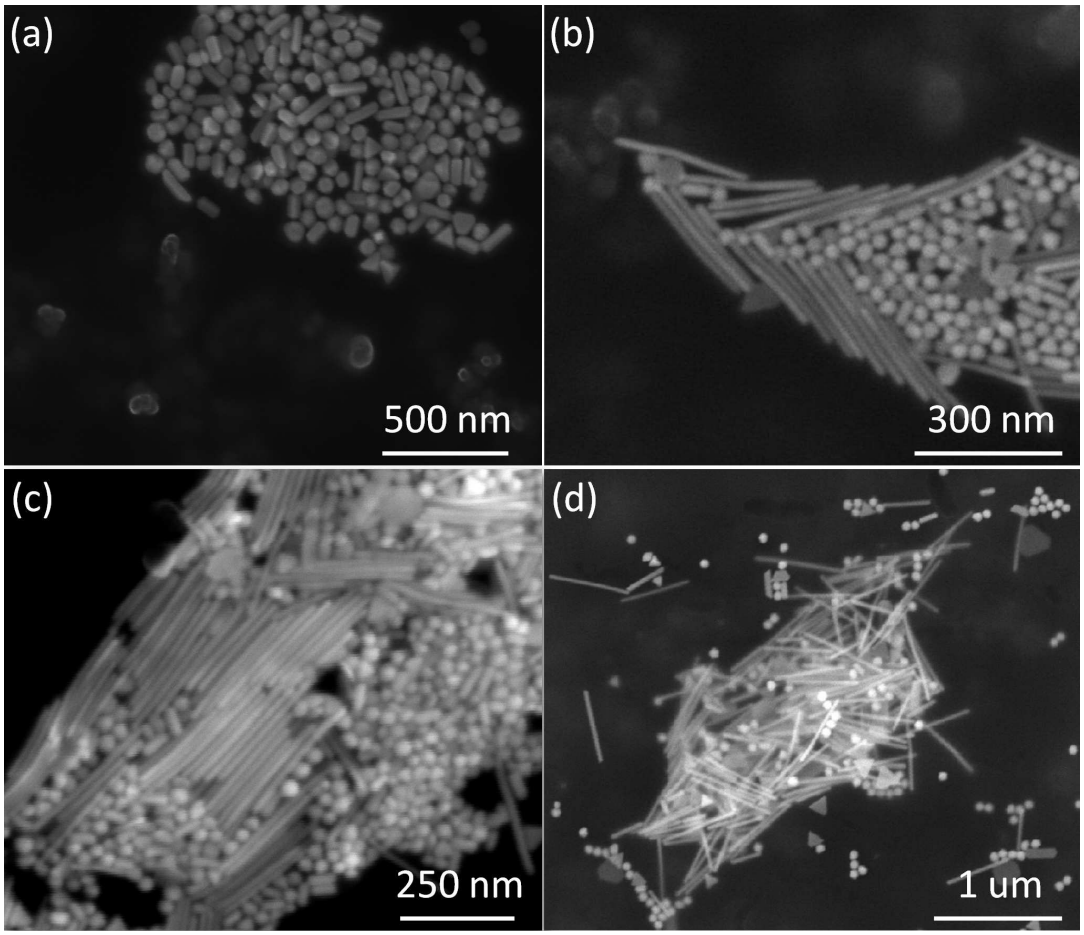

Figure 4.10: SEM images of gold nanoantennas fabricated by seed-mediated chemical technique at different lengths. (a) The gold rods with length around 150 nm. (b-c) The gold rods with length 300 and 500 nm. (d) The gold rods at micron scale. Yield of the process increases by the increase in length of the fabricated rods.

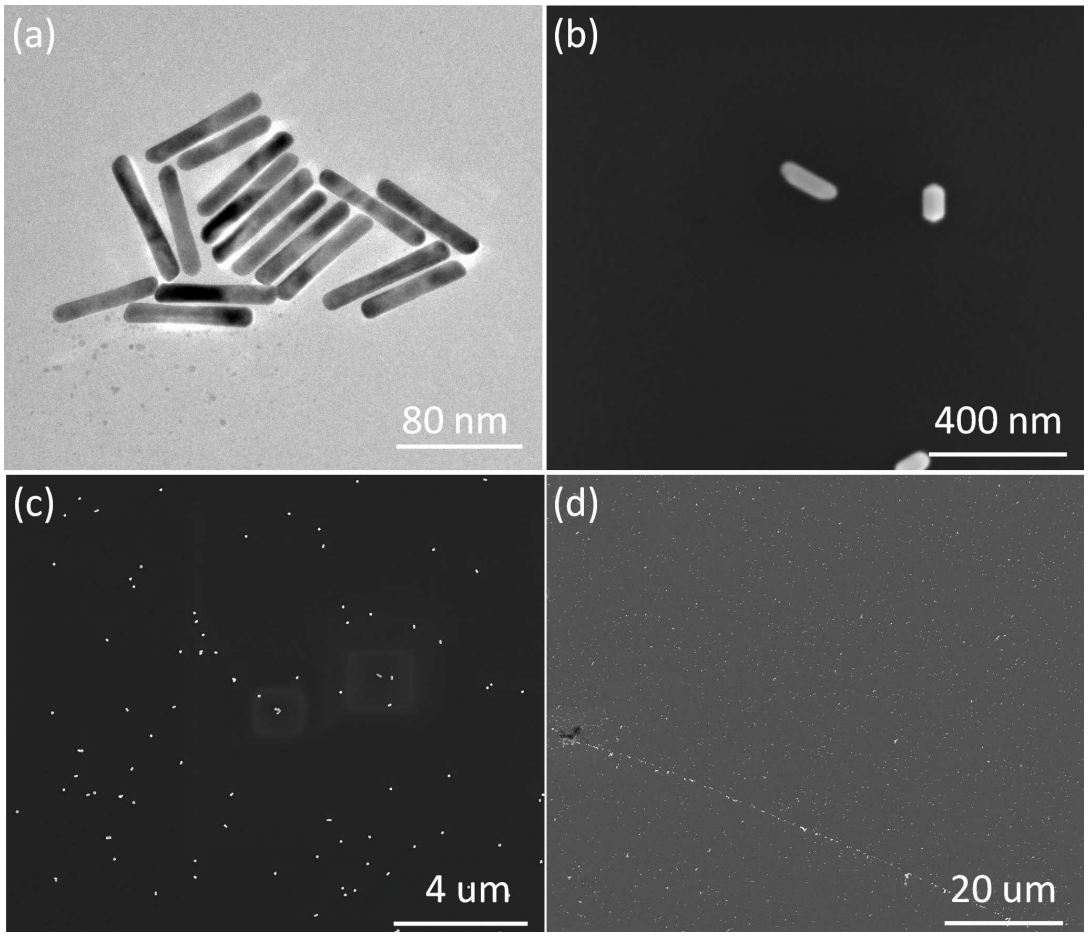

Figure 4.11: SEM and TEM images of the gold nanoantennas fabricated by two different seed-mediated chemical technique. (a) TEM image of fabricated nanoantenna. (b) Close snapshot of the single antennas. (c-d) General view of the antenna distribution on the substrate.

4.3 Anodic Aluminum Oxide

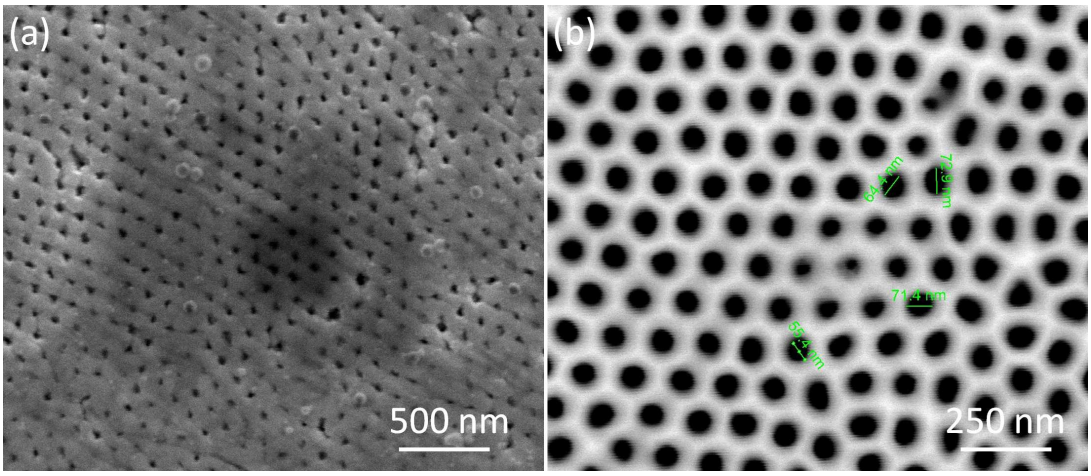

Figure 4.12: (a) SEM image of branched side of the AAO membrane. (b) SEM image of clear side of the AAO membrane.

In this fabrication technique of nanoantennas we tried to fabricate rod shaped antennas by electro deposition using AAO membranes as templates. AAO membranes have very advantageous properties such as structural regularity and uniform pore size to fabricate narrow size distributed structures. Moreover, the membranes are chemically inert and have high mechanical hardness. This allows us to use them in different chemicals and fabrication processes [54]. Pore sizes of membranes can be arranged from 10 nm to 300 nm and the thickness of the membrane can change between 100 μm to 300 μm. In our case, we get the membranes from one of our collaborators, and the pore size of the membranes is about 70 nm and the thickness is 3 μm. Two sides of the membrane have different surface properties. The holes at a side are clear but for the other side holes are branched. SEM images of closed and clear sides of the membrane is shown at Figure 4.12.

According to simulation results in chapter 3 we should growth 258 nm gold in the pores of AAO membrane to fabricate them at resonant length (Fig. 3.21). To achieve this goal we try to fill these pores using thermal evaporation. At the first step, we clean a Si wafer properly and stick AAO membrane on it by

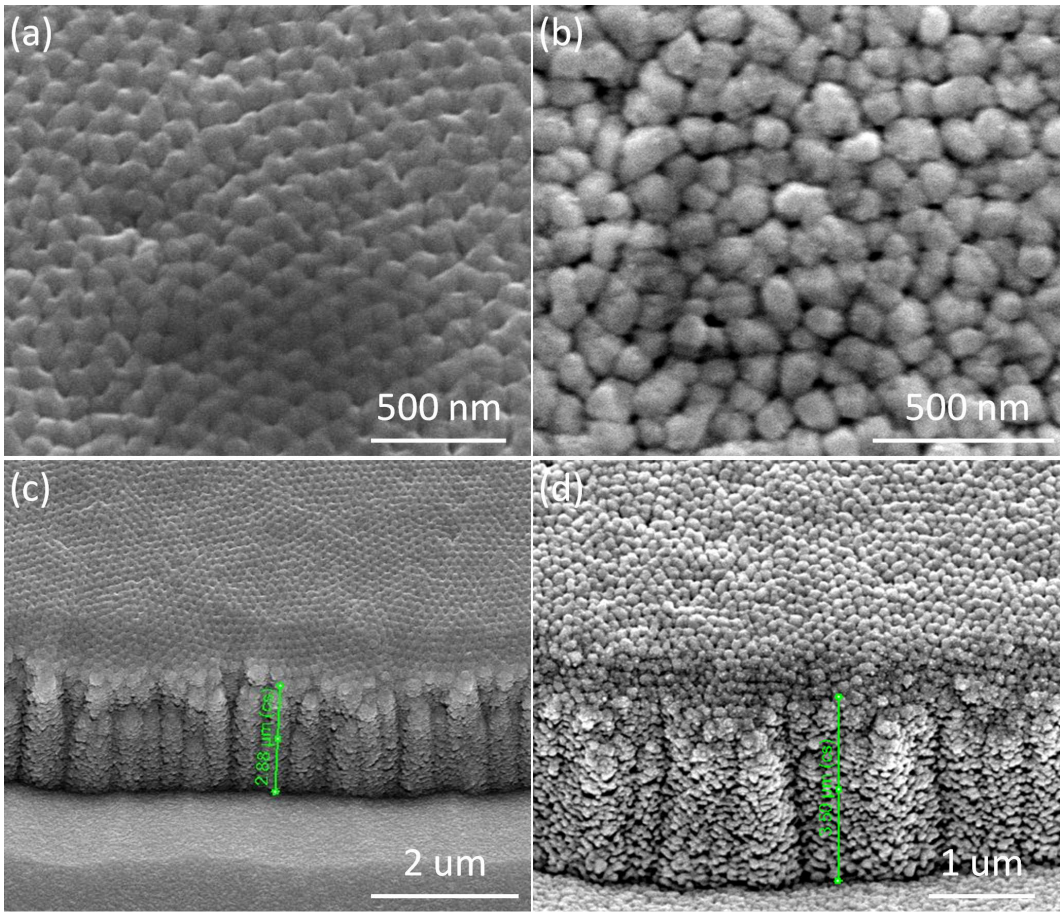

Figure 4.13: (a-b) Top view SEM images of the AAO membrane after different amount of gold deposited. (c-d) Side view SEM images of the AAO membrane after different amount of gold deposited.

isopropanol. In this step, it is important to put the membrane on a wafer with the branched side facing up. After sticking the membrane we etch and open the branched holes of the membrane by inductive coupling plasma (ICP) etch STS-LPX SR (F) model equipment. We etch the structure by Ar plasma for 40 minutes at Ar flow rate 30 sccm and power for coil and platen 300 W and 200 W respectively. During the process temperature of platen chiller is set to 20 °C. We optimized these values for ICP etching after some experiments. At the end of the ICP etching step we get clearly opened holes as at Figure 4.12. Then we thermally evaporate gold on this structure, but gold does not fill the pores fully

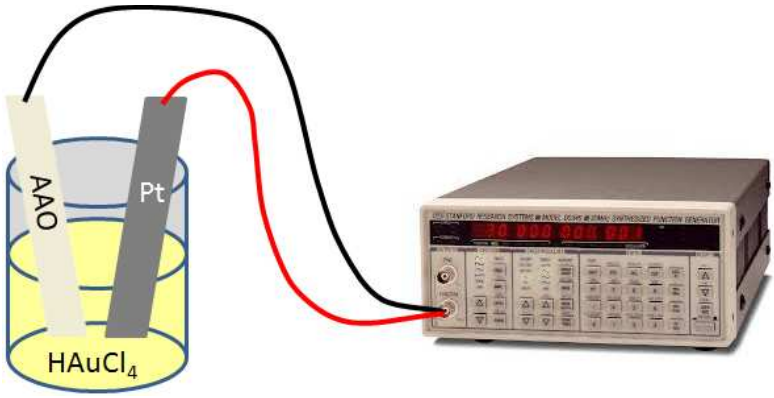

Figure 4.14: Schematic illustration of the electrodeposition setup. Pt stick and AAO membrane is connected to positive and negative ends of the output respectively. The electrolytic solution contains 5 mg $HAuCl_4$ into 10 mL deionized water.

as we expect. Gold does not go too deep in the pores but accumulates at the top and generates holes at the surface as seen in Figure 4.13. After some experiment we realize that it is not possible to fabricate designed rods at desired lengths by thermally evaporating gold on AAO membrane. Therefore, we skip to a new fabrication technique for filling gaps with gold and we try electro deposition.

For depositing gold by electro deposition we start with cleaning step. After that as first step of process we coat 1 μm silver on the wafer by thermal evaporation. This layer is just a contact for electro deposition step. 1 μm deposition is not common thickness for contact and it takes too much time for deposition, but thinner layers of silver oxidise and lift-off from the substrate when we dipped it in acidic electrolyte solution. After thermal evaporation of silver we put the AAO membrane on the top of silver and stick it by isopropanol like in previous technique. Again we put the branched side of membrane facing up, and etch it to clear pores. At electro deposition step, we prepare electrolytic solution by adding 5 mg $HAuCl_4$ into 10 mL deionized water. Then, we dip the anode (Pt electrode) and the cathode (AAO membrane) inside the bath (Fig. 4.14). We applied different DC voltage values to optimize height of deposited rods. In our first trials, we fabricate antennas which are too long for our application. Fabricated rods

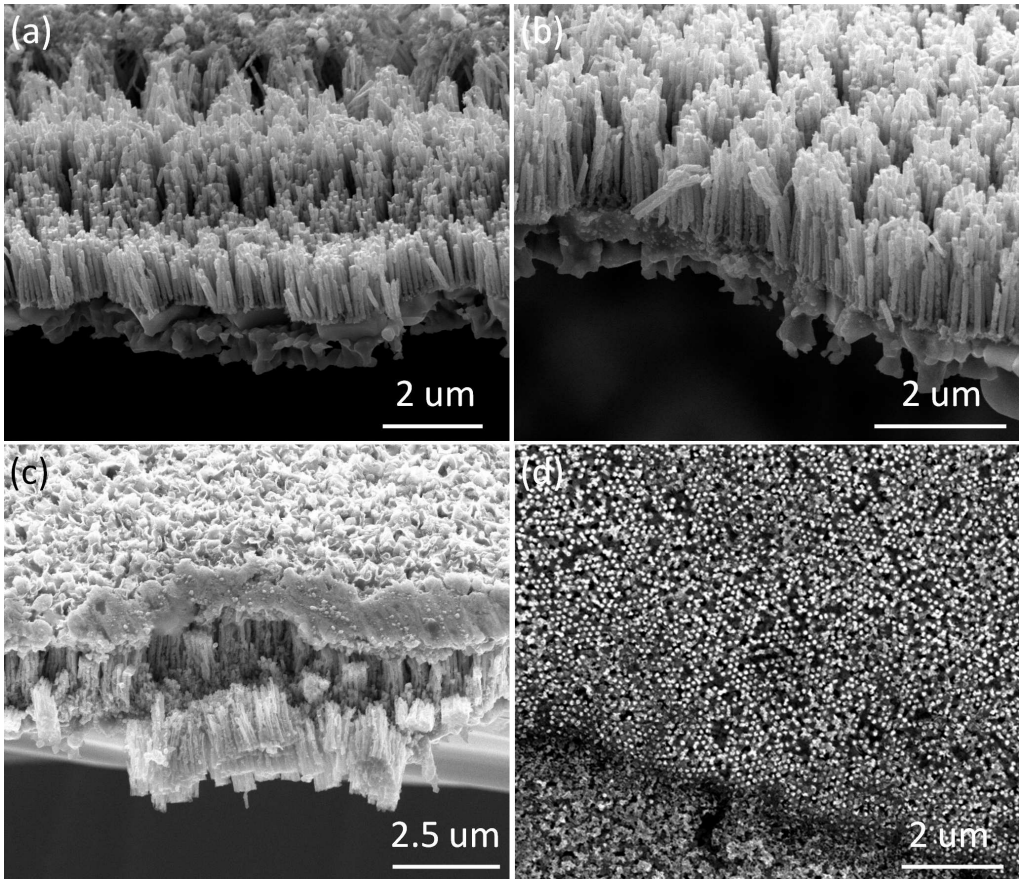

Figure 4.15: SEM images of the micron scale gold rods after etching the AAO membrane. (a-b) Side view of the micron scale gold rods. (c) Side view of gold rods which exceeds height of the membrane. (d) Top view of the micron scale gold rods.

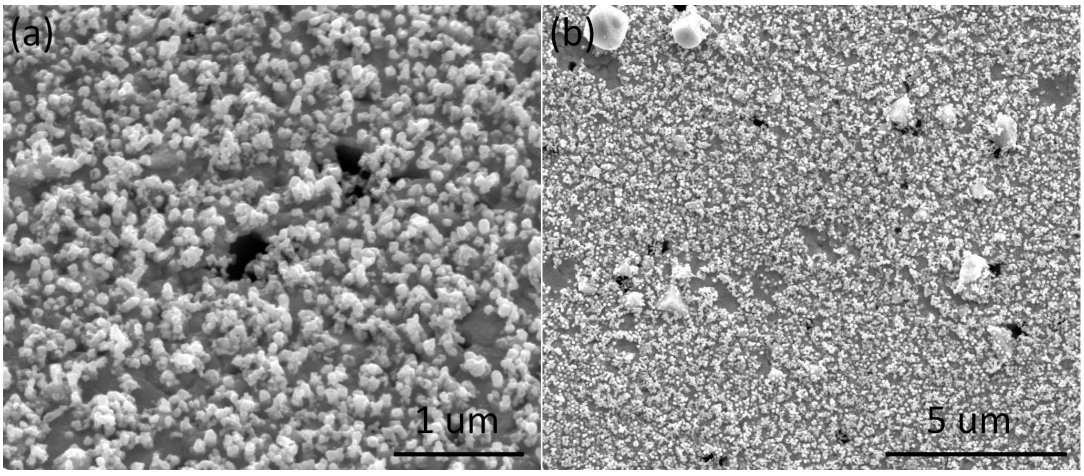

Figure 4.16: SEM images of nanometre scale gold rods on wafer after etching AAO membrane by H_3PO_4.

by using this method in the literature are also at micron scale or nano scale for larger diameters [55]. To reduce length of the rods we reduce the applied voltage, concentration of electrolyte and deposition time. Even for 5 s deposition under continuous DC voltage sizes of rods become at micron level (Fig. 4.15). Then we applied 20 mV DC to system for just 125 ms by using Stanford Research Systems DS345 function generator as pulse to reduce height of deposition. By this modification we fabricated gold rods at nanometre scale (Fig. 4.16). After deposition of gold inside the holes we etch the AAO membrane by waiting overnight inside phosphoric acid (H_3PO_4). Lastly, we tried etching silver in nitric acid (HNO_3) but there is an unexpected black layer which antennas stick on it and we cannot get gold rods by centrifuge. Probably silver oxidized and this oxidized layer keeps gold rods. Maybe different chemicals can etch this layer and one can get the rods in a liquid and spread them on As_2Se_3 substrate by spin coating like we did in seed mediated chemical technique. This technique also allow us to fabricate dipole antenna configuration by inserting another material between two gold rods. Schematic illustration of fabrication steps of the technique is given at Figure 4.17.

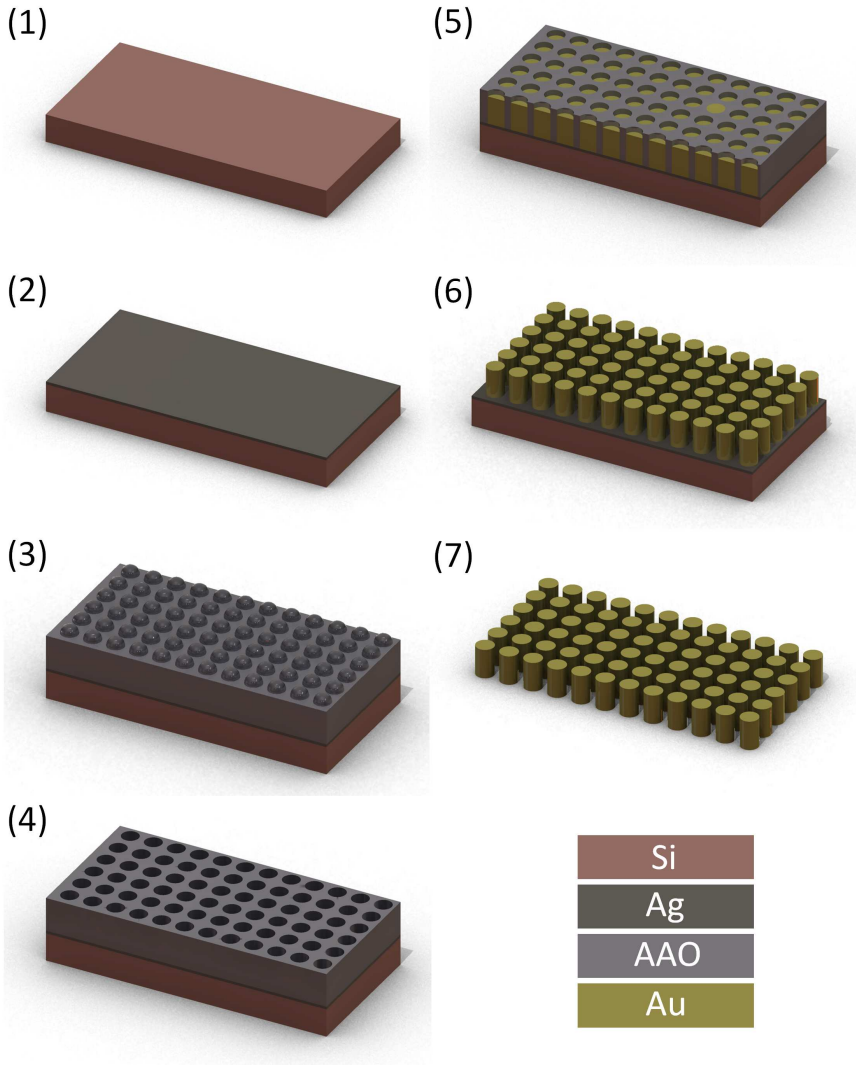

Figure 4.17: Fabrication steps of gold nanoantennas by electrochemically filling of AAO membrane. (1) Properly cleaned Si wafer. (2) Silver coated sample. (3) Branched AAO membrane on sample. (4) Cleaned AAO membrane on wafer after ICP etching. (5) Electrochemically gold deposited into AAO membrane pores. (6) Gold antennas on wafer after AAO membrane etched by H_3PO_4. (7) Gold rods in liquid after silver contact etched by HNO_3.

Chapter 5

Conclusion and Future Work

Electromagnetic wave localization properties of metal nanoantennas and high optical nonlinear coefficient of chalcogenide glasses are combined for low threshold continuum and third harmonic generation. Dipole plasmon resonance of gold nanoantennas on chalcogenide glasses are examined. Effects of wavelength of incident light, linear refractive index of substrate and medium, shape and size of antenna on resonance behaviour and strength of structure are investigated and optimized by FDTD simulations. We demonstrated that metallic antenna reduces threshold intensity value for initiating continuum generation. FDTD simulation results indicate that 500 nm FWHM spectral broadening is achievable for the peak intensity of 4.8 $W/\mu m^2$ with proposed plasmonic antenna and chalcogenide glass structure. Silica glass requires 3300 times higher power than arsenic selenide material for continuum generation on their characteristic resonant antenna lengths. Also, we showed that very small volumes of nonlinear material is enough to observe nonlinear effects, which eliminate the necessity for centimeter long material as a propagation length as in waveguide geometry. Since required antenna length for broadband light generation is much smaller than incident wavelength and resonant system is combined with nonlinear medium it is proper to use it in numerous nano scale on-chip applications.

Moreover, we fabricated the proposed gold-As_2Se_3 structure in both stripe and rod shaped antenna cases, by e-beam lithography and seed-mediated wet

chemical techniques. We proposed and applied solutions to challenges in fabrication of the system and optimized process steps of both techniques to produce nanoantennas at designed sizes. Furthermore, we optimized most of the process steps of nanoantenna fabrication by using AAO membranes to produce single and dipole antenna structures.

As a future work, we will construct an optical setup which contains femtosecond laser at around 1550 nm wavelength and fabricated nanoantenna-nonlinear material systems to observe supercontinuum generation on the structures. Also, one can produce dipole antennas with chalcogenide glass at their feed gap by optimizing remaining fabrication steps of nanorod growth by AAO membranes. Lastly, it is possible to design and fabricate new nanoantenna chalcogenide glass systems in new geometries and with new material combinations to use them for nonlinear optical applications.

Bibliography

[1] S. A. Maier, *Plamonics Fundamentals and Applications*. New York: Springer, 2007.

[2] P. Mühlschlegel, H. J. Eisler, O. J. F. Martin, B. Hecht, and D. W. Pohl, "Resonant optical antennas," *Science*, vol. 308, pp. 1607–1609, 2005.

[3] P. Biagioni, J. S. Huang, L. Duo, M. Finazzi, and B. Hecht, "Cross resonant optical antenna," *Phys. Rev. Lett.*, vol. 102, pp. 256801–1–256801–4, 2009.

[4] P. Ghenuche, S. Cherukulappurath, T. H. Taminiau, N. F. van Hulst, and R. Quidant, "Spectroscopic mode mapping of resonant plasmon nanoantennas," *Phys. Rev. Lett.*, vol. 101, pp. 116805–1–116805–4, 2008.

[5] R. Adato, A. A. Yanik, J. J. Amsden, D. L. Kaplan, F. G. Omenetto, M. K. Hong, S. Erramilli, and H. Altug, "Ultra-sensitive vibrational spectroscopy of protein monolayers with plasmonic nanoantenna arrays," *PNAS*, vol. 106, pp. 19227–19232, 2009.

[6] W. Zhang, L. Huang, c. Santschi, and O. J. F. Martin, "Trapping and sensing 10nm metal nanoparticles using plasmonic dipole antennas," *Nano Lett.*, vol. 10, pp. 1006–1011, 2010.

[7] G. von Maltzahn, J. H. Park, A. Agrawal, N. K. Bandaru, S. K. Das, M. J. Sailor, and S. N. Bhatia, "Computationally guided photothermal tumor therapy using long circulating gold nanorod antennas," *Cancer Research*, vol. 69, pp. 1–9, 2009.

[8] L. Tang, S. E. Kocabas, S. Latif, A. K. Okyay, D. S. L. Gagnon, K. C. Saraswat, and D. A. B. Miller, "Nanometre-scale germanium photodetector enhanced by near infrared dipole antenna," *Nature Photon.*, vol. 2, pp. 226–229, 2008.

[9] E. Cubukcu, E. A. Kort, K. B. Crozier, and F. Capasso, "Plasmonic laser antenna," *Appl. Phys. Lett.*, vol. 89, pp. 093120–1–093120–3, 2006.

[10] S. Kim, J. Jin, Y. J. Kim, I. Y. Park, Y. Kim, and S. W. Kim, "High-harmonic generation by resonant plasmon field enhancement," *Nature*, vol. 435, pp. 757–760, 2008.

[11] T. Schumacher, K. Kratzer, D. Molnar, M. Hentschel, H. Giessen, and M. Lippitz, "Nanoantenna-enhanced ultrafast nonlinear spectroscopy of a single gold nanoparticles," *Nature Comm.*, vol. 2, pp. 1–5, 2011.

[12] G. Brambilla, F. Koizumi, V. Finnazi, and D. J. Richardson, "Supercontinuum generation in tapered bismuth silicate fibres," *Electron. Lett.*, vol. 41, pp. 20051711–1–20051711–2, 2005.

[13] E. C. Magi, L. B. Fu, H. C. Nguyen, M. R. E. Lamont, D. I. Yeom, and B. J. Eggleton, "Enhanced kerr nonlinearity in sub-wavelength diameter as2se3 chalcogenide fiber tapers," *Opt. Exp.*, vol. 15, pp. 10324–10329, 2007.

[14] D. I. Yoem, E. C. Magi, M. R. E. Lamont, M. A. F. Roelens, L. Fu, and B. J. Eggleton, "Low-threshold supercontinuum generation in highly nonlinear chalcogenide nanowires," *Opt. Lett.*, vol. 33, pp. 660–662, 2008.

[15] P. Y. Chen and A. Alu, "Optical nanoantenna arrays loaded with nonlinear materials," *Phys. Rev. B*, vol. 82, pp. 235405–1–235405–6, 2010.

[16] B. J. Eggleton, B. L. Davies, and K. Richardson, "Chalcogenide photonics," *Nature Photon.*, vol. 5, pp. 141–148, 2011.

[17] M. L. Brongersma, "Plasmonics: Engineering optical nanoanatennas," *Nature Photon.*, vol. 2, pp. 270–272, 2008.

[18] K. L. Kelly, E. Coronado, L. L. Zhao, and G. C. Schatz, "The optical properties of metal nanoparticles: The influence of size, shape and dielectric environment," *J. Phys. Chem. B*, vol. 25, pp. 668–677, 2003.

[19] X. H. Huang, I. H. El-Sayed, W. Qian, and M. A. El-Sayed, "Cancer cells assemble and align gold nanorods conjugated to antibodies to produce highly enhanced, sharp, and polarized surface raman spectra: A potential cancer diagnostic marker," *Nano Lett.*, vol. 7, pp. 1591–1597, 2007.

[20] K. D. Osberg, M. Rycenga, N. Harris, A. L. Schmucker, M. R. Langille, G. C. Schatz, and C. A. Mirkin, "Dispersible gold nanorod dimers with sub-5 nm gaps as local amplifiers for surface-enhanced raman scattering," *Nano Lett.*, vol. 12, pp. 3828–3832, 2012.

[21] P.Anger, P. Bharadwaj, and L. Novotny, "Enhancement and quenching of single-molecule fluorescence," *Phys. Rev. Lett.*, vol. 96, pp. 113002–1–113002–4, 2006.

[22] S. Kuhn, U. Hakanson, L. Rogobete, and V. Sandoghdar, "Enhancement of single-molecule fluorescence using a gold nanoparticle as an optical nanoantenna," *Phys. Rev. Lett.*, vol. 96, pp. 017402–1–017402–4, 2006.

[23] M. Danckwerts and L. Novotny, "Optical frequency mixing at coupled gold nanoparticles," *Phys. Rev. Lett.*, vol. 98, pp. 026104–1–026104–4, 2007.

[24] J. N. Farahani, D. W. Pohl, H. J. Eisler, , and B. Hecht, "Single quantum dot coupled to a scanning optical antenna: A tunable superemitter," *Phys. Rev. Lett.*, vol. 95, pp. 017402–1–017402–4, 2005.

[25] J. N. Farahani, H. J. Eisler, D. W. Pohl, M. Pavius, P. Fluckiger, P. Gasser, and B. Hecht, "Bow-tie optical antenna probes for single-emitter scanning near-field optical microscopy," *Nanotechnology*, vol. 18, pp. 125506–1–125506–4, 2007.

[26] P. J. Schuck, D. P. Fromm, A. Sundaramurthy, G. S. Kino, and W. E. Moerner, "Improving the mismatch between light and nanoscale objects with gold bowtie nanoantennas," *Phys. Rev. Lett.*, vol. 94, pp. 017402–1–017402–4, 2005.

[27] K. D. Ko, A. Kumar, K. H. Fung, R. Ambekar, G. L. Liu, N. X. Fang, and K. C. Toussaint, "Nonlinear optical response from arrays of au bowtie nanoantennas," *Nano Lett.*, vol. 11, pp. 61–65, 2011.

[28] N. Liu, M. L. Tang, M. Hentschel, H. Giessen, and A. P. Alivisatos, "Nanoantenna-enhanced gas sensing in a single tailored nanofocus," *Nature Mater.*, vol. 10, pp. 631–636, 2011.

[29] P. A. Gonzalez, P. Albella, M. Schnell, J. Chen, F. Huth, A. G. Etxarri, F. Casanova, F. Golmar, L. Arzubiaga, L. E. Hueso, J. Aizpurua, and R. Hillenbrand, "Resolving the electromagnetic mechanism of surface-enhanced light scattering at single hot spot," *Nature Comm.*, vol. 3, pp. 1–7, 2012.

[30] A. M. Kern and O. J. F. Martin, "Surface integral formulation for 3d simulations of plasmonic and high permittivity nanostructures," *JOSA A*, vol. 26, pp. 732–740, 2009.

[31] M. Hentschel, T. Utikal, H. Giessen, and M. Lippitz, "Quantitative modeling of the third harmonic emission spectrum of plasmonic nanoantennas," *Nano Lett.*, vol. 12, pp. 3778–3782, 2012.

[32] D. M. O'Carrol, J. S. Fakonas, D. M. Callahan, M. Schierhorn, and H. A. Atwater, "Metal-polymer-metal split-dipole nanoantennas," *Adv. Mater.*, vol. 24, pp. 136–142, 2012.

[33] C. Simovski, D. Morits, P. Voroshilov, M. Guzhva, P. Belov, and Y. Kivshar, "Enhanced efficiency of light-trapping nanoantenna arrays for thin-film solar cells," *Opt. Exp.*, vol. 21, pp. 714–725, 2013.

[34] A. Zakery and S. R. Elliott, *Optical Nonlinearities in Chalcogenide Glasses and Their Applications*. Berlin: Springer, 2007.

[35] S. R. Ovshinsky, "Reversible electrical switching phenomena in disordered structures," *Phys. Rev. Lett.*, vol. 21, no. 7, pp. 1037–1050, 1968.

[36] G. Pfeiffer, M. A. Paesler, and S. C. Agarwal, "Reversible photodarkening of amorphous arsenic chalcogens," *J. Non-Cryst. Sol.*, vol. 130, pp. 111–143, 1991.

[37] M. Mitkova, M. N. Kozicki, H. C. Kim, and T. L. Alford, "Thermal and photodiffision of ag in s-rich ge-s amorphous films," *Thin Solid Films*, vol. 449, pp. 248–253, 2004.

[38] A. V. Kolobov and J. Tominaga, "Chalcogenide glassses in a solid induced by polarized light," *J. Optoelectron. Adv. Mat.*, vol. 4, pp. 679–686, 2002.

[39] S. Shabahang, M. P. Marquez, G. Tao, M. U. Piracha, D. Nguyen, P. J. Delfyett, and A. F. Abouraddy, "Octave-spanning infrared supercontinuum generation in robust chalcogenide nanotapers using picosecond pulses," *Opt. Lett.*, vol. 37, pp. 4639–4641, 2012.

[40] B. E. A. Saleh and M. C. Teich, *Fundamentals of Photonics*. New Jersey: Wiley, 2007.

[41] K. S. Yee, "Numerical solution of initial boundary value problems involving maxwells equations in isotropic media.," *IEEE Trans. Antennas Propag.*, vol. 14, pp. 302–307, 1966.

[42] D. Poljack, *Time Domain Techniques in Computational Electromagnetics*. Boston: WIT Press, 2003.

[43] G. Lenz, J. Zimmermann, T. Katsufuji, M. E. Lines, H. Y. Hwang, S. Spalter, R. E. Slusher, S. W. Cheong, J. S. Sanghera, and I. D. Aggarwal, "Large kerr effect in bulk se-based chalcogenide glasses," *Opt. Lett.*, vol. 25, pp. 254–256, 2000.

[44] J. B. Harbold, F. . Ilday, F. W. Wise, J. S. Sanghera, V. Q. Nguyen, L. B. Shaw, and I. D. Aggarwal, "Highly nonlinear as-s-se glasses for all-optical switching," *Opt. Lett.*, vol. 27, pp. 119–121, 2002.

[45] K. Ogusu, J. Yamasaki, S. Maeda, M. Kitao, and M. Minakata, "Linear and nonlinear optical properties of ag-as-se chalcogenide glasses for all-optical switching," *Opt. Lett.*, vol. 29, pp. 265–267, 2004.

[46] M. F. Bertino, R. R. Gadipalli, L. A. Martin, B. Heckman, N. Leventis, S. Guha, J. Katsoudas, R. Divan, and D. C. Mancini, "X-ray lithography of

metal and semiconductor nanoparticles," *ACS Preprints*, vol. 49, pp. 574–575, 2008.

[47] P. G. Kik, A. L. Martin, A. S. Maier, and H. A. Atwater, "Metal nanoparticle arrays for near-field opticall lithography," *ETATS-UNIS*, vol. 4810, pp. 7–13, 2002.

[48] E. U. Kim, K. J. Baeg, Y. Y. Noh, D. Y. Kim, T. Lee, I. Park, and G. Y. Jung, "Templated assembly of metal nanoparticles in nanoimprinted patterns for metal nanowire fabrication," *Nanotechnology*, vol. 20, pp. 355302–1–355302–6, 2009.

[49] G. Frens, "Controlled nucleation for the regulation of the particle size in monodisperse gold suspensions," *Nature Phys. Sci.*, vol. 241, pp. 20–22, 1973.

[50] G. S. Metraux, Y. C. Cao, R. Jin, and C. A. Mirkin, "Triangular nanoframes made of gold and silver," *Nano Lett.*, vol. 3, pp. 519–522, 2003.

[51] J. P. Juste, L. M. L. Marzan, S. Carnie, D. Y. C. Chan, and P. Mulvaney, "Electric-field-directed growth of gold nanorods in aqueous surfactant solutions," *Adv. Funct. Mater.*, vol. 14, pp. 571–579, 2004.

[52] C. J. Murphy, A. M. Gole, S. E. Hunyadi, and C. J. Orendorff, "One-dimensional colloidal gold and silver nanosructures," *Inorg. Chem.*, vol. 45, pp. 7544–7554, 2006.

[53] L. Vigderman and E. R. Zubarev, "High-yield sytnhesis of gold nanorods with longitudinal spr peak greater than 1200 nm using hydroquinone as a reducing agent," *Chem. Mater.*, vol. 25, pp. 1450–1457, 2013.

[54] H. Masuda and K. Fukuda, "Ordered metal nanohole arrays made by a two-step replication of honeycomb structures of anodic alumina," *Science*, vol. 268, pp. 1466–1468, 1995.

[55] M. R. Kim, D. K. Lee, and D. J. Jang, "Template -based electrochemically controlled growth of segmented multimetal nanorods," *J. Nanomater.*, vol. 2010, pp. 203756–1–203756–7, 2010.